UNIVERSIDAD
NACIONAL
DE COLOMBIA

Magmatism as a Tracer of the Cenozoic Crustal Evolution of the Northern Andes

Juan Sebastián Jaramillo Ríos

Universidad Nacional de Colombia

Facultad de Minas, Departamento de Materiales y Minerales

Medellín, Colombia

2024

Magmatismo como un Trazador de la Evolución Cortical Cenozoica de los Andes del Norte

Juan Sebastián Jaramillo Ríos

Tesis presentada como requisito parcial para optar al título de:

Doctor en Ingeniería

Línea de Investigación:

Geología

Director:

PhD., Agustín Cardona Molina

Codirector:

PhD., Sebastián Zapata Henao

Grupo de Investigación:

EGEO

Universidad Nacional de Colombia

Facultad de Minas, Departamento de Materiales y Minerales

Medellín, Colombia

2024

This thesis is partially based on the following publications.

Jaramillo, J. S., Zapata, S., Carvalho, M., Cardona, A., Jaramillo, C., Crowley, J. L., Bayona, G., and Caballero-Rodriguez, D., 2022. Diverse magmatic evolutionary trends of the Northern Andes unraveled by Paleocene to early Eocene detrital zircon geochemistry. Geochemistry, Geophysics, Geosystems, 23(9), e2021GC010113. https://doi.org/10.1029/2021GC010113

Jaramillo-Ríos, J. S., Cardona, A., Zapata, S., Valencia, V., Monsalve, G., & Vervoort, J. (2024). A mantle origin for Pliocene SiO2-rich ignimbrites in the modern Colombian magmatic arc. Lithos, 480–481(107666). https://doi.org/10.1016/j.lithos.2024.107666

Jaramillo-Ríos, J.S., Cardona, A., Zapata, S., Valencia, V., Monsalve, G., Schaen, A. Mafic volcanic rocks trace Pleistocene lithospheric dripping under the Colombian Andes. Submitted to Terra Nova's special issue of Crustal/lithospheric delamination (Crustal/lithospheric delamination).

Acknowledgments

To my mom and grandparents.

It was a large road with a roller coaster of feelings. First, I want to thank Agustín Cardona, who has guided me for twelve years. Agustín has always fueled my geology curiosity and has helped me face difficult moments. Victor Valencia, who trusted in my capabilities and who is an essential part of this research. Jorge Gómez, my friend who helped me during my stay in Zirchron Lab, is especially grateful. I want to thank Manuela Botero for her help at Washington State University and the EGEO research group members for all of the discussions during these years. Thanks, especially, to my co-director, Sebastian Zapata, who had to learn about geochemistry and magmatism to help me in this process. I am grateful to Carlos Jaramillo, Monica Carvalho, and the Smithsonian Tropical Research Institute for their economic assistance for a year. I want to thank my family (my grandparents, wherever they are. Ely, Gabriel, Fredy, Lina, my sisters, and my cousin Jhonatan), especially my aunt Nana, who has made me lunch for several years. To Aleja, my partner and support, my handbrake and light in the darkness. To Santi, thanks for always being there. I am wholeheartedly grateful to my cycling friends, “Los Angelitos” who were part of this roller coaster. To John Ortíz and Hernando Mahecha because they showed me geology when I was a child; now I can call them “colleagues.” To the Alcolirykoz, Los PetitFellas, Los Suziox, Wilmer Mesa, and Mario Mendoza.

Victor Valencia, John Jairo Sanchez, Camilo Bustamante, and Hugo Murcia are thanked for their strict evaluation of this dissertation and valuable comments on improving it.

Abstract

Crustal evolution in orogenic belts, such as the Northern Andes, has broadly been associated with subduction and mantle dynamics, the collision of allochthonous blocks, and the recycling of the lower crust into the asthenospheric mantle. All of these scenarios can produce magmatic rocks, which are sensitive enough to trace changes experienced by the continental crust.

In this study, field relations, petrography, zircon U-Pb (LA-ICP-MS and CA-ID-TIMS) geochronology, geochemistry, and isotopes (Hf), as well as whole-rock geochemistry and isotopes (Nd-Sr-Pb) modeling, and $^{40}Ar/^{39}Ar$ geochronological data, were used to understand the magmatic evolution of the Paleocene-Eocene continental magmatic arc and the Pliocene-Pleistocene volcanic rocks recorded in the central segment of the modern Colombian magmatic arc. Therefore, these magmatic rocks were used as a tracer of the long-term modification of the continental crust in convergent margins.

The Paleocene-Eocene (66 - 50 Ma) continental magmatic arc was formed after the collision of the Caribbean Plate with the Northern Andean continental margin at ~72 Ma. These rocks were highly exhumed and underwent high weathering and erosion rates, which resulted in the volcanic sources of this magmatism being transported to the sedimentary basins. In order to avoid sampling bias produced by the limited exposure of the plutonic facies of this magmatism, detrital zircons collected in sedimentary rocks were very important to understand the behavior of this magmatic arc.

Siliciclastic rocks from the Bogotá Formation were analyzed by LA-ICP-MS and CA-ID-TIMS geochronology and zircon chemistry. The results show that this magmatism started at ~ 66 Ma, which is ~ 4 Myr earlier than previously proposed by other authors and ended at ~50 Ma. This magmatism was formed in a heterogeneously thick continental crust, strongly controlled by strike-slip tectonics. Finally, this study proposes lithospheric dripping into the mantle to explain the bi-modal continental crust thick between 62 and 55 Ma.

After forming this arc, the continental margin was characterized by an oblique regime, which shut down the magmatic production between 50 and 35 Ma. The magmatic rocks restarted in the Western Cordillera as the Timbiquí arc and migrated toward the east up to where the modern magmatic arc is located.

During the Pliocene-Pleistocene, the central segment of the modern Colombian magmatic arc is characterized by the production of contrasting magmatic rocks, including high-silica rhyolites, adakite-like andesites, and OIB-like alkaline basalts. The high-silica rhyolitic ignimbrites were formed during a high magmatic flux (magmatic flare-up) in this arc segment at 2.6 Ma. This study proposes that the high magma flux produces a significant volume of basaltic cumulates, which were ponded in the base of the crust, facilitating the formation of garnet-bearing pyroxenites known as arclogites. This magmatic flare-up could be related to an increased sediment input into the subducted slab, as suggested by the isotopic modeling.

It is known that the arclogites in this arc segment are denser than the underlying mantle. It is proposed that Pleistocene olivine basalts and andesites associated with monogenetic volcanism found in this arc section are related to dripping rather than complete delamination of the lower crust into the asthenospheric mantle, originating from two distinct arclogites: one garnet-bearing and the other amphibole-garnet-bearing pyroxenite.

The chapters developed in this thesis demonstrate how the continental margin of the Northernmost Andes has been dynamic throughout the Cenozoic era. Unlike the Central Andes, where orogeny is predominantly driven by subduction-dynamics shortening, the Colombian orogen is influenced by block collisions, strike-slip tectonics, and magmatic underplating. The magmatic underplating in this Andean section may have been the critical factor controlling the crustal thickness and subsequent removal of the lower, denser, and unstable portion of the lithosphere.

Keywords: Magmatism, U-Pb and Ar-Ar Geochronology, Geochemistry, Isotopes, Dripping, Northern Andes

Resumen

La evolución de cinturones orogénicos como los Andes del Norte ha sido ampliamente asociado con la dinámica de la subducción y el mano, la colisión de bloques alóctonos y el reciclamiento de la corteza inferior dentro del manto astenosférico. Todos estos escenarios producen rocas magmáticas, las cuales son lo suficientemente sensibles para trazar los cambios experimentados por la corteza continental.

En este estudio, relaciones de campo, petrografía, geocronología (LA-ICP-MS y CA-ID-TIMS), química e isotopía (Hf) en circón, así como modelamiento geoquímico e isotópico (Nd-Sr-Pb) en roca total, y geocronología Ar-Ar en masa fundamental, se usaron para entender la evolución magmática del arco Paleoceno-Eoceno y rocas volcánicas del Plioceno-Pleistoceno del orógeno Nor-Andino. Estas rocas, por lo tanto, fueron usadas como trazadoras de las modificaciones de la corteza continental en márgenes continentales.

Posterior a la colusión de la Placa Caribe con la margen Nor-Andina a ~72 Ma, se formó un arco postcolisional del Paleoceno-Eoceno (66 – 50 Ma). Estas rocas junto con su basamento fueron rápidamente exhumadas y registran altas tasas de meteorización y erosión.

Con el fin de evitar el sesgo de muestreo producido por la exposición limitada de las fases magmáticas proximales, circones detríticos fueron colectados en las rocas siliciclásticas de la Formación Bogotá. Estos circones fueron químicamente analizados y datados mediante geocronología LA-ICP-MS y CA-ID-TIMS. Los resultados muestras que este arco magmático comenzó a ~ 66 Ma, lo cual es ~ 4 Ma más temprano de lo que previamente se había propuesto por otros autores y termina a ~50 Ma. Este magmatismo se formó en una margen de espesor heterogéneo, fuertemente controlada por la tectónica de rumbo. Finalmente, este estudio propone que la litosfera fue removida “dripping” para explicar la bi-modalidad del espesor cortical entre 62 y 55 Ma.

El segmento central del arco magmático reciente en Colombia durante el Plioceno-Pleistoceno fue caracterizado por la producción de rocas magmáticas contrastantes, incluidas riolitas altas en sílice, andesitas con señal tipo adaquita y basaltos alcalinos con firma tipo OIB. Las ignimbritas riolíticas ricas en sílice fueron formadas en un periodo de gran flujo magmático (flare-up) que ocurrió en este segmento del arco a 2.6 Ma. En este estudio se propone que este alto flujo magmático produjo un alto volumen de cumulatos

basálticos fueron retenidos en la base de la corteza, facilitando la formación de piroxenitas granatíferas conocidas como arclogitas. Este alto flujo magmático, podría estar relacionado al aumento del ingreso de sedimentos dentro de la placa subducente, como se evidencia en el modelamiento isotópico.

Por estudios anteriores se conoce que las arclogitas de este segmento del arco son más densas que el manto subyacente. En este estudio se propone que el vulcanismo monogenético con basaltos alcalinos del Pleistoceno en esta sección del arco, fueron formados por pequeños fragmentos delaminados “dripping” en vez de delaminación completa de la corteza inferior entre el manto astenosférico. Dos tipos de arclogitas se fundieron para generar este tipo de magmatismo, una piroxenita con granate y una piroxenita con granate y anfíbol.

Los capítulos desarrollados en esta tesis muestran cómo la margen continental de la parte más norte de los Andes ha sido dinámica a través del Cenozoico. El orógeno colombiano, a diferencia de los Andes Centrales, donde el acortamiento tectónico controla el orógeno, está controlado principalmente por la acreción de bloques, tectónica de rumbo y el apilamiento magmático. El apilamiento magmático en esta sección del arco Andino fue quizás el factor más crítico en el control del espesor cortical y posterior remoción de su parte inferior más densa e inestable.

Palabras Clave: Magmatismo, Geocronología U-Pb y Ar-Ar, Geoquímica, Isotopos, Dripping, Andes del Norte.

Content

List of figures

Pág.

List of tables

Pág.

CHAPTER 1

1. Introduction

1.1 Magmatism as a tracer of continental crust dynamics

The continental crust in active margins is dynamic through time and strongly controlled by subduction and mantle dynamics, the collision of allochthonous blocks, shortening, and magmatic underplating (Cawood et al., 2009; Condie, 2007; DeCelles et al., 2009; Karlstrom et al., 2014). Magmatic rocks are commonly formed in active continental margins due to normal subduction (Syracuse & Abers, 2006), with some exceptions, such as the cases of flat slab subduction (Ramos and Folguera, 2009). These rocks are a first-order tracer for continental crust evolution as both lower and upper plate characteristics can influence magma genesis (Carrapa et al., 2022; DeCelles et al., 2009; Lee et al., 2009; Ramos, 2009).

The thickening of the continental crust is primarily driven by coupling and flat slab subduction, which increases the shortening, as widely discussed in the case of the Central Andes (Anderson et al., 2017; Giambiagi et al., 2022; Jordan et al., 1997; Ramos, 2009; Sundell et al., 2022). The underplating of mafic and intermediate magmatic rocks at the base of the crust (Cawood et al., 2013; Jagoutz & Schmidt, 2013; Karlstrom et al., 2014; Paterson et al., 2011) and the collision of allochthonous blocks (Cawood et al., 2009), also contribute to the thickening of the upper plate.

The thinning of the continental crust has usually been related to rift settings, which could be driven by mantle plumes (Koppers et al., 2021), subduction dynamic as in the case of rollback (Best et al., 2016; Ferrari et al., 2001), or mantle dynamics that considers that the mantle heterogeneity and the changes in the convection cells could generate topography changes (Faccenna et al., 2014, Faccenna & Becker, 2020). Complete lower crust delamination is a catastrophic tectonic scenario that produces extension and thinning of the continental crust (Beall et al., 2017; Morency and Doin, 2004). In contrast, small extensional settings are related to the sinking of small pieces of the lower continental crust via

lithospheric dripping (Currie et al., 2015; Ducea et al., 2013; 2021, a,b; Murray et al., 2015; Stern et al., 2013).

The lithospheric dripping may occur either by the continuous continental shortening like the Central Andes case (Anderson et al., 2017; Beall et al., 2017; Kay and Kay, 1993; Sundell et al., 2022;) or due to magmatic underplating, which produces the thickening of the crust, metamorphic changes of the arc root and the unstability of the lower crust (Bowman et al., 2021; Ducea et al., 2021b; Houseman et al., 1981; Jagoutz and Behn, 2013).

The strike-slip is a particular tectonic scenario where the continental crust can have significant lateral changes in its thickness (Lemiszki & Brown, 1988; Schulte-Pelkum & Ben-Zion, 2012), and magmatism could occur. The Northern Andes is a place where the strike-slip has been fundamental in the geological evolution, at least since the Cretaceous (Bayona et al., 2012; Montes et al., 2019; Pindell & Kennan, 2009). This tectonic scenario has produced different basin and topography formations in the northernmost Andes (e.j. Montes et al., 2010).

Due to the high sensitivity of the magmatic rocks to these tectonic changes, whole-rock techniques such as geochemistry, isotopy analysis, and geochronology (DePaolo & Wasserburg, 1976; Ducea et al., 2015a; Gómez-Tuena et al., 2014; Klein et al., 2023; Lustrino, 2005; Lee et al., 2006; Sundell et al., 2021) or the petrochronology of detrital zircons sourced from magmatic rocks (Barth et al., 2003; Paterson et al., 2011) are employed to illuminate about the processes that occur in the crust and mantle, and allow to reconstruct the character of subduction-related settings (Alonso-Perez et al., 2009; Barth et al., 2013; DePaolo et al., 2019; Ducea et al., 2015a; Kay et al., 2014; Lee et al., 2009; Luffi & Ducea, 2022; Thorkelson et al., 2011).

1.2 Cenozoic magmatic setting of the Northern Andes

The Northern Andes is a classic example of an orogen controlled by terrane accretion (Montes et al., 2019; Pindell & Kennan, 2009; Restrepo & Toussaint, 1988), where the shortening produced by the subducted-slab dynamics, as in the Central Andes (Giambiagi et al., 2022; Jordan et al., 1997) is not clearly discriminated (**Fig. 1.1A**).

The building of the Western and Central cordilleras has been controlled by the oblique collision of allochthonous Caribbean-related blocks during the Meso-Cenozoic and the

oblique subduction of the Caribbean, Farallon, and Nazca plates (Cardona et al., 2018; Montes et al., 2019; Pindell & Kennan, 2009; Villagómez & Spikings, 2013; Zapata et al., 2019). From the Paleocene-Eocene to the Upper Miocene, the strike-slip tectonics have promoted the filling of some basins in the Colombian Andes (Montes et al., 2019; Zapata et al., 2023a, b). On the other hand, the magmatic underplating has been a fundamental factor in the construction of the central segment of the modern Colombian magmatic arc (Jaramillo-Ríos et al., 2023; 2024).

The collision of the Caribbean Plateau with the Colombian continental margin produces a quick exhumation and uplift of the continental crust during the Paleocene-Eocene (George et al., 2020; León et al., 2021; Zapata et al., 2021). This increase in the uplift rates associated with major global warming (PETM) promotes the high erosion of the whole continental crust, including plutonic and volcanic rocks from the Paleocene-Eocene magmatic arc (Zapata et al., 2021). It causes the loss of a significant quantity of valuable material for understanding what happens with an orogeny after a Plateau collision.

The Paleocene-Eocene continental magmatic arc (PECMA) has a limited and segmented exposure in the continental margin (**Fig. 1.1B**). Therefore, the tectonic and magmatic evolution of this arc has been evaluated from reduced whole-geochemistry, isotopic analysis, and geochronological data for in-situ rocks (e.g., Bustamante et al., 2017; Cardona et al., 2018; Duque-Trujillo et al., 2019a; Leal-Mejía et al., 2019). The whole-rock geochemistry shows calc-alkaline and adakite-like signatures and bi-modal isotopic (Nd-Hf) characteristics (Bustamante et al., 2017; Cardona et al., 2018; Leal-Mejía et al., 2019).

The evolution of the PECMA has been related to a short-lived continental arc developed in a thick continental crust that controlled the chemical and isotopic compositions (Bayona et al., 2012; Bustamante et al., 2017; Cardona et al., 2018; León et al., 2021), after the collision of the Caribbean Plate with the continental margin (Montes et al., 2019; Zapata et al., 2019) or to the break-off of the Caribbean Plate at 58 Ma (Leal-Mejía et al., 2019).

Two Paleocene-Eocene volcanic arc segments outcrops at the Western Cordillera of Colombia (**Fig. 1.1B**). The Cenozoic magmatic rocks related to the Panama-Chocó Block (Barbosa-Espitia et al., 2019; Cardona et al., 2018; Montes et al., 2012) that have been associated with island arc magmatism collided with the continental margin at ~20 Ma (León et al., 2018; Montes et al., 2015). On the other hand, the Timbiqui Complex, located in

southwestern Colombia, has Eocene ages ranging between 55 and 35 Ma (Barbosa-Espitia et al., 2019; Cardona et al., 2018; McCourt et al., 1990). Although the Timbiqui Complex has been related to an immature continental arc, it´s considered allochthonous or parautochthonous to the Colombian Margin (Barbosa-Espitia et al., 2019; Cardona et al., 2018). As both the Panama-Chocó Block and Timbiqui Complex are not considered part of the continental Colombian arc during the Paleocene, those are out of the scope of this study.

The continental magmatic activity in the Central Cordillera of Colombia ceased between ~50 and 25 Ma, likely due to a combination of strong strike-slip tectonics and flat-slab subduction (Bayona et al., 2012; Bustamante et al., 2017; Cardona et al., 2018; Echeverri et al., 2015; Leal-Mejía et al., 2019). Magmatic activity in the continental margin resumed at ~ 25 Ma to the west of the recent magmatic arc (Echeverri et al., 2015; Leal-Mejía et al., 2019) and subsequently migrated eastward to its current position (Echeverri et al., 2015; Wagner et al., 2017).

The modern magmatic arc, restricted to the Central Cordillera of Colombia, north of the Colombian Massif, is divided into three segments, each separated by magmatic gaps (Monsalve-Bustamante, 2020). The central arc segment, in addition to the andesite and dacite flows (Correa-Tamayo et al., 2020; Monsalve-Bustamante, 2020; Monsalve & Pulgarín, 1999), is characterized by the formation of voluminous high-silica rhyolitic pyroclastic rocks, related to the Guacacallo and Popayan formations (van der Wiel, 1991; Kroonemberg et al., 1981; Torres-Hernández, 2010). These high-silica rhyolitic pyroclastic rocks have been proposed to be formed by the Paletará Caldera (Kroonemberg et al., 1981; Torres-Hernández, 2010). To the East, the Guacacallo Formation is being intruded by both alkaline monogenetic basalts-andesites and calc-alkaline andesites related to the modern arc (Kroonenberg et al., 1982; 1987; Monsalve et al., 2020; **Fig. 1.1B**). The composition of these monogenetic magmatisms varies between alkaline basalts (nephelinites, basanites) up to olivine andesites (Kroonenberg et al., 1982; 1987).

The continental crust in this segment has a thickness of ~67 km, and the dense arc root reaches ~13.5 km (Avellaneda-Jimenez & Monsalve, 2022), which is also evident in the geoid anomaly (Chase et al., 2009). Furthermore, this arc segment has the only lower crust and mantle xenoliths known as arclogites in a modern magmatic arc worldwide (Bloch et al., 2017; Ducea et al., 2021a; Gianola et al., 2023; Notini et al., 2024; Rodriguez-Vargas et al.,

2005; Weber et al., 2002; Zieman et al., 2023). Therefore, the understanding of the Upper Miocene magmatic processes could help to understand the crustal evolution and the generation of the conditions for the formation of the arclogites in an orogeny controlled by collision and magmatic underplating instead of the tectonic shortening.

1.3 Research questions and specific objectives

1. How long does it take for the magmatic arc to re-start after a plateau collision? Was the hiatus really of ~10Ma?
2. Did the strike-slip tectonics influence arc magmatism?
3. When were the ignimbrites from Guacacallo and Popayan formed, and how long did it take to form all that volume?
4. Despite some ages from the arclogites between 5.2 and 0 Ma (Bloch et al., 2017), is it possible that the voluminous magmatism that formed the ignimbrites of Guacacallo and Popayan contributed to the formation of these arclogites?
5. How can a subduction-related setting produce both calc-alkaline and alkaline magmas in the same location?

Following the inquiries mentioned before, the objectives of this thesis are as follows:

1. To advance understanding of the Paleocene-Eocene continental magmatic arc and crustal evolution within a collisional orogeny, particularly examining how magmatism responds to the strike-slip dynamics proposed to this period in the Northern Andes (Montes et al., 2019; Pindell and Kennan 2009).

2. To uncover the causes and effects in the continental crust associated with the formation of voluminous high-silica rhyolitic magmatism from Guacacallo and Popayan formations in this segment of the Northern Andes.

3. To reveal the petro-tectonic scenarios that promote the formation of the olivine basalts and andesites in a subduction-related regime.

For the development of this thesis, the sample preparation for whole-rock geochemistry and isotopes, mineral separation, and mounting for zircon analysis was performed at Zirchron

Lab in Tucson, Arizona. Zircon chemistry, U-Pb LA-ICP-MS geochronology, and Hf isotopes were performed at the Radiogenic Isotope and Geochronology Lab (RIGL), and whole-rock analysis at the Peter Hooper GeoAnalytical Lab at Washington State University. Procedure details are presented in each chapter of this thesis.

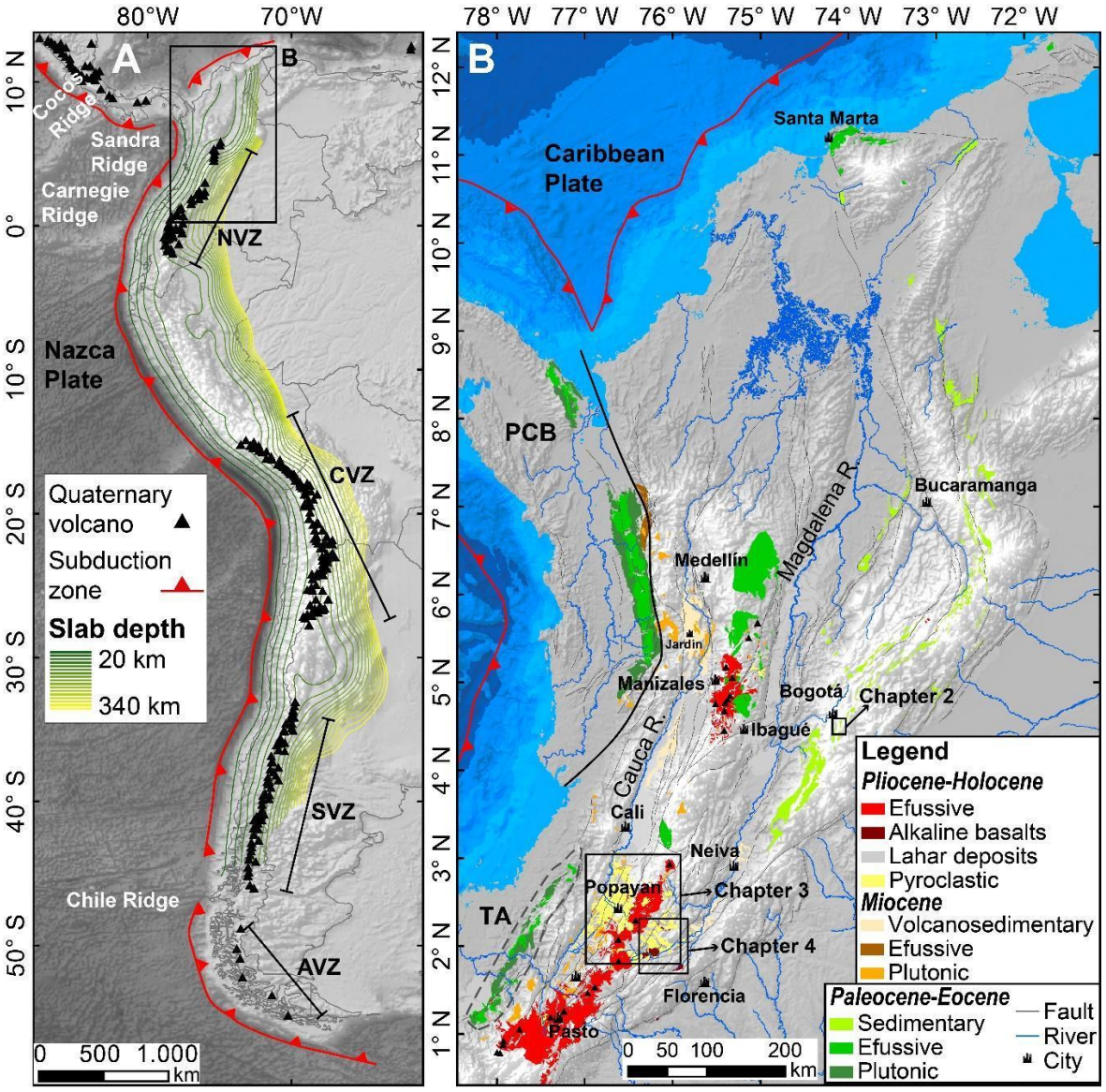

Figure 1. 1. Location of the Colombian Andes in the Andean chain. A Map showing the Andean segmentation and the respective oceanic ridges of the Nazca Plate. B) Colombian map with the outcrops of Paleocene-Eocene and the Miocene to modern magmatic and sedimentary rocks. Boxes correspond to the chapters presented in this study. Slab depth (Hayes et al., 2018), Quaternary volcanoes (Global Volcanism Program, 2023). Paleocene-Eocene and Pliocene Holocene magmatism and sedimentary rocks (Modified of Gómez & Montes, 2020). PCB: Panama-Chocó Block; TA: Timbiquí arc.

The zircon chemistry, isotope, and geochronological approach was used to understand the spatio-temporal evolution of the Paleocene-Eocene continental magmatic arc (PECMA) and Pleistocene to modern magmatic arcs in the Northern Andes. Considering that at least all the Paleocene-Eocene magmatic bodies from the Colombian Andes have limited exposures (**Fig. 1.1B**), Paleocene-Eocene sedimentary rocks from the sedimentary Bogotá Formation were analyzed by zircon U-Pb LA-ICP-MS geochronology and REE to determine the magmatic contribution. Younger grains were then analyzed for CA-ID-TIMS to obtain more precise ages of the detrital populations and, therefore, obtain a better approximation of the magmatic evolutionary trends to this post-collisional magmatism. Whole-rock geochemistry and isotopic database were grouped with zircon geochronology and REE to decipher the magmatic conditions that controlled the formation of a Pliocene flare-up in the central segment of the modern Colombian arc. Also, whole-rock geochemistry, isotopy, and Ar-Ar geochronology were used to understand the magmatic processes necessary to generate the alkaline basalts that intrude on the Pliocene volcanic rocks.

Chapter 2 addressed the influence of strike-slip tectonics in a collisional orogen. This chapter demonstrates how a detrital perspective aids in resolving such issues when in-situ proximal rocks are limited or absent. The maturation of the Paleocene-Eocene post-collisional magmatic arc was constrained using zircon chemistry and LA-ICP-MS and CA-ID-TIMS geochronology. The magmatic evolution of this arc, influenced by strike-slip tectonics, exhibits a bi-modal crustal thickness and ages ranging between 62 and 55 Ma. These characteristics were interpreted as a consequence of the foundering of the lower crust into the asthenospheric mantle.

Chapter 3 addresses the geochronological, geochemical, and isotopic data from Pliocene voluminous high-silica rhyolitic magmatism outcropping in the central segment of the modern Colombian magmatic arc. The results presented in this thesis delineate and group two distinct cartographic units known as the Popayan and Gucacallo formations. These pyroclastic rocks, covering an area of approximately ~3000 km^2 and with a moderately estimated dense rock equivalent (DRE) volume of 155 km^3, were formed within a restricted period (<0.1 Ma). The pyroclastic rocks contain at least twice as much material as the modern arc, which began forming approximately 1.5 Ma ago. This thesis concludes that the magmatic

flare-up episode that produced these voluminous pyroclastic rocks created optimal conditions for forming arclogites.

Chapter 4 demonstrates the coexistence of olivine basalts and andesites, some of those alkaline, with calc-alkaline rocks in subduction-related magmatism. This peculiar and volumetrically limited type of magmatism, formed under high temperatures and pressures, could be associated with the melting of garnet-bearing pyroxenites. Therefore, these olivine basalts and andesites could represent magmatism resulting from small-scale lithospheric dripping in the central segment of the Colombian arc.

Finally, Chapter 5 provides a broader discussion and concluding remarks addressing the elements found in each chapter of this thesis, showing how magmatism is sensitive and contributes to the evolution of the continental crust during the Cenozoic in the Colombian Andes.

These contributions, which formed the Ph.D. thesis, demonstrate how Cenozoic magmatism in the Northern Andes has been sensitive to changes in the tectonic regime and how magmatism has shaped the continental crust over time. These results provide insight into the significance of the detrital record of sedimentary basins, particularly in cases where magmatic rocks are poorly exposed. Furthermore, they allow us to understand the construction of the central segment of the modern Colombian magmatic arc and the relationships between magmatism, thickening by magmatic underplating, and subsequent dripping.

CHAPTER 2

2. Diverse magmatic evolutionary trends of the Northern Andes unraveled by Paleocene to early Eocene detrital zircon geochemistry

---

2.1 Abstract

The Paleocene-early Eocene continental magmatic arc (PECMA) in the Northern Andes is an example of arc magmatism following a major collisional event. This arc formed after the arc-continent collision between the Caribbean Plate and the South American continental margin at ca. 72 Ma. We used detrital zircon LA-ICP-MS and CA-ID-TIMS geochronology and geochemistry to complement the limited plutonic record of the PECMA and better characterize the PECMA's magmatic evolution. Zircon geochronology and their respective trace element geochemistry were analyzed from the Paleocene-early Eocene strata of the Bogotá Formation in the foreland region. Our results show that after the Caribbean Plate collision, the PECMA magmas differentiated under a thick continental crust with limited subduction input at ca. 66 Ma. By 62–50 Ma, scattered patterns of Hf, U, U/Yb, and Yb/Gd ratios in detrital zircons suggest the existence of contrasting magmatic inputs attributed to different depths of crustal fractionation, varied temperatures of crystallization, and significant mantle and subduction inputs. These diverse magmatic patterns reflect the evolution of the continental crust. We proposed that oblique convergence and strike-slip tectonics favored contrasting crustal architectures along the continental margin while local lithosphere dripping from a previously thickened crust promoted the formation of hot magmas under a thick continental crust.

Key Points

Detrital zircon geochemistry was used to better refine the post-collisional Paleocene to Eocene tectono-magmatic evolution of the Northern Andes.

The Paleocene-early Eocene detrital zircons crystallized in contrasting magmatic conditions and under varying crustal thicknesses.

Strike-slip tectonics, crustal dripping, and a previously thickened continental crust can explain the observed diverse magmatic trends.

2.2 Introduction

The spatial distribution and composition of magmatic arcs are controlled by interactions between the mantle and the upper and lower plates, led by tectonic processes that typically last over one to tens of millions of years (Ducea et al., 2015a; Gerya & Meilick, 2011; Paterson & Ducea, 2015; Syracuse & Abers, 2006). The plutonic and volcanic products that result from these interactions reflect different stages of the magmatic evolution: whereas plutonic rocks represent a more homogenized final record of a magmatic event, volcanic rocks are a snapshot of the magmatic settings at the time of the eruption (e.g., Glazner et al., 2015; Zimmerer & McIntosh, 2012).

Andean-type orogens are characterized by coeval magmatism, exhumation, and surface uplift (Bayona et al., 2021; Horton, 2018; Horton et al., 2010, 2015). These concurrent events often result in the erosion of the uppermost segment of the volcanic arcs (volcanic and shallow plutonic rocks) and the exposure of deeper plutons (e.g., Barth et al., 2013; Yang et al., 2012). The exhumation and erosion of the initial magmatic products often bias the record of past volcanic arcs (Gaschnig et al., 2017).

Despite this bias, some of the volcanic arc's older record can be preserved in adjacent basins, and their study can provide additional insights into the magmatic system (Barth et al., 2013; Malusà et al., 2011; McKenzie et al., 2018; Schwartz et al., 2021; Yang et al., 2012). Magmatic zircons provide the isotopic and chemical composition of the system at the time of their crystallization (Cavosie et al., 2005; Grimes et al., 2015; Vervoort et al., 2004). Because these minerals are resistant to low-grade metamorphism, weathering, and sedimentary processes, they can retain their geochemical signatures after transport and burial (Morton & Hallsworth, 2007; Rubatto, 2017). The record of detrital zircons found in sedimentary basins adjacent to magmatic arcs can, therefore, provide evidence of their

isotopic and chemical signatures (Barth et al., 2013; Cavosie et al., 2005, 2006; McKenzie et al., 2018; Yang et al., 2012).

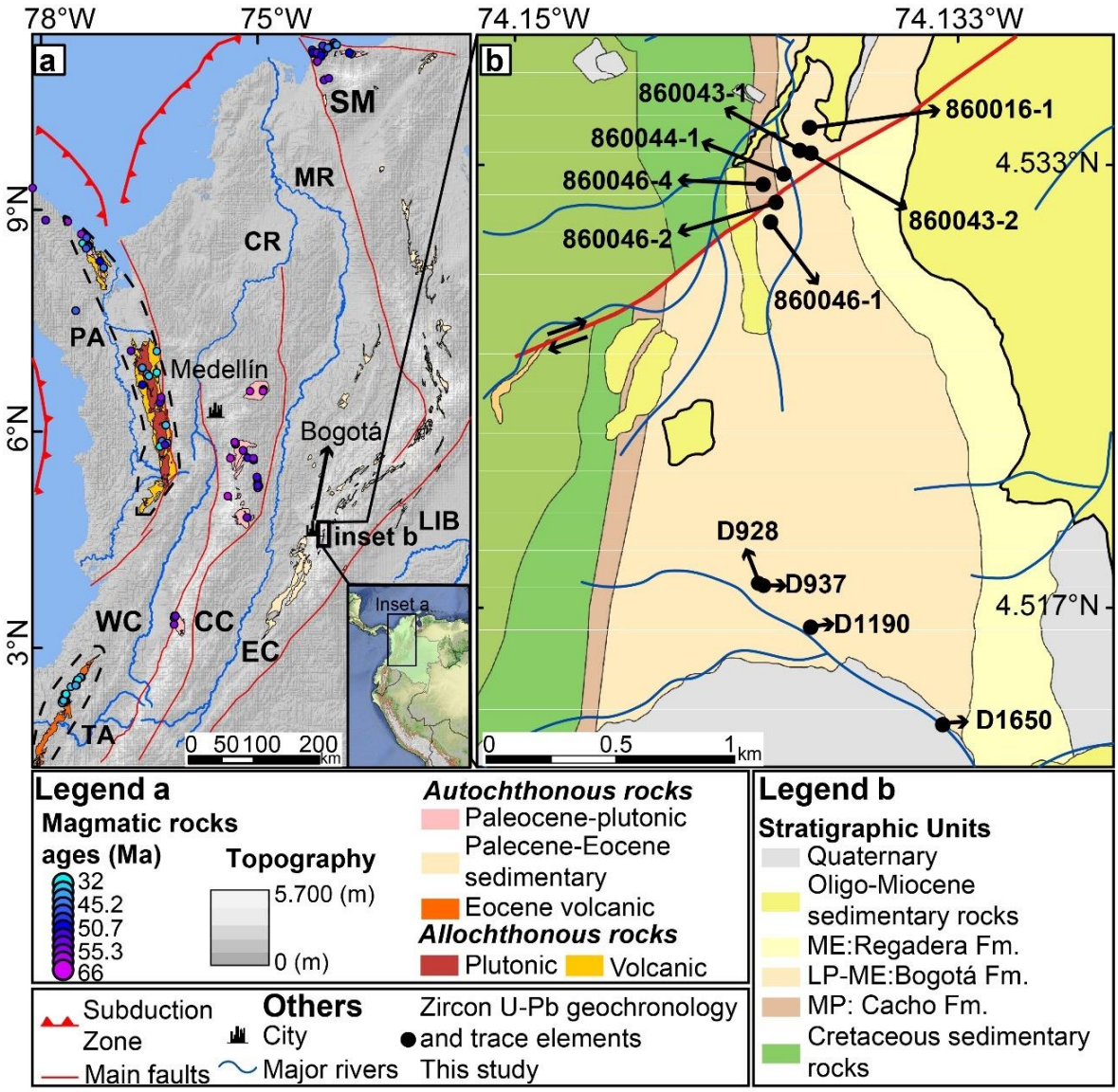

Figure 2. 1. Location maps. **A)** Regional map showing the Paleocene-Eocene volcanic, plutonic, and sedimentary rocks and radiometric ages from the Colombian Andes. **B)** Geological map of the study region modified from Acosta and Ulloa (1998), WC: Western Cordillera, CC: Central Cordillera, EC: Eastern Cordillera, SM: Santa Marta Massif, LlB: Llanos Basin, PA: Allochthonous Panama Arc, CR: Cauca River, MR: Magdalena River, TA: Timbiquí Arc.

In the Northern Andes, the Late Cretaceous collision between the Caribbean and the South American Plates led to intense deformation, crustal thickening, and topographic growth along the continental margin (Bayona et al., 2012; Jaramillo et al., 2017; Kennan & Pindell, 2009; León et al., 2021; Pindell & Kennan, 2009; Villagómez & Spikings, 2013;

Zapata et al., 2021). During the Paleocene and early Eocene, subduction of the Caribbean Plate formed a post-collisional magmatic arc along the South American continental margin (Paleocene–early Eocene continental magmatic arc, PECMA). The plutonic remnants of this arc are partially preserved and exposed in the Central Cordillera and Caribbean regions of Colombia, but the volcanic components are either not exposed or preserved (**Fig. 2.1A**) (Bayona et al., 2010, 2012; Bustamante et al., 2017; Cardona et al., 2011, 2018; Duque-Trujillo et al., 2019a; Leal-Mejía et al., 2019; Ordoñez et al., 2001). Based on this limited record, the subduction of the Caribbean Plate beneath a thick continental crust (Bayona et al., 2012; Bustamante et al., 2017) and slab break-off at ca. 58 Ma (Leal-Mejía, 2011; Leal-Mejía et al., 2019) have been proposed as the tectonic scenarios that controlled the post-collisional magmatic evolution. However, the absence of a more complete magmatic record hinders the understanding of the evolution of the NW South American margin.

The PECMA was built on top of the basement (Permian-Triassic metamorphic rocks and Cretaceous igneous and sedimentary rocks) of the Central Cordillera and the Santa Marta Massif, which have had a positive high-relief since the Late Cretaceous. These high-relief regions acted as a sediment source for adjacent basins, including the foreland basins to the East (Bayona et al., 2012, 2021; Horton et al., 2015; Zapata et al., 2021). The middle Paleocene-early Eocene Bogotá Formation is a ca. 1.4 km-thick clastic sequence located in the axial zone of the Eastern Cordillera, around 150 km east of the Central Cordillera (**Fig. 2.1A**). Triassic, Jurassic, Cretaceous, and Paleocene-early Eocene populations of detrital zircons suggest that the basement of the Central Cordillera (basement of the PECMA) and the PECMA were the dominant source areas for the sediments of the Bogotá Formation (Bayona et al., 2010, 2012, 2021). Given that maximum depositional ages (MDA) of sandstones of the Bogotá Formation and Paleocene–early Eocene populations of detrital zircons become progressively younger towards the top of the sequence, it is likely that vulcanism of the PECMA was nearly coeval with sedimentation in this basin (Alberts et al., 2021; González et al., 2018; Rodríguez-Alonso et al., 2004). LA-ICP-MS and CA-ID-TIMS detrital zircon geochronological and geochemical constraints from the Bogotá Formation were used to improve our understanding of the PECMA. The integration of this detrital record with data from exposed plutonic rocks (Bustamante et al., 2017; Cardona et al., 2011, 2018;

Duque-Trujillo et al., 2019a; Leal-Mejía et al., 2019) provides further insight into the dynamics of convergent margin tectonic settings, especially after the transition from collision to subduction (Brown & Ryan, 2011; Draut & Clift, 2001).

2.2.1 Cretaceous to Eocene tectonic evolution of the Northern Colombian Andes (6-12°N)

The basement of the Western Cordillera of Colombia is a remnant of the allochthonous Caribbean Plate–a thick oceanic plateau and intraoceanic arc accreted to the continental margin during the Late Cretaceous (ca. 72 Ma) (George et al., 2021; Jaramillo et al., 2017; Kennan & Pindell, 2009; Kerr et al., 1997; Pardo-Trujillo et al., 2020; Pindell & Kennan, 2009; Restrepo & Toussaint, 1988; Villagómez & Spikings, 2013). Various sources of evidence–thermo-kinematic models, stratigraphy, and crustal thickness estimates based on whole-rock geochemistry–suggest that the collision of this plate caused the deformation, uplift, and exhumation of the pre-Cretaceous basement that is currently exposed in the Central Cordillera (Bustamante et al., 2017; León et al., 2021; Zapata-Villada et al., 2021; Zapata et al., 2021).

The onset of subduction after the collision was responsible for the development of PECMA. U-Pb zircon ages from exposed plutons show that magmatism started at ca. 62 Ma and ceased at ca. 50 Ma (Bayona et al., 2012; Bustamante et al., 2016). The age of this plutonic record has been interpreted as evidence of a hiatus between the collision (ca. 72 Ma) and the onset of subduction (Bayona et al., 2012; Bustamante et al., 2017; Cardona et al., 2018; Duque-Trujillo et al., 2019b; Leal-Mejía et al., 2019). Magmatism has also been interpreted as a product of asthenospheric upwelling driven by a post-collisional slab break-off (Leal-Mejía, 2011; Leal-Mejía et al., 2019), yet this interpretation assumes that the collision of the Caribbean Plate and the NW South American continental margin occurred during the Eocene. An Eocene collision does not agree with time constraints based on the intrusion of undeformed plutonic rocks that show evidence of an earlier Late Cretaceous collision (Bustamante et al., 2017; Duque-Trujillo et al., 2019b; Jaramillo et al., 2017; Villagómez & Spiking, 2013; Zapata-Villada et al., 2021). During the Oligocene, the northern segment of the PECMA was fragmented and became displaced, resulting in the

formation of the Santa Marta Massif and Guajira ranges (Kennan & Pindell, 2009; Montes et al., 2010, 2019; Parra et al., 2020; Pindell & Kennan, 2009; Weber et al., 2010).

This Late Cretaceous-Paleocene collisional orogenic phase resulted in the development of high topography that became the source area of adjacent syn-orogenic basins to the east (Bayona et al., 2021; León et al., 2021; Pardo-Trujillo et al., 2020; Zapata et al., 2021). The syn-orogenic middle Paleocene-early Eocene continental succession of the Bogotá Formation (61-50 Ma) corresponds to a fluvial system that accumulated under high subsidence rates in a basin adjacent to the PECMA (**Fig. 2.1A**) (Bayona et al., 2012, 2021). Fluvial sediments were mainly sourced from the paleo-Central Cordillera and the PECMA in addition to several intrabasinal uplifts (Montes et al., 2012) and smaller volcanic sources within the basin (Bayona et al., 2012, 2021; Caballero et al., 2020).

In addition to the PECMA, two other Paleocene-Eocene magmatic arcs are currently exposed in the Northern Andes (**Fig. 2.1A**). These comprise (i) the Timbiqui continental volcanic arc (~55-35 Ma) that intruded the oceanic basement of the Western Cordillera south of 3°N (Barbosa-Espitia et al., 2019; Cardona et al., 2018) and (ii) the allochthonous oceanic Panama-Chocó arc exposed along the western flank of the Western Cordillera and the Pacific coast north of 4°N (Barbosa-Espitia et al., 2019; León et al., 2018; Montes et al., 2015; Villagómez et al., 2011; Zapata-García & Rodríguez-García, 2020). These arcs are, however, unlikely sources of sediments for the Bogotá Formation given that the Timbiqui arc is significantly younger, and the Panama arc formed in a distal position, SW of the continental margin, and collided with the continental margin in the Middle Miocene (León et al., 2018; Montes et al., 2015).

2.2.2 Previous Paleocene-Eocene whole-rock and zircon geochemical and isotopic data

The magmatic record of the PECMA in the Colombian Andes is restricted to plutonic rocks exposed in the Central Cordillera and Santa Marta Massif. These rocks have been interpreted as part of an active magmatic arc characterized by U-Pb zircon ages between 62 and 50 Ma with calc-alkaline and adakite-like geochemical signatures (Bustamante et al., 2017; Cardona et al., 2011, 2018; Leal-Mejía et al., 2019). Currently, evidence of PECMA

magmatism earlier than 60 Ma is restricted to small plutons in the Santa Marta Region (Cardona et al., 2011; Duque-Trujillo et al., 2019a) and antecrysts in younger, Late Paleocene plutons (Bustamante et al., 2017). These antecrysts have $\varepsilon Hf_{(i)}$ values between +1.5 and +5.9 (**Fig. 2.2A**), which are characteristic of zircons formed in magmas that derived from the mantle (Iizuka et al., 2017) and were modified by assimilation of an older continental crust (Bustamante et al., 2017; Cardona et al., 2018).

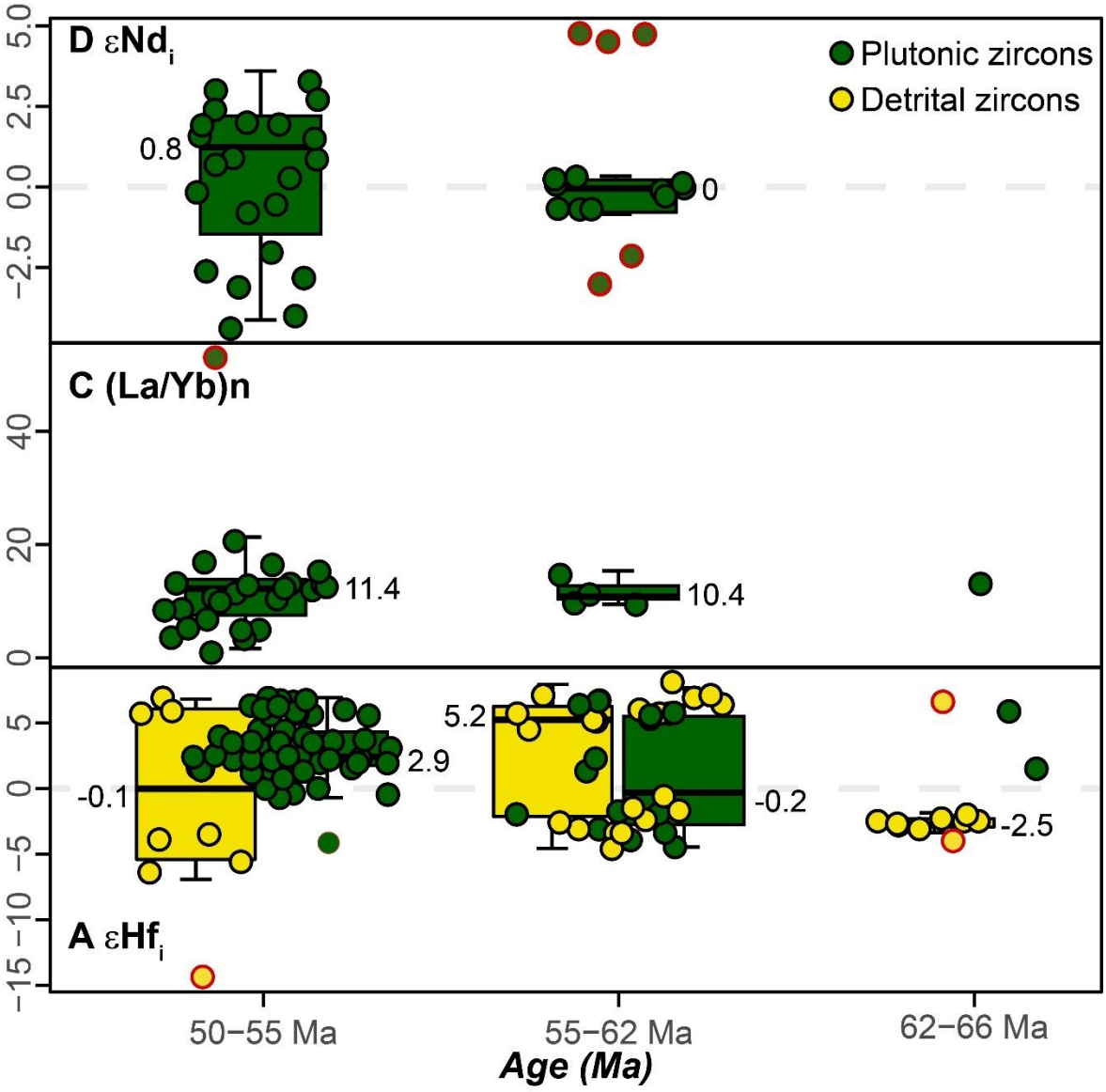

Figure 2. 2. Boxplot from whole-rock compiled analyses from PECMA plutonic rocks (Bustamante et al., 2017; Cardona et al., 2018, 2011; Leal-Mejía et al., 2019; Ordoñez et al., 2001; Rueda-Gutiérrez, 2019). **A)** Age vs. Zircon εHf values from plutonic (green circles) and detrital zircons (yellow circles). **B)** Age vs. La/Yb normalized to chondrite composition (McDonough and Sun, 1995). **C)** Age vs. εNd from whole-rock plutons, the boxplots show the error bars and thick lines correspond to the mean values after removing outliers (red borders).

Plutons between 62 and 50 Ma show whole rock (La/Yb)n ratios between 3.3 and 19.7 (**Fig. 2.2B**) that suggest crustal thickness values between 39 and 59 km (Bustamante et al., 2017; León et al., 2021). These also show whole-rock $\varepsilon Nd_{(i)}$ values between -3 and +4 while $\varepsilon Hf_{(i)}$ values range between -4.2 and +6.9 (**Fig. 2.2A, C**) that indicate both mantle and crustal inputs (Bustamante et al., 2017; Cardona et al., 2011, 2018; Leal-Mejía et al., 2019; Ordoñez et al., 2001).

Zircons with ages between 66 and 62 Ma have $\varepsilon Hf_{(i)}$ values between -4.0 and -2.0 in addition to a single grain with an $\varepsilon Hf_{(i)}$ of +6.6; those with ages between 62 and 50 Ma have a higher variation in $\varepsilon Hf_{(i)}$ values and range between -14.4 and +8.1 (**Fig. 2.2A**) (Bustamante et al., 2017). These isotopic data also suggest different amounts of mantle and crustal contributions throughout the magmatic evolution of the PECMA.

2.3 Methods

2.3.1 Field observations and sampling strategy

Eight samples of fluvial sandstones and a reworked volcanic tuff were collected from two stratigraphic sections of the Bogotá Formation. These are separated less than 3 km apart and crop out in the Parque Industrial Mochuelo, Bogotá, Colombia (**Fig. 2.1B**). The sections comprise thick, mottled mudstone beds with paleosol development (argillisols, oxisols) (Morón et al., 2013), interbedded fine-grained to conglomeratic fluvial sandstones, volcaniclastic sandstones, and a reworked volcanic tuff. **Fig. 2.3** shows the relative stratigraphic position of the analyzed samples. All samples were collected as part of previous stratigraphic and paleontological studies carried out in an area with abundant leaf beds and vertebrates that record the Paleocene-early Eocene global warming events (e.g., Bayona et al., 2012; Jaramillo and Cardenas, 2013; Moron et al., 2013). In this location, the Bogotá Formation is interpreted as a middle Paleocene-early Eocene meandering to a braided fluvial depositional system sourced from the west (Bayona et al., 2010, 2021). This unit is conformably overlying the middle Paleocene sandstones of the Cacho Formation, and it is unconformably overlain by middle to upper Eocene fluvial conglomeratic sandstones of the Regadera Formation (Bayona et al., 2010). Both the Cacho and Regadera formations lack evidence of syn-sedimentary magmatism.

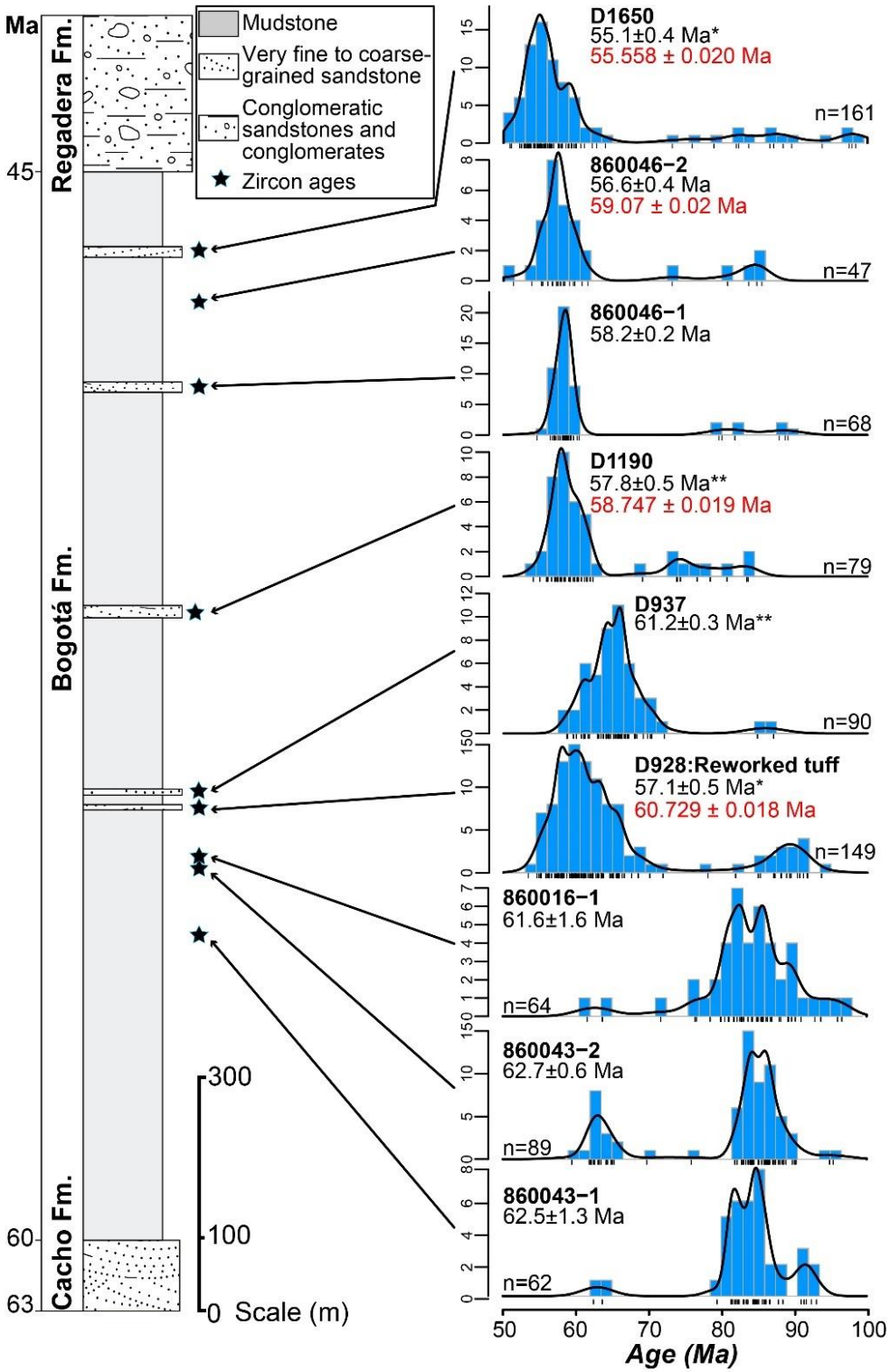

Figure 2. 3. Generalized stratigraphic section from the Bogotá Formation (modified from Bayona et al., 2012). Blue stars denote the samples with zircon geochronological and geochemical data, and the rectangles are samples without zircon REE data compiled from Bayona et al. (2012). Each sample's KDE distributions show only the Paleocene-Eocene geochronological data. The red number corresponds to the younger CA-ID-TIMS age.

2.3.2 Zircon U-Pb geochronology

Zircon U-Pb geochronology and geochemistry have been widely used to reconstruct the evolution of magmatic rocks (Schaltegger et al., 2015). Given that sedimentary transport and diagenesis do not significantly modify zircon geochemical composition, detrital grains can be used to constrain the ages and the composition of the magmatic sources (Gehrels, 2014; Horton et al., 2015).

Zircons separated from nine samples from the Bogotá Formation were analyzed with LA-ICP-MS to obtain U-Pb dates and trace element concentrations. Only sharply faceted euhedral crystals were analyzed with the aim of increasing the chances of collecting data from the young volcanic grains and avoiding older crystals that could have undergone multiple sedimentation cycles (Cretaceous to Precambrian). This procedure may have created a bias in the zircon populations; however, this contribution focuses on the magmatic evolution of the Paleocene-Eocene magmatic arc and does not intend to answer a question of provenance. Various provenance analyses have already been previously carried out in the Bogotá Formation (Bayona et al., 2010, 2012, 2021).

The zircons that yielded the youngest LA-ICP-MS dates were further dated using CA-ID-TIMS. Twenty-nine zircon grains from three clastic samples (860046-2, D1190, and D1650) and one from a reworked tuff sample (D928) were analyzed using CA-ID-TIMS (Table 2.1).

2.3.2.1 LA-ICP-MS Geochronology

Zircon grains were separated from rocks using standard techniques, annealed at 900°C for 60 hours in a muffle furnace, and mounted in epoxy and polished until their centers were exposed. Cathodoluminescence (CL) images were obtained with a JEOL JSM-300 scanning electron microscope and Gatan MiniCL. Zircon was analyzed by laser ablation inductively coupled plasma mass spectrometry (LA-ICP-MS) using a ThermoElectron X-Series II quadrupole ICPMS and New Wave Research UP-213 Nd:YAG UV (213 nm) laser ablation system. In-house analytical protocols, standard materials, and data reduction software were used for the acquisition and calibration of U-Pb dates and a suite of high-field strength elements (HFSE) and rare earth elements (REE). Zircon was ablated with a laser spot of 25

μm wide using fluence and pulse rates of 5 J/cm^2 and 5 Hz, respectively, during a 45-second analysis (15 s gas blank, 30 s ablation) that excavated a pit ~15 μm deep. Ablated material was carried by a 1.2 L/min He gas stream to the nebulizer flow of the plasma. Dwell times were 5 ms for Si and Zr, 200 ms for ^{49}Ti and ^{207}Pb, 80 ms for ^{206}Pb, 40 ms for ^{202}Hg, ^{204}Pb, ^{208}Pb, ^{232}Th, and ^{238}U and 10 ms for all other HFSE and REE. Background count rates for each analyte were obtained prior to each spot analysis and subtracted from the raw count rate for each analyte. Ablations pits that appear to have intersected glass or mineral inclusions were identified based on Ti, and P. U-Pb dates from these analyses are considered valid if the U-Pb ratios appear to have been unaffected by the inclusions. Analyses that appear contaminated by common Pb were rejected based on mass 204 being above baseline. For concentration calculations, background-subtracted count rates for each analyte were internally normalized to ^{29}Si and calibrated with respect to NIST SRM-610 and -612 glasses as the primary standards. Temperature was calculated from the Ti-in-zircon thermometer (Ferry and Watson, 2007). Because there are no constraints on the activity of TiO_2, an average value in crustal rocks of 0.6 was used.

For U-Pb and ^{207}Pb/^{206}Pb dates, instrumental fractionation of the background-subtracted ratios was corrected, and dates were calibrated with respect to interspersed measurements of zircon standards and reference materials. The primary standard Plešovice zircon (Sláma et al., 2008) was used to monitor time-dependent instrumental fractionation based on two analyses for every 10 analyses of unknown zircon. A secondary correction to the ^{206}Pb/^{238}U dates was made based on results from the zircon standards Seiland (531 Ma, unpublished data, Boise State University) and AUSZ2 (38.9 Ma, Kennedy et al., 2014), which were treated as unknowns and measured once for every 10 analyses of unknown zircon. These results showed a linear age bias of several percent that is related to the ^{206}Pb count rate. The secondary correction is thought to mitigate matrix-dependent variations due to contrasting compositions and ablation characteristics between the Plešovice zircon and other standards (and unknowns).

Radiogenic isotope ratio and age error propagation for all analyses include uncertainty contributions from counting statistics and background subtraction. The standard calibration uncertainty for U/Pb is the local standard deviation of the polynomial fit to the fractionation factor of Plešovice versus time, and for ^{207}Pb/^{206}Pb is the standard error of the mean of the

fractionation factor of Plešovice. Errors without and with the standard calibration uncertainty are shown in the data table. These uncertainties are 0.4-2.7% (2σ) for $^{206}Pb/^{238}U$ and 0.3-1.0% (2σ) for $^{207}Pb/^{206}Pb$. Errors on single analyses without the standard calibration uncertainty are given below. Age interpretations are based on $^{207}Pb/^{206}Pb$ dates for analyses with $^{207}Pb/^{206}Pb$ and $^{206}Pb/^{238}U$ dates >1000 Ma. Otherwise, interpretations are based on $^{206}Pb/^{238}U$ dates. Errors are at 2σ. The Kernel density estimates (KDEs), concordance plots, and maximum depositional ages were estimated using the radial plot method (Vermeesch, 2021). Each sample was plotted using Isoplot R (Vermeesch, 2018).

2.3.2.2 CA-ID-TIMS Geochronology

Zircon was removed from the epoxy mounts for dating based on CL images and LA-ICP-MS data, except for sample D1190, which did not get analyzed by LA-ICP-MS; CL images were used for grain selection.

Zircon was put into 3 ml Teflon PFA beakers and loaded into 300 µl Teflon PFA microcapsules. Fifteen microcapsules were placed in a large-capacity Parr vessel, and the zircon was partially dissolved in 120 µl of 29 M HF for 12 hours at 190°C. Zircon was returned to 3 ml Teflon PFA beakers, HF was removed, and zircon was immersed in 3.5 M HNO_3, ultrasonically cleaned for an hour, and fluxed on a hotplate at 80°C for an hour. The HNO_3 was removed, and zircon was rinsed twice in ultrapure H_2O before being reloaded into the 300 µl Teflon PFA microcapsules (rinsed and fluxed in 6 M HCl during sonication and washing of the zircon) and spiked with the EARTHTIME mixed ^{233}U-^{235}U-^{205}Pb tracer solution (ET535) or EARTHTIME mixed ^{233}U-^{235}U-^{202}Pb-^{205}Pb tracer solution (ET2535) (Condon et al., 2015). Zircon was dissolved in Parr vessels in 120 µl of 29 M HF with a trace of 3.5 M HNO_3 at 220°C for 48 hours, dried to fluorides, and re-dissolved in 6 M HCl at 180°C overnight. U and Pb were separated from the zircon matrix using an HCl-based anion-exchange chromatographic procedure (Krogh, 1973), eluted together, and dried with 2 µl of 0.05 N H_3PO_4.

Pb and U were loaded on a single outgassed Re filament in 5 µl of a silica-gel/phosphoric acid mixture (Gerstenberger and Haase, 1997), and U and Pb isotopic measurements made on a GV Isoprobe-T multi-collector thermal ionization mass spectrometer equipped with an

ion-counting Daly detector. Pb isotopes were measured by peak-jumping all isotopes on the Daly detector for 100 to 160 cycles. Analyses spiked with ET535 tracer solution were corrected for 0.16 ± 0.03%/a.m.u. (1σ) mass fractionation and analyses spiked with ET2535 tracer solution were corrected for mass fractionation using the known $^{202}Pb/^{205}Pb$ ratio of the tracer solution. Transitory isobaric interferences due to high-molecular-weight organics, particularly on ^{204}Pb and ^{207}Pb, disappeared within approximately 60 cycles, while ionization efficiency averaged 10^4 cps/pg of each Pb isotope. Linearity (to ≥1.4 x 10^6 cps) and the associated deadtime correction of the Daly detector were monitored by repeated analyses of the NBS982 standard and have been constant since installation. Uranium was analyzed as UO_2^+ ions in static Faraday mode on 10^{12}-ohm resistors for 300 cycles and corrected for isobaric interference of $^{233}U^{18}O^{16}O$ on $^{235}U^{16}O^{16}O$ with an $^{18}O/^{16}O$ of 0.00206. Ionization efficiency averaged 20 mV/ng of each U isotope. U mass fractionation was corrected using the known $^{233}U/^{235}U$ ratio of the tracer solution.

U-Pb dates and uncertainties were calculated using the algorithms of Schmitz & Schoene (2007), calibration of ET535 tracer solution (Condon et al., 2015) of $^{235}U/^{205}Pb$ = 100.233, $^{233}U/^{235}U$ = 0.99506, and $^{205}Pb/^{204}Pb$ = 11268, calibration of ET2535 tracer solution (Condon et al., 2015) of $^{235}U/^{205}Pb$ = 100.233, $^{233}U/^{235}U$ = 0.99506, $^{205}Pb/^{204}Pb$ = 8474, and $^{202}Pb/^{205}Pb$ = 0.99924, U decay constants recommended by Jaffey et al. (1971), and $^{238}U/^{235}U$ of 137.818 (Hiess et al., 2012). $^{206}Pb/^{238}U$ ratios and dates were corrected for initial ^{230}Th disequilibrium using $D_{Th/U}$ = 0.20 ± 0.05 (1σ) and the algorithms of Crowley et al. (2007), increasing the $^{206}Pb/^{238}U$ dates of ~0.09 Ma. All common Pb in analyses were attributed to laboratory blank and subtracted based on the measured laboratory Pb isotopic composition and associated uncertainty. U blanks are estimated at 0.013 pg.

Weighted mean $^{206}Pb/^{238}U$ dates are calculated from equivalent dates (probability of fit >0.05) using Isoplot 3.0 (Ludwig, 2003). Errors on weighted mean dates are given as ± x / y / z, where x is the internal error based on analytical uncertainties only, including counting statistics, subtraction of tracer solution, and blank and initial common Pb subtraction, y includes the tracer calibration uncertainty propagated in quadrature, and z includes the ^{238}U decay constant uncertainty propagated in quadrature. Internal errors should be considered when comparing our dates with $^{206}Pb/^{238}U$ dates from other laboratories that used the same tracer solution or a tracer solution that was cross-calibrated using EARTHTIME gravimetric

standards. Errors, including the uncertainty in the tracer calibration, should be considered when comparing our dates with those derived from other geochronological methods using the U-Pb decay scheme (e.g., laser ablation ICPMS). Errors, including uncertainties in the tracer calibration and ^{238}U decay constant (Jaffey et al., 1971), should be considered when comparing our dates with those derived from other decay schemes (e.g., $^{40}Ar/^{39}Ar$, ^{187}Re-^{187}Os). Errors are at 2σ.

Sample locations are presented in Table 2.1 and **Fig. 2.1B**. Figure 4 shows the Kernel density estimates (KDEs), concordance plots, and maximum depositional ages estimated using the radial plot method (Vermeesch, 2021). Each sample was plotted using Isoplot R (Vermeesch, 2018). We discuss and interpret zircon data from 128 grains (seven samples) with dates between 66 and 50 Ma. We only considered zircon grains that had ages with 2σ errors lower than 4 Ma.

Table 2. 1. Locations and youngest LA-ICP-MS date and youngest CA-TIMS date from the nine samples analyzed. *Data from Bayona et al. (2012). All CA-TIMS ages are from this study.

Sample	Lat	Long	Youngest LA-ICP-MS date	Youngest CA-ID-TIMS age
860016-1	4.53454	-74.13919	61.6±1.7	
860043-1	4.53367	-74.13951	62.4±1.2	
860043-2	4.53357	-74.13910	59.5±2.2	
860046-1	4.53098	-74.14059	54.6±2.7	
860046-2	4.53173	-74.14040	51.4±1.9	59.07±0.02
D928	4.53700	-74.16300	50.9±3.6; 56.2±1.2*	60.68±0.04
D937	4.53700	-74.16300	59.0±4.0**	
D1190	4.53700	-74.16300	54.1±3.5**	58.72±0.04
D1650	4.53700	-74.16300	52.5±3.0*; 53.6±1.1**	55.53±0.04

2.3.3 Zircon geochemistry and estimates of crustal thickness

The relative concentration of trace elements in zircons is controlled by multiple magmatic processes. For instance, Hf, Th, and U can be directly associated with specific magma compositions and are, therefore, indicative of magma compositional differentiation and crustal assimilation (Claiborne et al., 2006; Kirkland et al., 2015). Yb and Y can be

preferentially trapped in minerals crystallized at high pressures, which allows inferring crystallization depths (Barth et al., 2013), and Ti content is dependent upon magma temperatures (Ferry & Watson, 2007).

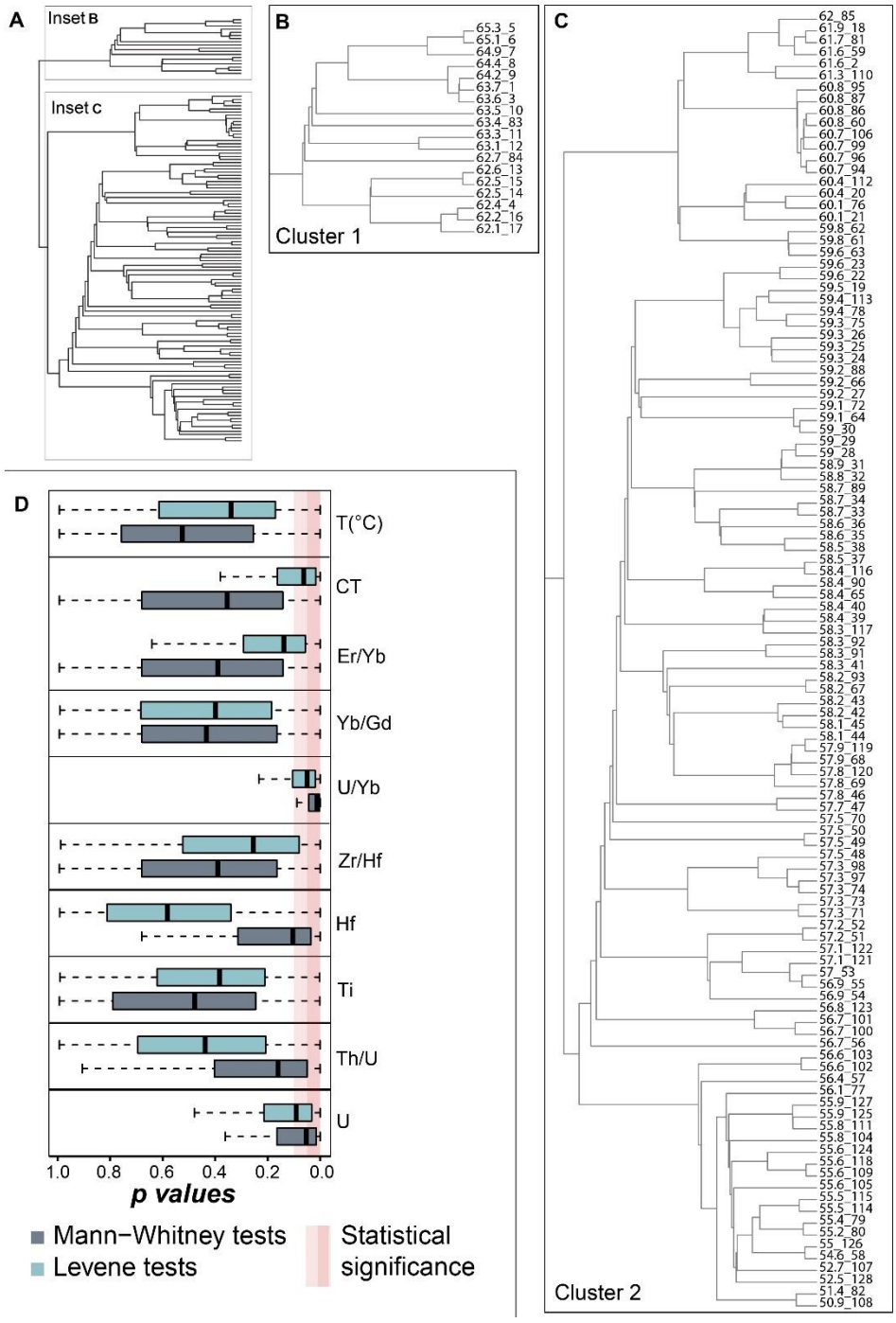

Figure 2. 4. Statistical analysis of trace element composition. **A)** Cluster analysis results using the Euclidean distance and coniss agglomeration method, the age and code of each grain are on the right axis. **B)** Resulting *p*-values distribution of the Levane and Mann-Whitney test for ten geochemical parameters; CT: Crustal thickness and T(°C): Magma temperature calculated from Ti values.

The crustal thickness was estimated following Tang et al. (2021). This approach is based on the Eu anomaly (Eu/Eu* ratio), which is sensitive to fractionation under varying pressure (Tang et al., 2021). Under high pressures, the preferential incorporation of Fe^{+2} into garnet enhances the oxidation of multivalent trace elements such as Eu (Tang et al., 2018; 2019a). The oxidation of Eu increases the availability of Eu^{+3} concerning Eu^{+2} and facilitates the incorporation of Eu in the zircon lattice. Consequently, zircons crystallized under high pressure and crustal thickness exhibit lower Eu anomalies, which is evidenced in higher Eu/Eu* ratios. Conversely, shallow magma fractionation will result in higher Eu anomalies and low Eu/Eu* ratios (Tang et al., 2021). Crustal thickness values derived from zircon geochemistry are nonetheless approximations and need to be interpreted carefully, as Eu/Eu* ratios may be affected by different magmatic processes such as assimilation of mature basements, co-crystallization of plagioclase and zircon at shallow depths, and variations in the redox state of the melts (Holder et al., 2020; Tang et al., 2021).

Cathodoluminescence and reflected images were used to avoid ablating close to zircon inclusions. Additionally, the geochemical signatures of zircons with Th/U>0.1, P>500, and Lan>30 were discarded to prevent potential contamination induced by inclusions (apatite, monazite, rutile, etc.), metamictization, and metamorphism.

2.3.4 Statistical analysis of trace element composition

A cluster analysis using Euclidean distance and coniss agglomeration method (package 'rioja,' Juggins, 2020) was performed in zircons with ages between 66 and 50 Ma to identify general patterns in zircon composition over time. This analysis used a distance matrix based on U, Hf, Ti contents, Th/U, Zr/Hf, U/Yb, Yb/Gd, and Er/Yb ratios and estimates of temperature and crustal thickness. We followed the silhouette width criterion to evaluate the optimal number of clusters (Kaoungku et al., 2018). Two clusters were identified based on age and similarities in geochemical composition (**Fig. 2.4A, B, C**), grouping zircons dated between 66.0 and 62.0 Ma and between 62.0 and 55.0 Ma. The geochemical composition of zircons dated between 66.0 and 62.0 Ma to those between 62.0 and 55.0 Ma was compared (**Fig. 2.4D**). Because the sample size was not constant across these two age intervals, each age group (n=10 zircons) was subsampled to test for differences in mean values and variance

of U, Hf, Ti contents, Th/U, Zr/Hf, U/Yb, Yb/Gd, and Er/Yb ratios, and estimates of temperature and crustal thickness. For each subsample, a Mann-Whitney U test (Mann & Whitney, 1947) was applied to assess differences in the mean, and Levene tests (Levene, 1960) were used to contrast the variance of these across age groups. The subsampling and statistical tests were iterated 1000 times, and the distribution of *p*-values resulting from the Levene or Mann-Whitney tests are presented in **Fig. 2.4D**. Differences in the chemical composition of zircons when the resulting *p*-value distribution is noticeably skewed toward zero were considered, with the first quartile (LVQ1 and MWQ1 for Levene and Mann-Whitney tests, respectively) below 0.05 and median value close to 0.1. This statistical approach allows the identification of significant differences in the geochemical composition of zircon grains before and after 62 Ma.

2.4 Results

2.4.1 LA-ICP-MS and CA-ID-TIMS Geochronology

A total of 489 zircons, which measure 60–390 μm long and have a length: width aspect ratio of 2:1–4:1 (**Fig. 2.5A**), were analyzed. Under cathodoluminescence, the predominant zircon population exhibits oscillatory zoning (**Fig. 2.5A**) characteristic of magmatic growth (Corfu et al., 2003). Some of these zircons show sector zoning, which may be related to rapid changes in the growth conditions (e.g., temperature and growth rates) during crystal formation (Paterson & Stephens, 1992). Zircons with homogeneous cores and complex rims were interpreted as older xenocrysts with younger overgrowth (Miller et al., 2003).

LA-ICP-MS dates included Triassic (~238 Ma; n=26), Jurassic (~160 Ma; n=58), Late Cretaceous (~84 Ma, n=197), and Paleocene (~59 Ma; n=156) populations (**Fig. 2.5B**), which despite the bias induced by the selection of sharply faceted grains are similar to the zircon age distributions presented in previous provenance studies (Bayona et al., 2012; Bustamante et al., 2017). The Paleocene to early Eocene zircons range between 66.0 and 50.9 Ma and have a large population with dates ca. 57.7 Ma and a secondary population with dates ca. 62.8 Ma (**Fig. 2.5B**).

Detrital zircon populations of Paleocene–Eocene age become progressively younger towards the top of the Bogotá Formation, suggesting that volcanism was contemporary with sediment deposition (**Fig. 2.3**) (Alberts et al., 2021; González et al., 2018). The basal segment of the Bogotá Formation is characterized by zircon dates between 65.3 and 59.5 Ma (18 zircons) with maximum depositional ages between 62.5 and 61.6 Ma (**Fig. 2.3**). Samples from the upper stratigraphic segment show zircon dates between 66.0 and 50.9 Ma with maximum depositional ages between 61.2 and 55.1 Ma. Zircon grains with dates between 55.0 and 50.9 Ma are restricted to a few zircons at the top of the stratigraphic section (**Fig. 2.3**), suggesting an early Eocene age for the uppermost beds of the Bogotá Formation (Bayona et al., 2012, 2021).

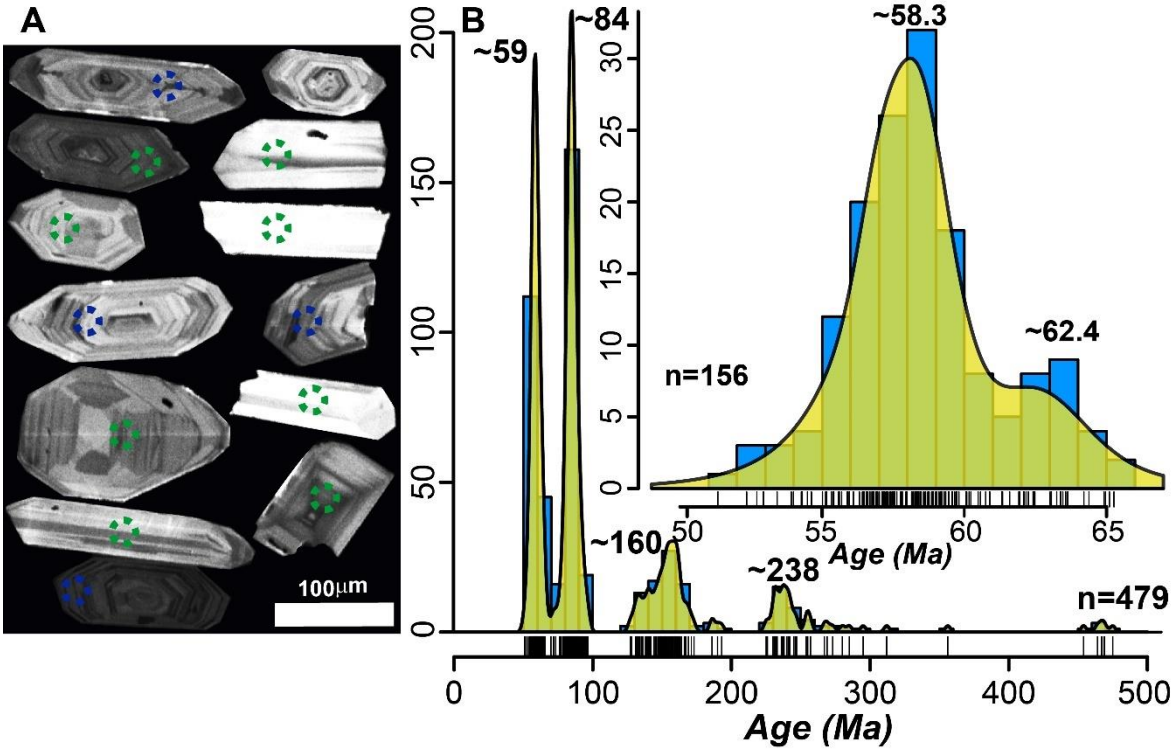

Figure 2. 5. Cathodoluminescence and KDE from Paleocene-Eocene detrital zircons. **A)** Cathodoluminescence of representative Paleocene-Eocene detrital zircons. Blue circles indicate grains with CA-TIMS ages and geochemical signatures obtained using LA-ICP-MS. Green circles indicate grains with REE and geochemical signatures obtained using LA-ICP-MS. Circles are 25 µm wide and indicate the position of the LA-ICP-MS analysis spot. **B)** Age distribution (blue) and kernel density estimation (yellow) of 479 detrital zircons. The inset contains the age distribution for 156 zircons aged 66 and 50 Ma. Black bars in the *x*-axis of KDE represent individual ages.

The dates of detrital zircons from the Bogotá Formation obtained using LA-ICP-MS are overall older than the LA-ICP-MS dates from PECMA plutonic rocks (t-value = -16.526,

degrees of freedom = 567.67, *p*-value < 2.2e-16) (Bustamante et al., 2017; Cardona et al., 2011, 2018; Leal-Mejía et al., 2019; Ordoñez et al., 2001; Rueda-Gutiérrez, 2019). Whereas detrital grains have a mean age of 59.4 Ma, plutonic zircons have a mean age of 55.7 Ma (**Fig. 2.6A**). Therefore, our data represent older stages of magmatic evolution that are not preserved in the plutonic record of the cordillera.

Detrital zircon grains (6 to 8 per sample) analyzed under CA-ID-TIMS yielded maximum depositional ages between 55.53 ± 0.04 and 60.68 ± 0.04 Ma (Table 1). Overall, dates obtained using CA-ID-TIMS are 0.4 to 3.6 Ma older than those obtained using LA-ICP-MS. These discrepancies may be related to lead loss or radiation damage, which are not detected by LA-ICP-MS (Herriott et al., 2019).

2.4.2 Trace element composition of detrital zircons from the Bogotá Formation

A cluster analysis based on the age and geochemical composition of 128 Paleocene-early Eocene detrital zircon grains is shown in **Fig. 2.4A–C**. The silhouette width criterion recognizes two distinct clusters (**Fig. 2S1**) that group zircons between 66.0 and 62.0 Ma (n = 18) and those between 62 and 50 Ma (n=110). These results suggest changes in magma composition and crystallization conditions over time (before and after 62.0 Ma). Trace elements in older zircon grains (66.0 to 62.1 Ma) are less variable than in younger grains (62 to 55 Ma) (**Fig. 2.6; 2.7**). Even though a larger number of younger zircon grains can account for a higher heterogeneity, U, Hf, U/Yb, and crustal thickness values show statistically distinctive trends before and after 62 Ma despite differences in the numbers of zircons (see section 2.3.4; **Fig. 2.4A**).

The content of U across the 128 Paleocene-early Eocene detrital zircons analyzed ranges between 60 ppm and 2200 ppm, and Th/U ratios range between 0.1 and 1.4. U content (mean values and variance) differs significantly between the younger and older detrital zircon populations (LVQ1=0.03 and MWQ1=0.01; **Fig. 2.4D**) even though no significant differences in Th/U ratios are observed (LVQ1=0.21 and MWQ1=0.05; **Fig. 2.4D**). Ti values range between 1.7 ppm and 33.2 ppm and do not show significant differences across both age groups (LVQ1=0.21 and MWQ1=0.25; **Fig. 2.4D**). These Ti values correspond to zircon saturation temperatures between 937 and 641°C. Hf content varies between 6,000 and 18,000

ppm, and Zr/Hf ratios range between 17 and 71.7. Hf content in younger zircons differs from that in older zircons (MWQ1=0.04 and LVQ1=0.34), whereas Zr/Hf ratios show no significant differences in mean values or variance (LVQ1=0.08 and MWQ1=0.17; **Fig. 2.4D**). U/Yb ratios vary between 0.1 and 5.3, showing differences in mean values and variances measured in younger and older zircons (LVQ1=0.02 and MWQ1=0.00; **Fig. 2.4D**). Zircons older than 62 Ma have low U/Yb ratios (0.2-1.0), whereas those measured in grains younger than 62 Ma are more widespread and range up to 5 (**Fig. 2.7A**). Er/Yb ratios range between 0.2 and 0.9, with the highest values observed among the younger grains (62 to 50 Ma), even though no significant differences between groups were found (MWQ1=0.14 and LVQ1=0.06; **Fig. 2.4D**). Yb/Gd ratios range between 1.3 and 60 and show no differences in younger and older zircons (MWQ1=0.17 and LVQ1=0.19**; Fig. 2.4D**). Estimates of crustal thickness based on Eu anomalies (Eu/Eu*) fall between 30.2 and 96 km. These estimates show a bimodal distribution with mean values of 41 ± 6 and 73 ± 9 km (**Fig. 2.8 A, B**). The smaller values of crustal thickness are only retrieved from younger zircons (62 to 50 Ma); therefore, the variance of estimated crustal thickness differs significantly between younger and older zircons (LVQ1=0.02). No significant difference was observed for mean values of the crustal thickness (MWQ1=0.14).

The composition of trace elements in detrital zircons dating between 95 and 73 Ma (n=196) differs from that of PECMA-derived zircons. Cretaceous zircons are characterized by lower U content (<1,000 ppm) and U/Yb ratios (<1), a narrow range of Zr/Hf ratios (15 to 30), and smaller crustal thickness values (mean of 44.6 ± 8.1 km) when compared with the Paleogene zircons.

2.5 Discussion

The deformation and exhumation phases that characterized the Late Cretaceous to Cenozoic tectonic evolution of the Northern Andes eroded the volcanic cover and shallow plutonic rocks on top of the PECMA (Bayona et al., 2010, 2012; Pardo-Trujillo et al., 2020; Villagómez & Spikings, 2013). The poor preservation of the magmatic record presents a major limitation in understanding the processes that controlled the evolution of this magmatic

arc. As a means to overcome these limitations, we analyzed detrital zircons deposited in a synorogenic basin adjacent to the PECMA and preserved in the Bogotá Formation.

We interpret the Paleocene-early Eocene detrital zircon populations recovered from sandstones of the Bogotá Formation to be part of the eroded volcanic and plutonic cover of the PECMA. Previous provenance and stratigraphic analyses of the Bogotá Formation indicate that this sequence formed in a mature fluvial system that drained the paleo-Central Cordillera (Bayona et al., 2012; 2021; Bustamante et al., 2017). This depositional system may have also had a large source area that facilitated sediment mixing (Bayona et al., 2010, 2021; Bustamante et al., 2017). Our results show that samples collected in different stratigraphic positions have progressively younger zircon populations towards the top of the Bogotá Formation, consistent with a scenario in which volcanism is coeval with sedimentation. Despite the induced bias in our analytical strategy (see section 3.2), samples from similar stratigraphic positions exhibit similar and reproducible zircon age distributions, suggesting a homogenized detrital record of the Paleocene-Eocene magmatism (e.g., samples 860046-1 and 860046-2). This detrital record is older than zircons retrieved from *in-situ* plutonic rocks (**Fig. 2.6A**) and, therefore, complements the plutonic record by providing a geochemical fingerprint of the volcanic and plutonic rocks formed during earlier magmatic phases of the PECMA.

2.5.1 Early onset of magmatism indicates a short post-collisional magmatic lull

The plutonic remnants of the PECMA include 62 to 60 Ma plutons and extensive plutonism between 55 and 50 Ma (**Fig. 2.1A**). In absence of evidence of earlier magmatism, this fragmentary plutonic record has been interpreted as the result of a magmatic hiatus between 72 and 62 Ma caused by the collision of the Caribbean Plateau (Bayona et al., 2012; Bustamante et al., 2017; Duque-Trujillo et al., 2019b; Jaramillo et al., 2017; Zapata-Villada et al., 2021).

The detrital zircons retrieved from the Bogotá Formation exhibit a longer and more robust record of arc magmatism that spans between 66.0 and 50.9 Ma. The age of this record suggests that following the accretion of the Caribbean Plate at ca. 72 Ma, subduction and magmatism re-started at least by 66 Ma, instead of 62 Ma, as previously interpreted (Bayona et al., 2012; Bustamante et al., 2017; Duque-Trujillo et al., 2019b; Jaramillo et al., 2017;

Zapata-Villada et al., 2021). Detrital zircons aged between 66.0 and 64.0 Ma represent ~8% of the Paleocene-Eocene detrital zircon population found in the Bogotá Formation and indicate an earlier onset of post-collisional magmatism. Zircon antecrysts of similar Late Cretaceous-Paleocene age (ca. 66 Ma) have been documented from *in-situ* plutonic rocks of the PECMA (Cardona et al., 2011; Duque-Trujillo et al., 2019b), further supporting magmatism that pre-dates 62 Ma. The finding of this study implies that the magmatic hiatus was shorter (≤ 6 Ma) than previously proposed (Duque-Trujillo et al., 2019b; Leal-Mejía et al., 2019) and that magmatism was nearly continuous in the transition from a collisional to a subduction setting.

2.5.2 Geochemistry and isotopes reflect changes in magma composition/magmatic evolutionary trends

A clustering analysis based on zircon trace element composition identifies two distinct clusters (**Fig. 2.4A**): an older cluster that groups 66.0 to 62.0 Ma zircons (**Fig. 2.4B**) and a younger cluster that includes zircons with ages between 62.0 and 50.9 Ma (**Fig. 2.4C**). These results show that zircon geochemistry changed significantly after 62.0 Ma and suggest varying conditions in the magmatic processes that controlled the zircon crystallization through time.

2.5.2.1 Early stages of post-collisional magmatic arc evolution (66.0 Ma to 62.0 Ma)

The 66.0 Ma to 62.0 Ma detrital zircon geochemistry represents the early stages of the arc that followed the Late Cretaceous collision of the Caribbean Plate with the continental margin. This record shows a scenario of limited subduction and magmas that emplaced and differentiated in a thick continental crust (>55 km) that formed during the collision. Similar scenarios have been previously suggested (George et al., 2021 and references therein; Leon et al., 2021).

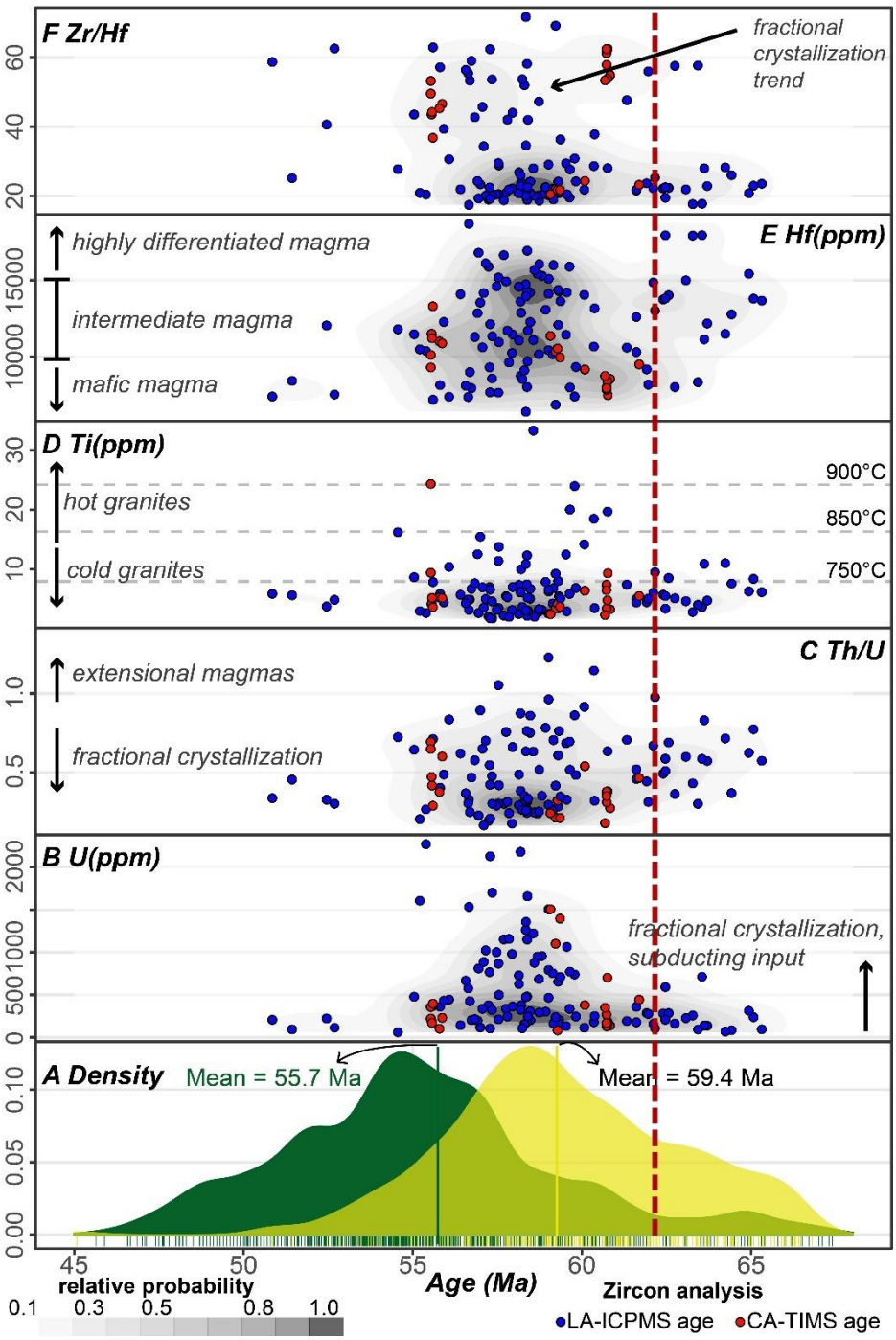

Figure 2. 6. Compared KDE and detrital zircon geochemistry concerning zircon age. **A)** Normalized probability density plot (PDP) of PECMA zircon dates from the Central Cordillera (green shadow) (Bayona et al., 2012; Bustamante et al., 2017; Cardona et al., 2018, 2011,2014; Duque-Trujillo et al., 2019a; Rueda-Gutiérrez, 2019) and detrital zircon dates from the Bogotá Formation (yellow shadow) (Bayona et al., 2012; this work). **B)** Age (Ma) vs. U (ppm). **C)** Age (Ma) vs. Th/U. **D)** Age (Ma) vs. Ti (ppm) and their inferred saturation temperatures (Ferry and Watson, 2007). **E)** Age (Ma) vs. Hf (ppm). **F)** Age (Ma) vs. Zr/Hf. The dashed red box indicates the time interval between 62 and 55 Ma. Annotations are from Belousova et al. (2002), Claiborne et al. (2006; 2010), Kirkland et al. (2015), McKay et al. (2018), Yang et al. (2012).

Whole-rock geochemistry of Cretaceous magmatic rocks (100 to 80 Ma) supports the existence of a thin to medium (20 to 55 km) crust before the collision of the Caribbean Plate with the continental margin (Bustamante et al., 2017; Jaramillo et al., 2017; León et al., 2021). Detrital zircons of Cretaceous age (101.9 to 66.2 Ma) retrieved from the Bogotá Formation agree with this scenario: their low Eu anomalies (Eu/Eu*) are consistent with a medium crust and provide thickness estimates of 44 ± 8 km (**Fig. 2. S2.** See Methods).

Paleocene detrital zircons from the same sedimentary unit, however, present higher Eu anomalies that reflect a thick crust by the early Paleocene and provide crustal thickness estimates between 55 and 80 km (mean value of 72 ± 7.3 km; **Figs. 2.6; 2.7; 2.8**). Independent evidence from whole-rock geochemistry of a 65.0 Ma pluton exposed in the Santa Marta Massif reported by Cardona et al. (2011) and Duque-Trujillo et al. (2019a) supports this observation. The (La/Yb)n ratio of this pluton provides estimates of a crustal thickness of ca. 50 km (Cardona et al., 2011; Duque-Trujillo et al., 2019a), and further indicates that the continental crust thickened during the Late Cretaceous. Both the detrital and plutonic records support that a thick crust (>50 km) was in place during the early stages of the PECMA.

The geochemistry of the 66.0 to 62.0 Ma detrital zircon population is suggestive of limited subduction in the early development of the PECMA. The relatively low U content and low U/Yb ratios (**Fig. 2.6**) are consistent with zircon-forming magmas derived from a depleted mantle with a limited presence of fluids. This composition is expected under limited subduction (Barth et al., 2013; Grimes et al., 2015). Even though the 66.0 Ma to 62.0 Ma detrital zircon record overall coincides with a coeval plutonic record, contrasting values of $\varepsilon Hf_{(i)}$ potentially highlight differences in magmatic sources. Whereas detrital zircons have negative $\varepsilon Hf_{(i)}$ values (-4 to -2) (**Fig. 2.7F**), zircon antecrysts with ages between 66–62 Ma found in 55-50 Ma plutonic rocks show positive $\varepsilon Hf_{(i)}$ values (1.5 to 5.9) (Bustamante et al., 2017; Cardona et al., 2011). This dissimilarity suggests that between 66 and 62 Ma, magmatic sources were a mixture of juvenile magmas and an old continental crust.

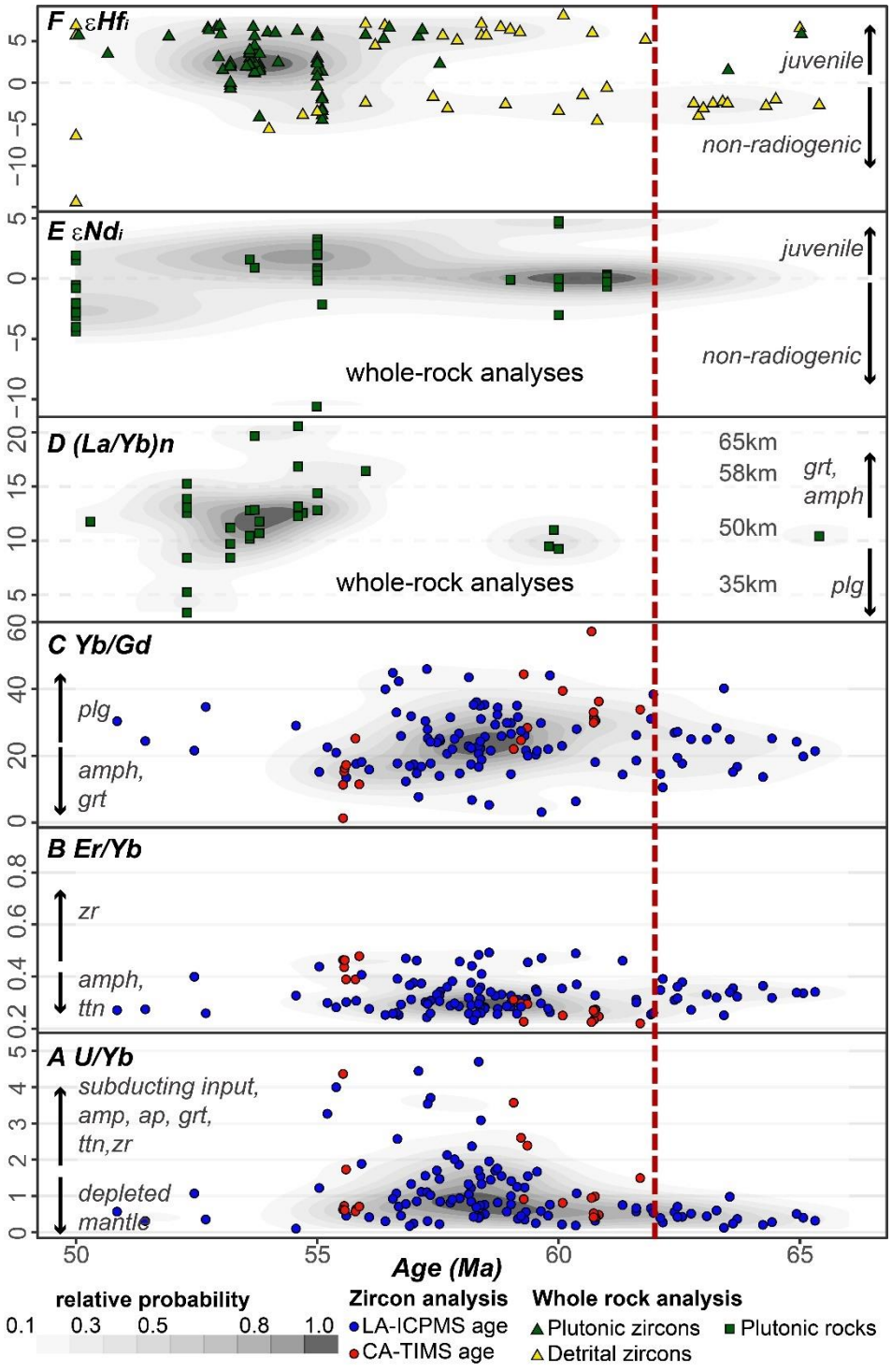

Figure 2. 7. Whole rock and detrital zircon geochemistry concerning zircon age. **A)** Age (Ma) vs. U/Yb ratios. **B**) Age (Ma) vs. Er/Yb ratios. **C)** Age (Ma) vs. Yb/Gd ratios. **D)** Age (Ma) vs. Whole-rock geochemistry (La/Yb). **E)** Age (Ma) vs. Whole-rock Nd radiogenic isotope signatures**. F)** Age (Ma) vs. Hafnium isotopic signature in zircons from the PECMA and detrital zircons from Bogotá Formation. Whole rock and isotopic signatures are from (Bustamante et al., 2017; Cardona et al., 2011; Duque-Trujillo et al., 2019a; Leal-Mejía, 2011; Villagómez et al., 2011). Annotations are from Barth et al. (2013), Grimes et al. (2015), Profeta et al. (2015), and Sundell et al. (2021).

2.5.2.2 A continental margin dominated by diverse magmatic evolutionary trends (62 to 50 Ma)

Even though dates from LA-ICP-MS may be inadequate to identify distinct trends in zircon age composition within short time intervals (<10Ma), the combination of LA-ICP-MS dates and geochemical data with more precise CA-ID-TIMS dates allowed us to identify different compositional pools in zircons with ages between 66.0 and 50.9 Ma. These Younger zircons are characterized by a wider range and differences in mean values of U, U/Yb, Ti, Hf, and crustal thickness when compared to older –66.0 to 62.0 Ma–zircons (**Figs. 2.6; 3.7; 2.8**). A wider range in these values suggests the occurrence of both low and highly differentiated and fractionated magmas (Belousova et al., 2002) after 62 Ma. Since Zr/Hf ratios and U values do not exhibit a systematic enrichment and an associated Ti reduction, these variations cannot be explained by the fractionation of a single magma (Grimes et al., 2009; Wang et al., 2010).

The significant increase in the U values and U/Yb ratios after 62 Ma may be indicative of a major input of subducted sediments (Grimes et al., 2015). Ti contents indicate crystallization temperatures between 679 and 937°C, which also suggests the presence of hot and cold granitic magmas (Miller et al., 2003) (**Fig. 2.5D; 2.7A**). Estimates of crustal thickness further indicate that zircons crystallized in both a normal (41 ± 6 km) and a thick (73 ± 9 km) continental crust (**Fig. 2.8A, B**). We interpret that the compositional heterogeneity observed between 62.0 and 50.9 Ma is the result of at least two distinct and unrelated magmatic suites that formed under contrasting crustal architectures.

The *in-situ* plutonic rocks that crystallized between 62 and 50 Ma have geochemical signatures that coincide with those of detrital zircons from the Bogotá Formation (Bustamante et al., 2017; Cardona et al., 2011; Duque-Trujillo et al., 2019a; Leal-Mejía et al., 2019). Crystallization temperatures calculated from whole-rock geochemistry coincide with the bimodal temperatures inferred from Ti content in detrital zircons (whole-rock geochemistry from Cardona et al., 2011; Leal-Mejia et al., 2019) (**Fig. 2.8A**). Additionally, whole-rock isotopic data reveals low and highly differentiated magma sources (**Fig. 2.2; 2.7** e, g; Bustamante et al., 2017). Finally, these plutonic rocks have (La/Yb)n ratios between 9

and 16, which are characteristic of magmas crystallized in a thick continental crust (> 50 km; **Fig. 2.8A**).

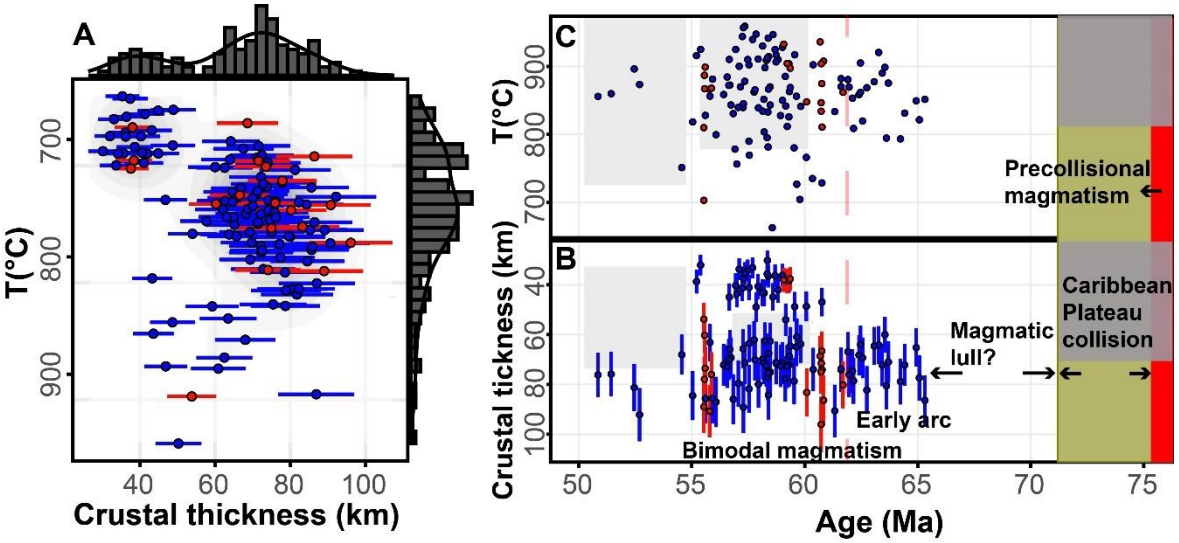

Figure 2. 8. Evaluation of the thickness and temperature of the analyzed zircons. **A**) Crustal thickness (km) vs. Temperature (°C) with marginal histograms showing the subtle bimodal behavior of the data. b) and c) Magmatic history of NW South America during the 75-50 Ma interval. **B)** Age (Ma) vs. Crustal thickness calculated using the methods presented by Tang et al. (2021), **C)** Age vs. Zircon Ti saturation temperature. Legend is the same as **Fig. 2. 6**. The magmatic lull between 72 and 66 Ma, the Caribbean Plateau collision, and the pre-collisional magmatism are indicated with black arrows. Gray squares correspond to changes in temperatures and crustal thickness calculated before published whole-rock geochemistry data (Bustamante et al., 2017; Cardona et al., 2011; Duque-Trujillo et al., 2019a; Leal-Mejia et al., 2019; Rueda-Gutierrez, 2019).

2.5.2.3 Potential tectonic controls for diverse magmatic trends in accretionary orogens: The case of the PECMA in the Northern Andes

Major collisional events on accretionary orogens promote extensive deformation and crustal thickening along continental margins (van Avendonk et al., 2014; Cawood et al., 2013). Such changes in the architecture of the crust can modify the composition of the magmas by providing higher pressures for mineral crystallization and facilitating crustal assimilation (Chapman et al., 2015; Chiaradia et al., 2009; Kay et al., 2014; Profeta et al., 2015). The collision of the Caribbean Plate was one of the major collisional events in the Cretaceous to Cenozoic tectonic evolution history of the Andes and was responsible for the development of high topographic relief (Bayona et al., 2011, 2012; Kennan & Pindell, 2009; Pardo-Trujillo et al., 2020; Villagómez & Spikings, 2013; Zapata et al., 2021). Even though estimates of crustal thickness based on geochemical proxies have noticeable uncertainties

(see section 2.3.3) and values exceeding 60 km can be abnormally high for Andean-type orogens (Kay et al., 1991, 2010), it is considered that the collision of the Caribbean Plate is a tectonic scenario consistent with the development of a thick continental crust. Sixty-nine percent of the Paleocene-early Eocene detrital zircons analyzed provide crustal thickness estimates between 60 and 90 km. Although the precision of these estimates remains contentious, they agree with a significant (>20 km) crustal thickening during the collision of the Caribbean Plate previously proposed based on geochemical and isotopic data of Late Cretaceous and Paleocene plutons (George et al., 2021; Jaramillo et al., 2017; León et al., 2021).

Detrital zircon geochemistry indicates that after 62 Ma, the PECMA was characterized by an increase in the input of subducted sediments, bimodal magmatism, and the coexistence of medium and thick continental crust. The oblique convergence between northwestern South America and the Caribbean Plate margin (Kennan & Pindell, 2009; Montes et al., 2019; Pindell & Kennan, 2009) may account for the magma heterogeneity observed between 62 and 50 Ma. Strike-slip tectonics promoted by oblique convergence was likely to result in coeval transpression and transtension along the continental margin. In this scenario, transtensional settings facilitated the emplacement of juvenile cold and hot magmas under a thin continental crust (McKay et al., 2018; Miller et al., 2003), while transpression maintained the thick continental crust inherited from the collision and promoted high magma differentiation (**Fig. 2.9**).

Strike-slip tectonics during the Eocene have been previously proposed as a potential driver for the arc shut-off (Bayona et al., 2012; Bustamante et al., 2017; Montes et al., 2019). Additional evidence for strike-slip controls has been observed in the dextrally controlled intrusion of several granitoids crystallized between 58 and 50 Ma (Bustamante et al., 2021; Salazar et al., 2016). Although a significant part of the Paleogene magmatic record was lost by erosion or may be hidden in the crust below, older Jurassic and Cretaceous arc plutons found in the Central Cordillera have field expressions that are volumetrically larger than the ones from the PECMA (Bustamante et al., 2016; Gómez et al., 2015), and maybe related to lower magmatic productivity between the Paleocene and the early Eocene. This apparent

reduction of the magma volumes can be interpreted as evidence of oblique convergence (Sheldrake et al., 2020).

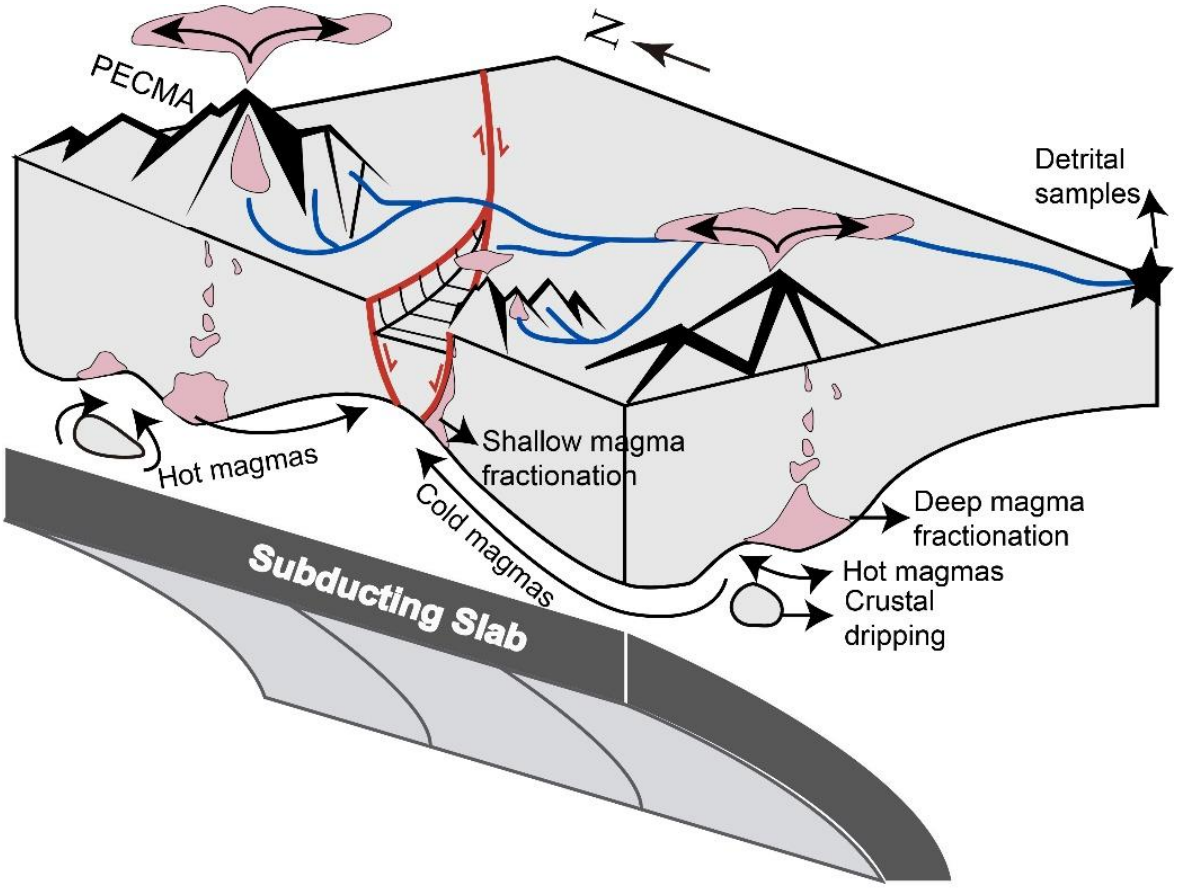

Figure 2. 9. Schematic model of the tectonic process that controlled the evolution of the PECMA between 62 and 50 Ma. This figure shows how a magmatic arc developed on a continental margin dominated by strike-slip tectonics can be characterized by magmas emplaced at different depths and hot magmas produced by crustal dripping.

Our data can be partly explained by oblique convergence and strike-slip tectonics. During transtension, magmas are formed under a locally thinned continental crust as a consequence of mantle decompression (Kohut et al., 2006; Waldbaum, 1971), and in this extensional setting, water-rich mantle reservoirs produce cold magmas (<800°C) while drier reservoirs generate hotter melts (>800°C) (Holtz & Johannes, 1994; Miller et al., 2003).

The occurrence of hot magmas formed under a thick continental crust inferred from our data (**Fig. 2.8A, B**) is not fully explained by strike-slip tectonics. We suggest that in addition to strike-slip tectonics, lithospheric sinking may have driven mantle upwelling and melting, favoring the generation of hot magmas under thick crustal domains (Kay & Kay, 1993). This

process can take place at local and regional scales, producing delamination and dripping, respectively, and is associated with the development of a thickened crust that is susceptible to becoming detached (see reviews in Beall et al., 2017; Ducea et al., 2021a, b).

Orogen-scale changes in crustal thickness (up to 40 km) have been documented in several orogens, such as the Himalayas, the Central Andes, and Baja California, as a result of major collisional events, crust delamination, and continental extension, respectively (Chen et al., 2020; Priestley et al., 2019; Schmitz et al., 2021). We propose that the combination of a prior thickened crust, local crustal extension, and lithospheric dripping in a scenario of strike-slip tectonics may be responsible for the coexistence of normal and thick continental crust between 62 and 50 Ma in the Northern Andes.

2.6 Conclusions

Detrital zircon age distribution suggests that after the accretion of the Caribbean Plate at 72 Ma, the continental arc magmatism was re-established under a thickened (>55 km) mixed oceanic-continental crust at least by 66 Ma, earlier than previously proposed (62 Ma).

Geochemical signatures of detrital zircons show the existence of both high- and low-pressure fractionation of hot and cold mantle-derived magmas.

Oblique tectonics is a plausible mechanism that explains the development of a thinned continental crust that coexisted with a prior thickened crust. Additionally, the presence of zircon crystallized in hot magmas and formed in a thick continental crust may be the record of mantle upwelling related to local crustal sinking (dripping) along the continental margin.

Strike-slip deformation combined with local crustal sinking (dripping) tectonics is a plausible mechanism to explain the observed variations in crustal architecture associated with local magmatic differentiation in contrasting crustal architectures between 62 and 55 Ma.

2.7 Supplementary figures

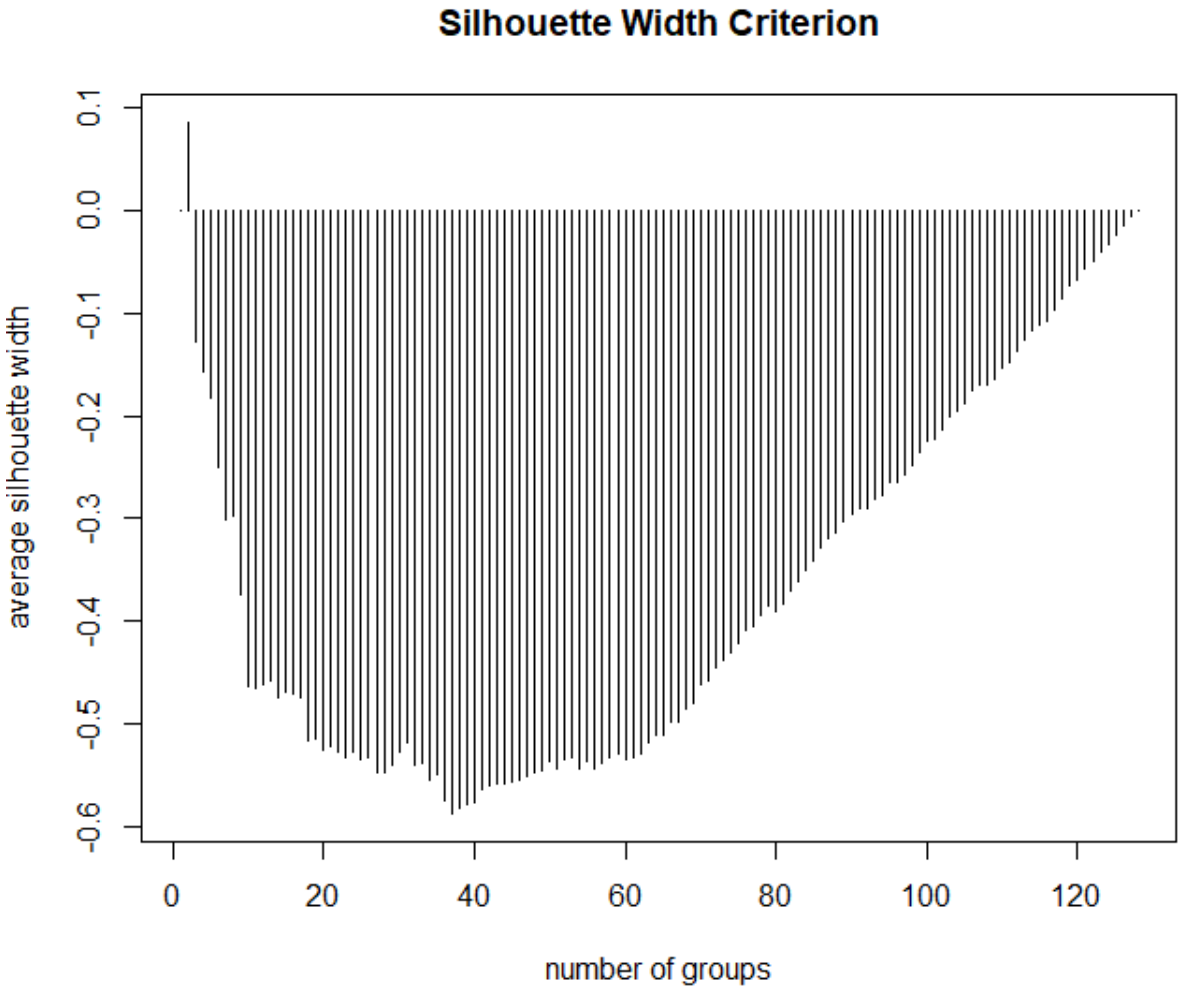

Figure 2. S 1. Silhouette width criterion (Kaoungku et al., 2018) showing the optimal number of the cluster of 2 groups (66-62 and 62-50 Ma).

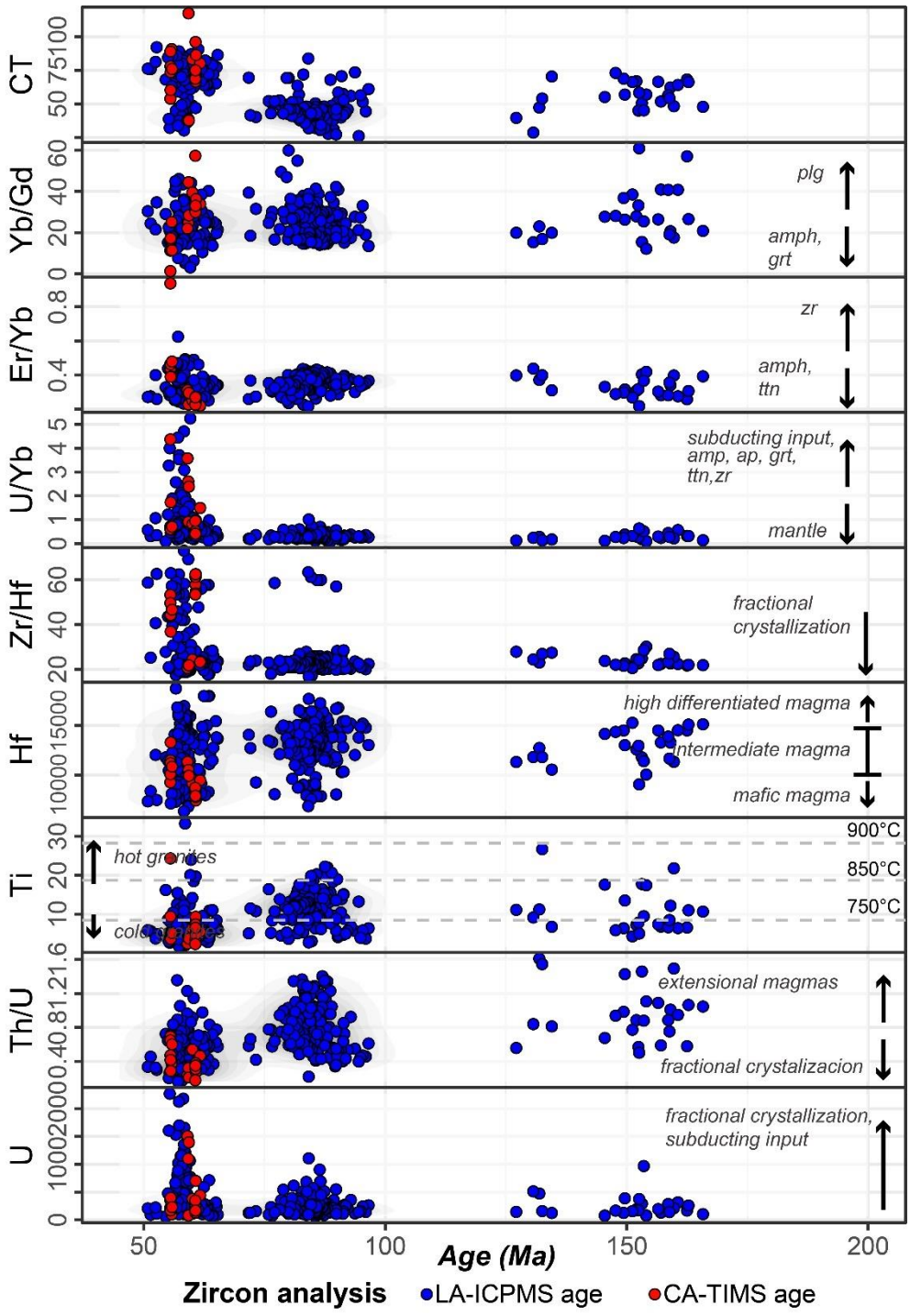

Figure 2. S 2. Cretaceous-Paleocene zircon geochemistry concerning zircon age**. A)** Age (Ma) vs. U (ppm). **B)** Age (Ma) vs. Th/U. **C)** Age (Ma) vs. Ti (ppm) and their inferred saturation temperatures (Ferry and Watson, 2007). **D)** Age (Ma) vs. Hf (ppm). **E)** Age (Ma) vs. Zr/Hf. **F)** Age (Ma) vs. U/Yb ratios. **G)** Age (Ma) vs. Er/Yb ratios. **H)** Age (Ma) vs. Yb/Gd ratios. Annotations are from Barth et al. (2013), Belousova et al. (2002), Claiborne et al. (2006; 2010), Grimes et al. (2015), Kirkland et al. (2015); McKay et al. (2018); Profeta et al. (2015); Sundell et al. (2021); and Yang et al. (2012)—CT=Crustal thickness.

CHAPTER 3

3. A mantle origin for Pliocene SiO_2-rich ignimbrites in the modern Colombian magmatic arc

3.1 Abstract

The generation of voluminous SiO_2-rich magmas has been extensively investigated due to their petrologic implications and because they pose a significant natural hazard. Two main petrogenetic models have been proposed to explain these volcanic products: partial melting of the continental crust and fractional crystallization and assimilation of mantle-derived magmas. In the central segment of the modern Colombian magmatic arc, the northernmost Andean magmatic arc, the eruption of voluminous rhyolitic pyroclastic rocks occurred at 2.6 Ma, covering an area of ~3000 km^2. This contribution presents Hf-Nd-Sr-Pb whole-rock isotopes, zircon U-Pb geochronology, and major/trace-element data from Pliocene rhyolitic ignimbrites and Quaternary andesitic lava flows from the modern Colombian magmatic arc to understand the mechanisms responsible for the formation of high-silica magmas.

The whole-rock and zircon geochemistry and Nd-Sr-Pb-Hf isotopic signatures indicate that this high-silica magmatism is mantle-derived and underwent extensive crystal fractionation and limited assimilation of the continental crust. Extreme magma fractionation at low temperatures and crustal thicknesses above 45 km could have favored the production of cumulates and fast (<5 Ma) crustal thickening. These results highlight the major role of the mantle in generating high-silica magmatism and the associated crustal thickening, a process that has been poorly understood in the Northern Andes.

Keywords: Voluminous SiO_2-rich volcanism; LA-ICP-MS geochronology; Sr-Nd-Pb-Hf isotopes; Basalt underplating; Crustal thickening; Andean orogen.

3.2 Introduction

Magmatism and crustal structure are deeply related in Andean-type margins; crustal architecture influences magma production, composition, fractional crystallization, depth of magma crystallization, and ascent characteristics, which in turn results in major modifications of the continental crust (Jagoutz and Klein, 2018; Kay et al., 1991). For instance, crustal thickening can be related to structural shortening or the underplating and intrusion of mafic and intermediate magmas in the crust (Attia et al., 2022; Ducea et al., 2015b; Haschke and Günther, 2003).

Recognizing the role of each of these mechanisms and their relationship with tectonics and magmatism is a significant research topic for the understanding of the cyclic behavior of long-term convergent margins (Capaldi et al., 2021; Ducea et al., 2015b).

Crustal thickening and the eruption of high-silica magmas are relatively common processes in Andean margins (e.g., Ducea et al., 2015b; Kay and Kay, 1993; Kay et al., 2011). High-silica rocks are widely studied because they contain valuable information about magma genesis and provide insights into major tectonic changes associated with the transition between steady-state and flare-up magmatism (de Silva and Kay, 2018; de Silva et al., 2015) and are also potential risks for populations living in volcanic areas (Pyle, 2015).

High-silica volcanic rocks (>70 SiO_2 wt.%) are mainly found as thick pyroclastic flows that include ignimbrites, eruptive falls, and caldera collapse deposits (de Silva et al., 2015). These pyroclastic flow deposits are frequently associated with caldera-forming eruptions, which can reach hundreds to thousands of cubic kilometers, covering areas wider than 105 km^2 (Bachmann and Bergantz, 2008; Best et al., 2016; de Silva et al., 2015; Gravley et al., 2016). High-silica eruptions have been related to two endmember models: 1) Anatexis of the lower crust (Caffe et al., 2012; Foley et al., 2023); 2) fractional crystallization, differentiation, and crustal assimilation of mantle-derived melts (Bachmann et al., 2014; Best et al., 2016; Ducea et al., 2021a; Hildreth and Moorbath, 1988). Both endmembers in arc-related settings have been associated with modifications in mantle flow induced by changes in the subduction angle (Best et al., 2016; Kay et al., 2011) or delamination promoted by crustal thickening (Ducea et al., 2021b; Gall et al., 2021; Kay and Kay, 1993).

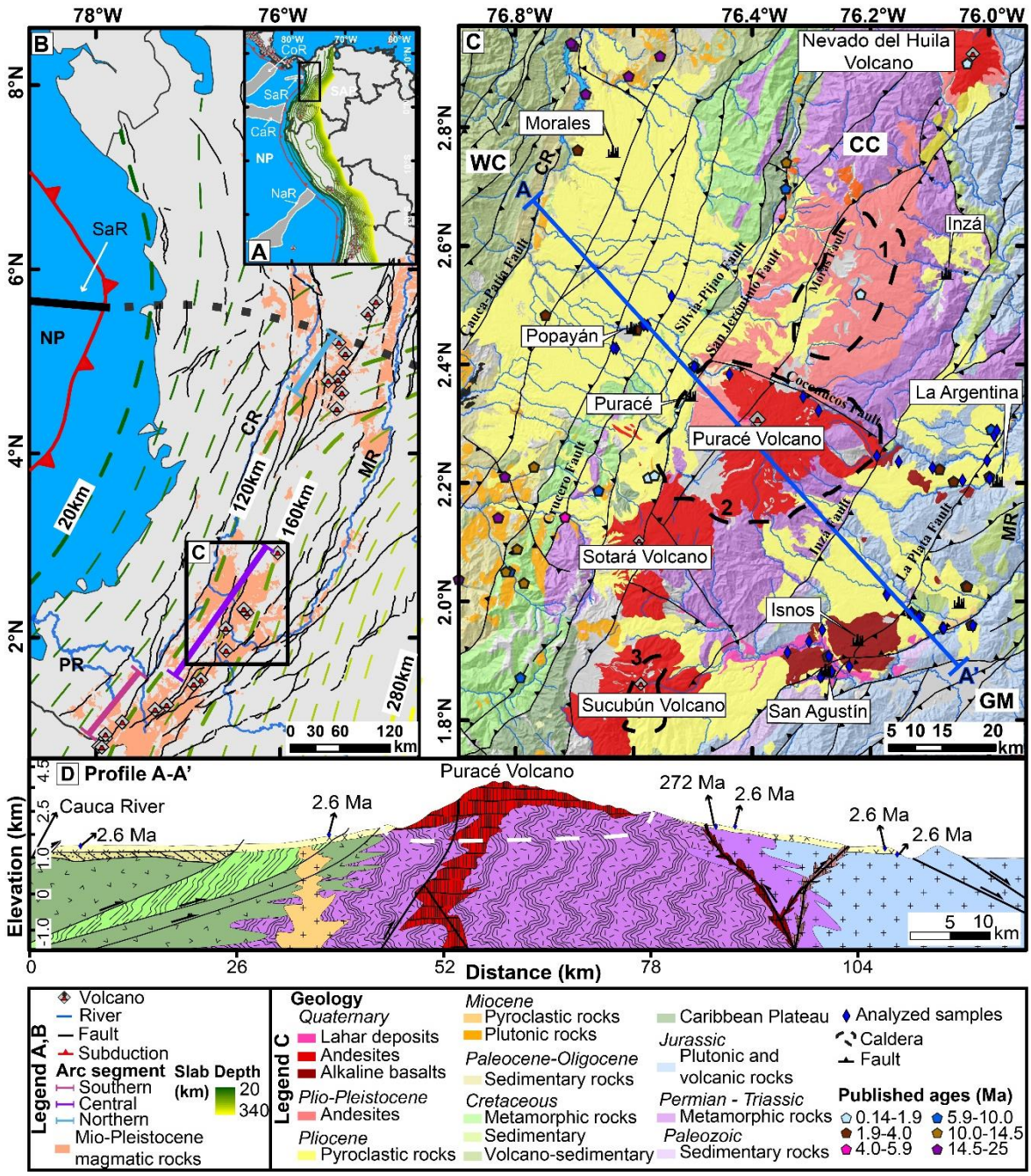

Figure 3. 1. Geological map of western Colombia, including the study area. **A)** Distribution of the frontal arc in the Andean chain with oceanic ridges. **B)** Colombian subduction setting and the volcanic products since the Miocene with subducting slab depths. **C)** Local geology of the study area. NP: Nazca Plate; SAP: South American Plate; CaR: Carnegie Ridge; CoR: Cocos Ridge; NaR: Nazca Ridge; SaR: Sandra Ridge; WC: Western Cordillera; CC: Central Cordillera; GM: Garzón Massif; CR: Cauca River; MR: Magdalena River; PR: Patía River; volcanic calderas correspond to 1: Gabriel López Caldera; 2: Paletará Caldera; 3: Cutanga Caldera (Modified of Gómez and Montes, 2020). **D)** Schematic geologic profile A-A' showing the recent tectonic configuration of the study zone.

The modern magmatic arc front in the Colombian Andes, located between 0.8 and ~5.5°N, is controlled by the subduction of the Nazca Plate (**Fig. 3.1A, B**). This arc has produced high-Mg# (>55) andesitic and dacitic calc-alkaline volcanic flows (Droux and Delaloye, 1996; Errázuriz-Henao et al., 2019; Monsalve-Bustamante et al., 2020). The magmatic evolution of this volcanic arc has been attributed to the differentiation of mantle-derived melts with minor crustal assimilation (Droux and Delaloye, 1996) and significant input from the subducted sediments (Errázuriz-Henao et al., 2019; Marín-Cerón et al., 2010). The central segment of the modern Colombian magmatic arc, in addition to the calc-alkaline andesitic and dacitic flows, is characterized by the production of voluminous Pliocene high-silica pyroclastic rocks and the presence of mantle and lower crust xenoliths into mid-Pliocene pyroclastic rocks (Rodriguez-Vargas et al., 2005; Weber et al., 2002).

A multi-analytical approach, including petrography, whole-rock geochemistry, Sr-Nd-Hf-Pb isotopes, and zircon U-Pb geochronology on silicic pyroclastic rocks from the central segment of the modern Colombian magmatic arc (**Fig. 3.1C**), was conducted to explore the relations between the formation of high-silica magmas and their effect in the crustal evolution. These two processes are key for understanding convergent margins.

Results suggest that the high-silica magmas that formed these pyroclastic rocks were produced from a mantle-derived source that underwent intense fractional crystallization with a minor contribution (< 10%) of continental crust or slab-derived sediments. We also discuss how the ascent and crystallization of these magmas contribute to crustal thickening due to magmatic addition below the base of the crust, presenting an example of the major role mantle-derived magmas played in the modification of the continental crust in Andean-type orogens.

3.3 Geological Setting of the Northernmost Andes

Colombia, located in the northernmost Andes (**Fig. 3.1A**), is characterized by three mountain ranges: Eastern, Central, and Western cordilleras, which are divided by the intermountain Magdalena and Cauca rivers (**Fig. 3.1B**). The Eastern and Central cordilleras are characterized by Precambrian to Miocene rocks with continental affinity (See Bayona et al., 2020; Bustamante et al., 2017; Cardona et al., 2018 for detailed descriptions), while the

Western Cordillera is characterized by allochthonous oceanic-related blocks accreted to the continental margin during the Late Cretaceous (Villagómez and Spikings, 2013) and lower Miocene (Montes et al., 2015; León et al., 2018). The interactions between the Caribbean, Nazca, and South America plates controlled the Neogene geological evolution of the Colombian Andes. The Nazca Plate currently subducts in a SW-NE direction at a velocity of ~58 mm/yr (Mora-Páez et al., 2019). This plate includes several aseismic ridges (**Fig. 3.1A**), such as Carnegie (0°-1°S) and Sandra (~5.5°N), which formed during the Oligocene-Miocene break-off of the Farallon Plate (Lonsdale, 2005).

The Nazca Plate in front of Colombia can be divided into two segments, North and South of the Sandra Ridge at ~5.5°N (Fig 1A). The northern segment is characterized by the absence of polygenetic volcanism, which has been related to flat subduction (Chiarabba et al., 2015; Syracuse et al., 2016; Wagner et al., 2017) since 5.2 Ma (Jaramillo et al., 2019) and restricted Quaternary monogenetic volcanism (Sánchez-Torres et al., 2022). In contrast, the southern segment has a subduction angle of 40°-35° (Wagner et al., 2017), producing a well-defined magmatic arc front (Errázuriz-Henao et al., 2019; Monsalve-Bustamante, 2020).

The modern Colombian magmatic arc front is divided into southern, central, and northern segments (**Fig. 3.1B**), typically producing calc-alkaline andesites and dacites with Mg# >55 and SiO_2 ranging from 50 to 66 wt.%. These geochemical compositions have been related to mantle-derived melts with a low contribution of continental materials (Droux and Delaloye, 1996; Errázuriz-Henao et al., 2019; Marín-Cerón et al., 2010; Monsalve-Bustamante, 2020).

The central segment of the modern Colombian magmatic arc, where the study area is located, includes six active volcanoes: Doña Juana, Las Ánimas, Sucubún, Sotará, Puracé, and Nevado del Huila (Monsalve-Bustamante, 2020; **Fig. 3.1C**). These volcanoes are intruding Permian-Triassic schists, gneisses, and metaluminous to peraluminous plutonic rocks in the axis of the Central Cordillera (**Fig. 3.1C**). Magma emplacement in this segment was associated with the NE Silvia-Pijao and San Jerónimo regional fault systems and the Moras and Coconuco faults (**Fig. 3.1C**).

In the central arc segment, the slab subducts with a dip angle of ~35° and reaches depths between ~150 and ~160 km under the active Puracé and Nevado del Huila volcanoes (Hayes

et al., 2018; Rosenbaum et al., 2021). Crustal thickness at this latitude is still a topic of debate, with estimates ranging between 48 to 68.5 km based on teleseismic receiver functions and xenolith data (Avellaneda-Jiménez and Monsalve, 2022; Poveda et al., 2015; Zieman et al., 2023).

3.3.1 Upper Miocene to Quaternary magmatic record in the central segment of the modern Colombian magmatic arc.

The Upper Miocene magmatic record in the central volcanic segment of the modern Colombian arc is characterized by volcaniclastic deposits and relatively minor intrusions (Gil-Rodriguez, 2014; van der Wiel, 1991). Several plutons of calc-alkaline diorite-tonalite compositions and ages between ~12 and 9 Ma are found in the western flank of the Central Cordillera (Gil-Rodriguez, 2014; Leal-Mejía et al., 2019), while the volcaniclastic Gigante Formation is mainly exposed in the Upper Magdalena Valley (see **Fig. 3.1** for location). The Gigante Formation consists of interbedded conglomerates, sandstones, mudstones, lahar deposits, and high-silica ignimbrites with ages between 9 and 6 Ma (Anderson et al., 2016; van der Wiel, 1991).

Pliocene volcanic deposits are grouped into the Popayan and Guacacallo formations, which include ash fall, debris avalanches, block-and-ash flows, and ignimbrites exposed in both flanks of the Central Cordillera **(Fig. 3.1C**; Kroonenberg et al., 1981; Torres-Hernández, 2010). These units overlie Permian-Triassic metamorphic, Jurassic igneous-volcanic, and pre-Miocene sedimentary rocks (**Fig. 3.1C**) with stratigraphic thicknesses between 20 and 700 m and a mean of 120 m (Kroonenberg et al., 1981; Torres-Hernández, 2010; van der Wiel, 1991). The Guacacallo and Popayan formations cover an area of 1200 and 1800 km^2, respectively. Unlike the Gucacallo Formation, the Popayan Formation presents andesitic flows at the base of the sequence, followed by thick pyroclastic deposits. The pyroclastic rocks from the Popayan and Guacacallo formations are characterized by high-silica (>65 wt.% SiO_2) calc-alkaline compositions and K-Ar, apatite fission track, and zircon U-Pb ages between 3.3 and 2.3 Ma (Kroonenberg et al., 1981; Sanín et al., 2022; Torres-Hernández, 2010; van der Wiel, 1991). Additionally, olivine basalts-andesites and scoria-cone deposits

associated with monogenetic volcanism overlie and cut the Guacacallo Formation (Monsalve-Bustamante, 2020).

Stratigraphic evidence has been used to relate the pyroclastic rocks from the Guacacallo and Popayan formations with the Paletará Caldera, which have an average diameter of 32.8 km and covers an area of ~845 km^2 (Samacá-Torres, 2016; **Fig. 3.1C**). However, some of this volcanic material may have also been produced by other calderas such as Gabriel Lopez and Cutanga, with areas of ~489 and ~73 km^2 respectively (Kroonenberg et al., 1981; **Fig. 3.1C**).

In Marcaderes region, Mid-Pleistocene ignimbrites from Doña Juana-Petacas volcanoes at the south of the central arc segment contain mantle and lower crust xenoliths, including garnet-bearing gabbros and lherzolites, pyroxenites, and hornblendites with ages between 5.2 and 0 Ma (Bloch et al., 2017; Rodriguez-Vargas et al., 2005; Weber et al., 2002; Zieman et al., 2023). These garnet-bearing pyroxenites, gabbros, and hornblendites have been interpreted as arclogites, which could be related to high-pressure transformed magmatic cumulates and restites after the partial melting of basaltic magmas at the base of the continental crust (Gianola et al., 2023).

3.4 Analytical methods

3.4.1 Zircon U-Pb LA-ICP-MS Geochronology

Zircons were extracted at Zirchron LLC, Tucson, AZ. Rock fragments were placed in the sample chamber of an Electro Pulse Disaggregator (EPD, Marx generator), then electrical pulses were applied at 1 Hz repetition and discharges of ~250kV for 15 minutes. The sample material passing through the 350 µm disposable stainless steel mesh sieve is collected in a plastic bag. Material is then processed following traditional methods using the Wilfley water table, Frantz® paramagnetic separator, and one-step (3.32 g/cm^3) heavy liquid separations. Zircon grains were then mounted in epoxy resin discs and then polished.

Zircon U-Pb ages were measured at the Radiogenic Isotope and Geochronology Lab (RIGL) at Washington State University using an Analyte G2 193 excimer laser ablation system coupled with a Thermo-Finnigan Element 2 single-collector, inductively coupled, plasma mass spectrometer. The laser parameters were 35 µm in diameter spot size, 10 Hz

repetition rate, and ~5.5 J/cm^2. For the U-Pb measurement, we mostly followed the method of Chang et al. (2006), except for the use of the 193 nm laser system instead of the 213 nm laser. A 10-second blank measurement of the He and Ar carrier gasses (Laser off) before each analysis followed by 250 scans across masses ^{202}Hg, ^{204}Pb+Hg, ^{206}Pb, ^{207}Pb, ^{208}Pb, ^{232}Th, ^{235}U, and ^{238}U during ~30-second laser ablation period. Analyses of zircon unknowns, standards, and quality control zircon grains were interspersed with analyses of external calibration standards, typically with 10-12 unknowns bracketed by multiple analyses of two different zircon standards (Plešovice and FC-1). The Plešovice standard (337.13 ± 0.37 Ma; Sláma et al., 2008; n=121 ^{206}Pb/^{238}U age=337.3 ± 0.4 Ma) was used to calibrate the ^{206}Pb/^{238}U and ^{207}Pb/^{235}U ages, zircon 91500 (1065 Ma; Wiedenbeck et al., 1995; n=61 ^{207}Pb/^{206}Pb age=1056 ± 3.0 Ma) was used for the calibration of ^{207}Pb/^{206}Pb ages owing to its high-count rate for ^{207}Pb (~2-4 times higher than that of Plešovice). Fish Canyon Tuff (~27.5 Ma Lanphere et al., 2001; n=36 ^{206}Pb/^{238}U age=28.1 ± 0.2 Ma) was used as a quality control standard. Data was processed offline using the Iolite software (Paton et al., 2011). Common Pb correction was performed using the ^{207}Pb method (Williams, 1998). Since young zircons, especially Quaternary, are widely affected by secular disequilibrium of the ^{230}Th-^{238}U during the zircon crystallization (Schärer, 1984), we corrected the ^{206}Pb/^{238}U ratios, following the approach of Sakata et al. (2017) (eq. 8). We use a ratio of Th/U zircon/ Th/U melt partition coefficients (fTh/U) of 0.30 ± 0.16 (1σ). This value was derived from the Th/U measurements of the dated zircons, and the Th/U resulted from the whole rock geochemistry. Plots were calculated using Isoplot 4.15 (Ludwig, 2012).

3.4.2 Zircon Lu-Hf isotopes

After the U-Pb analysis, Lu-Hf isotope compositions of 10-20 selected zircon grains were analyzed using the same laser ablation system coupled with a Thermo-Finnigan Neptune+ multi-collector mass spectrometer. Because the laser beam used for this analysis was 35-40 μm in diameter, only larger zircon grains were selected for this analysis. The laser fluence and repetition rate were the same as U-Pb. This study used the same instrument configuration, operating parameters, and data reduction methods discussed by Fisher et al. (2014), with the exception that U-Pb dates were not simultaneously determined. In this

"dedicated Hf" method, the output from the ablation cell was mixed with N_2 gas and delivered directly to the Neptune MC-ICPMS. To reduce inter-laboratory bias, the Plešovice zircon standard ($^{176}Hf/^{177}Hf$ = 0.282482 ± 13, Sláma et al., 2008) was regularly analyzed between sample blocks and used to correct the measured $^{176}Hf/^{177}Hf$ of unknowns. Given the potentially large range of (Lu+Yb)/Hf in zircon samples, accurate correction for the isobaric interference of ^{176}Yb and ^{176}Lu on ^{176}Hf is imperative and should be assessed using quality control zircons interspersed with samples (Fisher et al., 2014). Throughout this session, quality control zircons agreed well with published MC-ICPMS isotope compositions of purified Hf from these zircons, attesting to the accuracy of the interference correction methods employed.

Internal 2σ precision was typical ~1.1 εHf. Analyses with less than 25 ratios and/or internal 2σ uncertainty over 2 εHf units were discarded and not presented here. Present-day εHf values were calculated using the CHUR parameters reported by Bouvier et al. (2008).

3.4.3 Zircon Chemistry

Zircons large enough to accommodate another laser ablation spot were selected for rare earth element analysis at Washington State University using the same LA-ICP-MS instrument used for U-Pb and Lu-Hf isotope analysis. New laser spots were placed within the same zone for U-Pb and Lu-Hf isotope analyses. Each analysis consists of two cleaning pulses, followed by 10 seconds of washout, 18 seconds of gas blank, and 40 seconds of ablation time, followed by 15 seconds of waiting time before moving the stage. Three standards, including NIST610 and NIST612 (both are synthetic glass standards) and zircon reference 91500, were dispersed every 15 analyses. Correction and data reduction were carried out using the Iolite Software (Woodhead et al., 2007). The temperatures of zircon formations were calculated using the Ti in zircon thermometer (Ferry and Watson, 2007). The $aSiO_2$ for these ignimbrites was considered at 1, and the $aTiO_2$ of 0.6 following the information presented by Hayden and Watson. (2007).

3.4.4 Whole-rock geochemistry

Fifteen samples were chosen, avoiding veins and weathered surfaces for whole-rock chemical analyses. The samples were crushed using a jaw crusher and powdered using a

tungsten carbide ball mill at Zirchron LLC. Major and trace elements were analyzed using a Rigaku 3370 X-ray fluorescence (XRF) spectrometer at the Peter Hooper GeoAnalytical Lab at Washington State University. Details of sample preparation, dilution, and analytical procedures have been described by Johnson et al. (1999). Trace elements, including Rare Earth Elements (REEs), were determined by ICP-MS (Agilent 7700) at Washington State University. A 2g aliquot was weighed into a graphite crucible and mixed with 2 g of $LiBO_2$ flux. The crucibles were placed in an oven and fused at 1000°C in a muffle furnace for 30 min. The resultant bead was ground in a steel ring mill, and a 0.25 mg portion was dissolved using HNO_3 (2 mL), HF (6 mL), and $HClO_4$ (2 mL) at 110 °C. Calibration standards and reagent blanks were added to the sample sequence. Sample solutions were aspirated into an ICP emission spectrograph (Jarrel Ash Atom Comb 975) to determine major oxides and certain trace elements (Ba, Nb, Ni, Sr, Sc, Y, and Zr).

3.4.5 Whole-rock isotopes

Whole-rock Sr, Nd, and Pb isotope composition of four ignimbrites and two andesites were acquired at the RIGL using the Thermo-Finnigan Neptune+ multi-collector system. Results are presented in Table 3.1. After crushing the samples, they were powdered using an agate mill jar and balls at Zirchron LLC. The procedures for Sr, Nd, and Pb isotope preparation are the same as those in Gaschnig et al. (2011). The Sr analyses were corrected for mass fractionation using $^{86}Sr/^{88}Sr = 0.1194$ and normalized using the NBS-987 standard. The average reproducibility, with two standard deviations of $^{87}Sr/^{86}Sr$, was ± 0.00005. The initial isotopic values were calculated using Rb and Sr concentrations from the XRF. The Sm and Nd isotope analyses followed the procedures described in Vervoort & Blichert-Toft (1999). Sm and Nd mass fractionation were corrected using $^{147}Sm/^{152}Sm = 0.56081$ and $^{146}Nd/^{144}Nd = 0.7219$, respectively, and normalized using the Ames Nd standard (±0.000020 2σ average reproducibility). The εNd values were calculated using present-day values of $^{143}Nd/^{144}Nd = 0.512630$ and $^{147}Sm/^{144}Nd = 0.1960$ for CHUR (Bouvier et al., 2008). Pb was separated using the Tl doping method of White et al. (2000). After correcting for the mass bias using the Tl, samples were normalized to the triple-spike values for NBS-981 from Galer and Abouchami (1998).

3.4.6 Isotopic modeling

In this study, we developed 67 Sr-Nd and 10 Pb-Pb isotopic models. We considered the available information on potential host rock contamination suites and mantle sources, including the lower crust and mantle xenoliths exposed in the Mercaderes region (Rodríguez-Vargas et al., 2005; Weber, 1998; Weber et al., 2002). Additionally, Depleted Mantle (Gale et al., 2013) was also modeled with respect to the same potential host rocks. The information on the final isotopic members is presented in Table 3.1.

The end members correspond to the sample XM3, identified as a mantle xenolith (Rodriguez-Vargas et al., 2005), suggesting a potential mantle source. Based on field and petrography information, we assume that these samples may have assimilated schists from the Cajamarca Complex and plutonic rocks from the Permian and Jurassic arcs. Consequently, we calculated a mean isotopic value of the felsic rocks from the Cajamarca Complex (Cochrane et al., 2014; Restrepo et al., 2023; Vinasco et al., 2006). Additionally, we selected sample WR-214 from the Argentina Jurassic pluton (Leal-Mejía et al., 2019), which outcrops around the study area.

Considering the potential increase of sediment dehydration within the subducted slab, we incorporated the isotopic values of the sediments from the Nazca Plate (DSDP 69, site 504; Errázuriz-Henao et al., 2019). The best-fitting models are presented in the text and involve 1) a mixing of the peridotite (mantle) sample with a continental mixing of 60% Argentina pluton and 40% Cajamarca Complex and 2) a mixture of the peridotite (mantle) sample with an 80% of the Argentina pluton and 20% of sediments from the Nazca Plate.

Unfortunately, Pb isotope signatures are not abundant in rocks from the host rock and mantle xenoliths, so these models were developed with fewer samples. The best-fitting involves 1) mixing a hornblendite sample (lower crust) from the Mercaderes locality with a continental mixing of 20% Argentina pluton and 80% sediments from the Nazca Plate.

Data from coherent andesite flows related to the central segment of the modern Colombian magmatic arc is from Correa-Tamayo (2009), Droux and Delalouye (1996), Marín-Cerón et al. (2010), Marriner & Millward (1984); and Monsalve & Pulgarín, (1999); and data from Pliocene ignimbrite are from van der Wiel, (1991). Data from Caribbean Plateau signatures is from Kerr et al. (1996).

3.5 Results

3.5.1 Field Observations

Fieldwork was carried out in the central volcanic segment of the modern arc between the Sucubún and Nevado del Huila volcanoes (**Fig. 3.1C**). The Plio-Pleistocene volcanic deposits in this region are overlying Cretaceous basaltic rocks, Permian-Triassic metamorphic rocks, Jurassic plutonic and volcanic rocks, or Upper Miocene volcaniclastic rocks of the Gigante Formation (**Fig. 3.1C, D**).

Pyroclastic rocks were sampled along three previously recognized stratigraphic sections (**Fig. 3.2**; Kroonenberg et al., 1981; Torres-Hernández, 2010; van der Wiel, 1991). The Popayan and Guacallo formations include pyroclastic density currents – mainly ignimbrites–block and ash, and ash and lapilli fall deposits with thicknesses up to 700 m (**Fig. 3.3A**). Available geological mapping and stratigraphy suggest that the pyroclastic deposits from the Guacacallo and Popayan formations cover an area of ~3000 km^2 and have an average thickness of 120 m (**Fig. 3.1C; 3.2**; Kroonenberg et al., 1981; Torres-Hernández, 2010; van der Wiel, 1991), which could correspond to a bulk porous volume of ~359 km^3.

Ignimbrites have columnar jointing (**Fig. 3B**) and are composed of plagioclase, k-feldspar, quartz, and biotite (**Fig. 3.3C-G**). Accidental lithics can be observed sporadically (**Fig. 3.3C, E, G**). Quaternary lava flows mainly correspond to andesites with lobules and columnar jointing (**Fig. 3.3H, I**). These andesites are characterized by euhedral pyroxene phenocrysts and plagioclase within a gray groundmass (**Fig. 3.3K-N**).

From the bulk 359 km^3 estimated from field relations and stratigraphy for the pyroclastic rocks, a reasonable and very moderate dense rock equivalent (DRE) volume of 155 km^3 was calculated considering a magma density of 2.3 ± 0.14 g/cm^3 for the silicic magma following the Bottinga and Weill, (1970) method, and an average density of 1.0 g/cm^3, for the average of pyroclastic rocks (Pyle, 2015). This is consistent with pyroclastic rocks formed by intermediate to large calderas, such as the case of the Sawtooth Peak in Nevada (Best et al., 2013). However, more detailed stratigraphic columns, remoting sensing and geomorphology, mineral chemistry, and direct density calculations in the pyroclastic rocks need to be performed in this area.

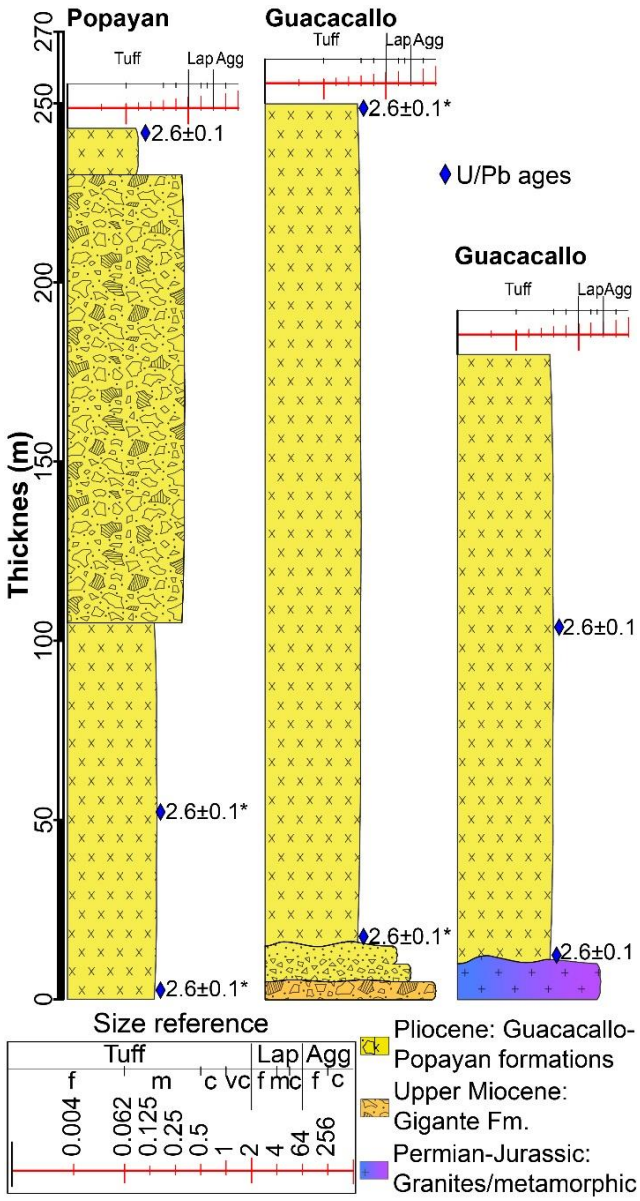

Figure 3. 2. Schematic stratigraphic columns for Popayan and Guacacallo Formations (Torres-Hernández, 2010; van der Wiel, 1991), some samples with geochronology are indicated in the columns; (*) data from Sanín et al. (2022).

3.5.2 Petrography

3.5.2.1 Pyroclastic rocks

Fifteen samples of Guacacallo and Popayan formations were analyzed; their mineral assemblage is dominated by sharp phenocrysts of plagioclase (24-74 vol.%), alkali feldspar (3-28 vol.%), quartz (10-29 vol.%), and biotite (0-10 vol.%). These rocks also contain glass shards and lithic fragments, volcanic (including pumice 0-20 vol.%), plutonic (0-1 vol.%),

fine-grained sedimentary (0-1.4 vol.%), and metamorphic rocks (0-2 vol.%). Zircon and apatite are the main accessories phases. The groundmass is mainly volcanic glass, except for samples V-01 and 21GU-05, where quartz has replaced the matrix. Zircon and apatite are present as accessory minerals. Vesiculation in these rocks can reach up to 8 vol.%.

The main rock texture in the studied samples is eutaxitic, with well-defined pumice fiammes (**Fig. 3.3D-F**). Occasionally, felsitic and spherulitic textures are observed. Jigsaw and embayed textures are evident in most crystals of quartz and feldspar (**Fig. 3.3F**), and disequilibrium textures are recorded by the complex zoning textures in plagioclase.

3.5.2.2 Andesite flows

Seven samples of coherent flows related to the Puracé were analyzed; their mineral assemblage is dominated by plagioclase (andesine, An35-40) (46-56 vol.%), clinopyroxene (18-40 vol.%), and orthopyroxene (7-20 vol.%), with variable contents of amphibole (0.3-3.9 vol.%), olivine (<2.4 vol.%), alkali feldspar (<2.6 vol.%), and traces of quartz (<1 vol.%). The matrix of most samples is composed of volcanic glass (**Fig. 3.3K, L**) except for samples 36074-Me, 36075 Me, and 36081-Po, where plagioclase and clinopyroxene are present in the matrix as tiny lath aggregates. Apatite is the principal accessory mineral phase.

The main textures found in these rocks are trachytic and pilotaxitic. Sporadically, plagioclase shows sieve and swallowtail textures (**Fig. 3.3L, N**). Clinopyroxene, orthopyroxene, and plagioclase are often presented in glomeroporphyritic aggregates. Disequilibrium textures correspond to sieve texture, complex zoning in plagioclase, and the overgrowth of clinopyroxene in orthopyroxenes. The amphibole displays reaction rims and, in some cases, is entirely replaced by opaque minerals due to devolatilization.

3.5.3 U-Pb zircon LA-ICP-MS Geochronology

Different samples located in the base, middle, and top of the stratigraphic sections from both the Guacacallo and Popayan formations were dated to constrain their deposition time. The host rocks, a granitoid sample, and different Upper Miocene and Quaternary volcano-sedimentary rocks were dated to characterize possible magma contaminants and refine the temporal magmatic evolution of this region.

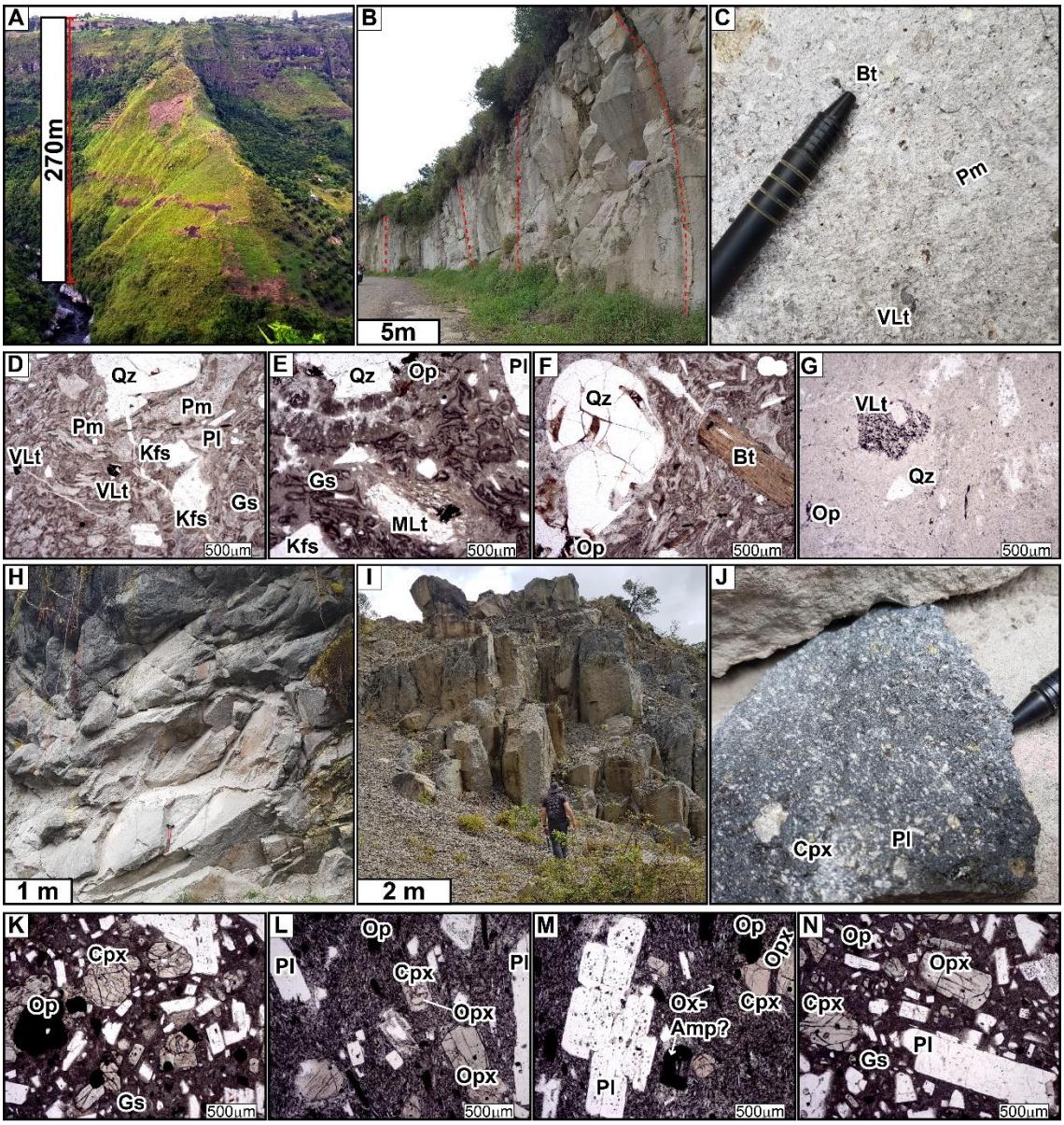

Figure 3. 3. Outcrops and microphotographs of the samples studied here. **A)** Photograph of the landscape showing the ignimbrite thickness (~270 m). **B)** Ignimbrites with columnar jointing (see red dashed lines). **C)** Closeup of ignimbrite rocks, black shapes correspond to biotite crystals and some schist xenoliths. D-G) Ignimbrite microphotographs. **D)** Eutaxitic texture and volcanic glass groundmass. **E)** Volcanic glass groundmass and metamorphic lithic. **F)** Quartz with embay texture and biotite. **G)** Andesitic lithic and groundmass replaced by silica. **H)** Modern andesite lava flow. **I)** Andesite with columnar jointing. **J)** Closeup view of andesite flows with white shapes corresponding to plagioclase crystals. **K-L)** Microphotographs of Quaternary andesite flows; note euhedral Cpx, Opx, and Pl. Groundmass is mainly formed by volcanic glass with some microliths of plagioclase with a trachyte texture. **K)** Clinopyroxene and plagioclase in glassy groundmass. **L)** Overgrowth of Clinopyroxene around orthopyroxene. **M)** Oxides possibly replacing amphiboles and microlites of plagioclase in the groundmass. **N)** clinopyroxene, orthopyroxene, and plagioclase embedded in glassy groundmass. Bt: Biotite; CPx: Clinopyroxene; Opx: Orthopyroxene; Kfs: K-Feldspar; Gs: Glass; Op: Opaque; Pl: Plagioclase; Pm: Pumice; Qz: Quartz; MLt: metamorphic lithic; VLt: Volcanic lithic.

3.5.3.1 Ignimbrites

Between 30 and 50 zircons were analyzed from each of the eight ignimbrite samples. Zircon crystals range from 100 to 500 μm with length-to-width ratios between 2:1 and 5:1 (**Fig. 3.4A**). Cathodoluminescence images show that most zircons have oscillatory zoning (**Fig. 3.4A**), indicating a characteristic magmatic growth (Corfu et al., 2003). Nevertheless, some zircons exhibited sector zoning (**Fig. 3.4B**), which has been related to rapid changes in their temperature and growth rates during crystal formation (Paterson and Stephens, 1992). The ignimbrites have concordant $^{238}U/^{206}Pb$ and $^{207}Pb/^{206}Pb$ isotopic ratios (**Fig. 3.4B**), with similar mean ages of 2.6 ± 0.1 Ma (**Fig. 3.4C**). Some zircons (14 of 348) have ages between 3.3 and 2.8 Ma and are considered antecrysts (**Fig. 3.4B, C**).

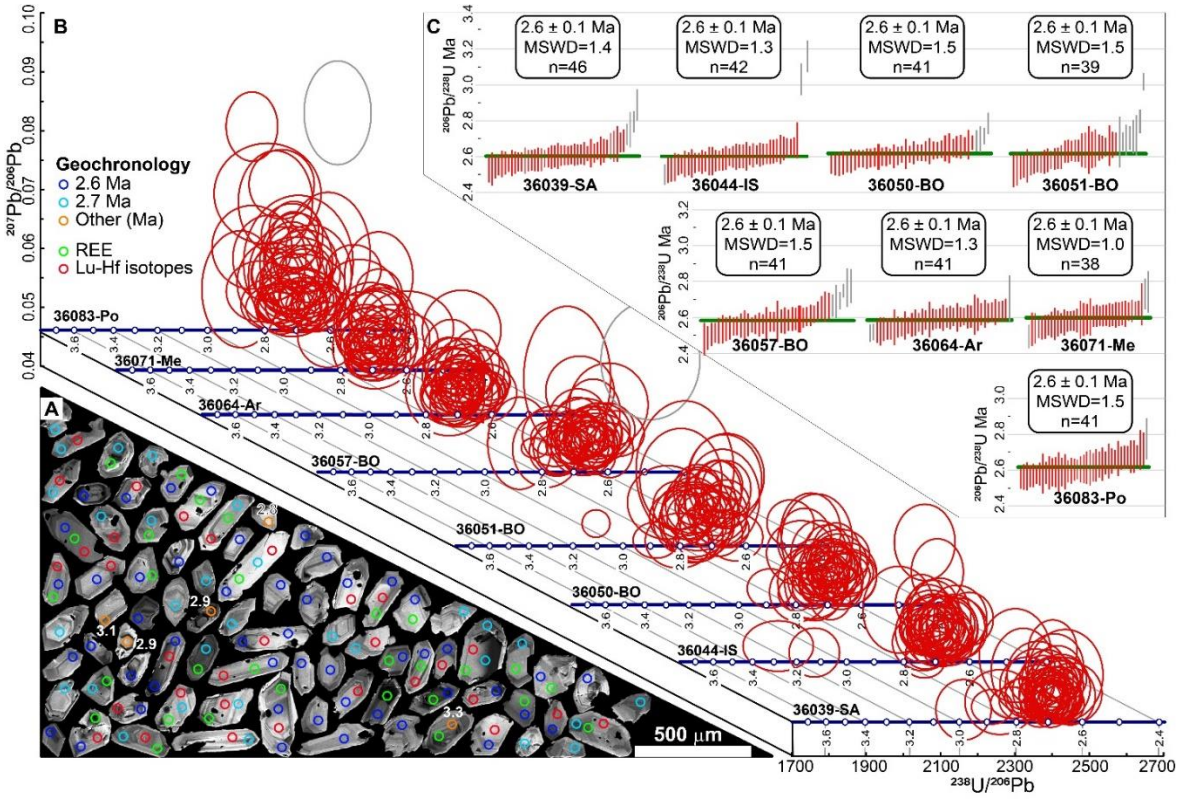

Figure 3. 4. Geochronology results for the analyzed zircons from ignimbrites. **A)** Cathodoluminescence images from representative grains. **B)** Tera-Wasserburg plots between 3.6 and 2.4 Ma for each sample. Gray ellipses correspond to those data with common Pb. **C)** Weighted average plots showing each sample's $^{206}Pb/^{238}U$ central age; gray bars correspond to those data out of the mean values. Bars correspond to 2σ absolute errors.

3.5.3.2 Basement rocks

A total of 47 zircons from a granitoid sample (sample 36072-Me) collected close to the Paletará Caldera were analyzed (**Fig. 3.1C, D**). Zircons range in size from 90 to 500 μm and have a length-to-width ratio between 2:1 and 4:1. Most zircons have oscillatory zoning in cathodoluminescence images (**Fig. 3.5A**), typical of magmatic growth (Corfu et al., 2003). This rock has a concordant $^{238}U/^{206}Pb$ and $^{207}Pb/^{206}Pb$ with a mean crystallization age of 272.2 ± 3.5 Ma (**Fig. 3.5B, C**).

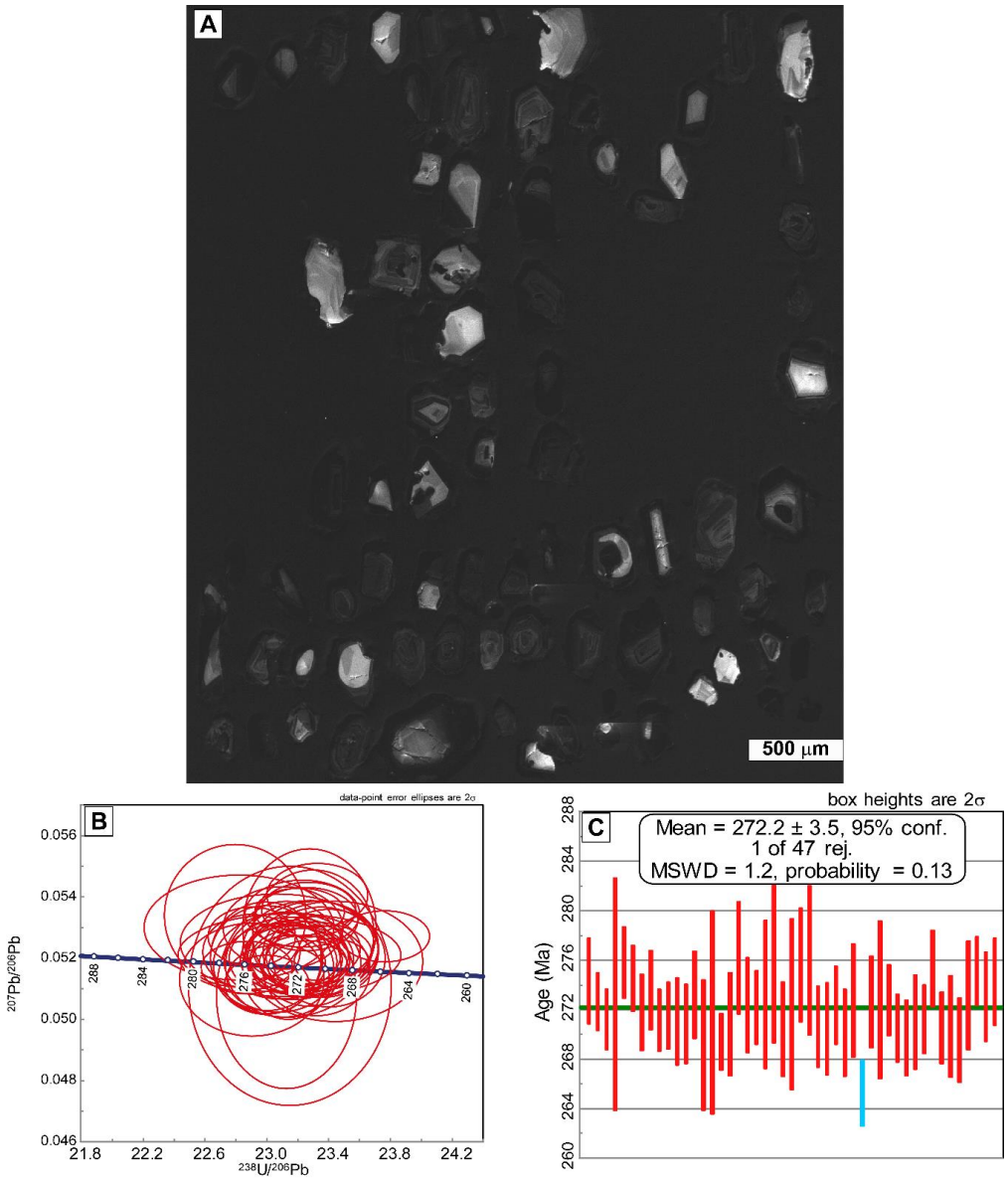

Figure 3. 5. Geochronology of granitic rock from the basement (sample 36072-Me). **A)** Cathodoluminescence image of the analyzed zircons. **B)** Tera-Wasserburg diagram of the analyzed zircons, it is possible to observe that all the zircons were concordant. C) Weighted average age of the sample.

3.5.3.3 Detrital zircons

A total of 517 zircons were separated from seven volcano-clastic rocks from the Gigante Formation and one sample from a Quaternary lahar deposit. Most of these zircons exhibit concordant $^{238}U/^{206}Pb$ and $^{207}Pb/^{206}Pb$ ratios (**Fig. 3.6A**). All mixed samples have prominent age peaks of 132, 141, 150, 183, and 273 Ma, followed by less significant peaks between 960 to 1500 Ma and isolated zircon ages of ~624, 2436, and 2882 Ma (**Fig. 3.6B**).

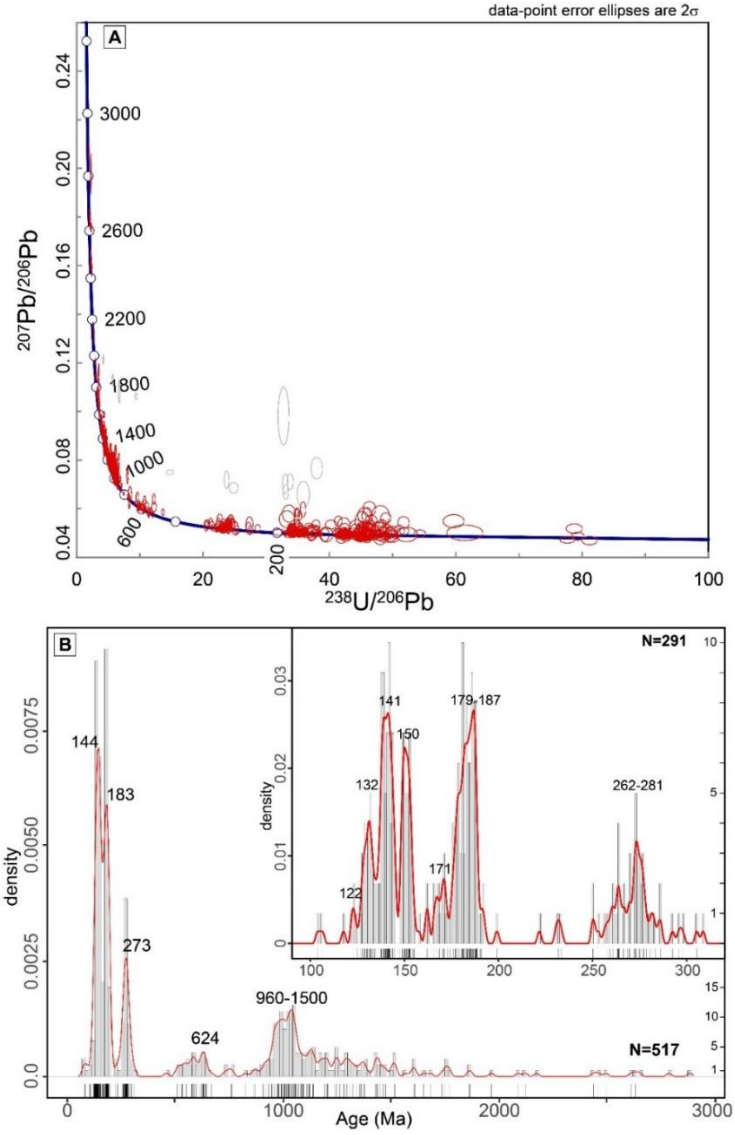

Figure 3. 6. Geochronology of detrital samples 36039-SA 36044-IS, 36050-BO, 36051-BO, 36057-BO, 36064-Bo, 36071-Me, 36083-Po, which correspond to lahar deposits and volcano-clastic sediments of the Gigante, El Carmen, and Altamira Formations. **A)** Tera-Wasserburg diagram of all analyzed zircons, in gray, are all those zircons with discordance >30% or samples with a lot of common Pb. **B)** KDE plots showing the main peaks, inset between 100 and 300 Ma shows the main Paleozoic-Mesozoic washed basements.

3.5.4 Geochemistry

After a careful petrographic revision, we geochemically analyzed nine of the freshest samples of ignimbrites, avoiding samples with veins, accessories, and accidental fragments. Loss on ignition (LOI) values vary between 0.07 and 3.9, with no correlation with SiO_2, Rb, Sr, or Th concentrations (**Fig. 3.7A-C**). The chemical Index of Alteration (CIA) varies between 45 and 56.5, suggesting fresh to weakly altered rocks (**Fig. 3.7D**). Therefore, the major and trace element results should be considered as a reliable proxy for geochemical evaluations. Six samples from the Quaternary volcanic arc were also analyzed to evaluate if the magmas involved in forming the Pliocene high-silica rocks have the same genesis. The geochemistry analysis developed in this study gave very similar results to the geochemistry available to the pyroclastic rocks (Torres-Hernandez, 2010; van der Wiel, 1991) and Puracé Volcano (Marín-Cerón et al., 2010 and references therein) (**Fig. 3.8; 3.9**).

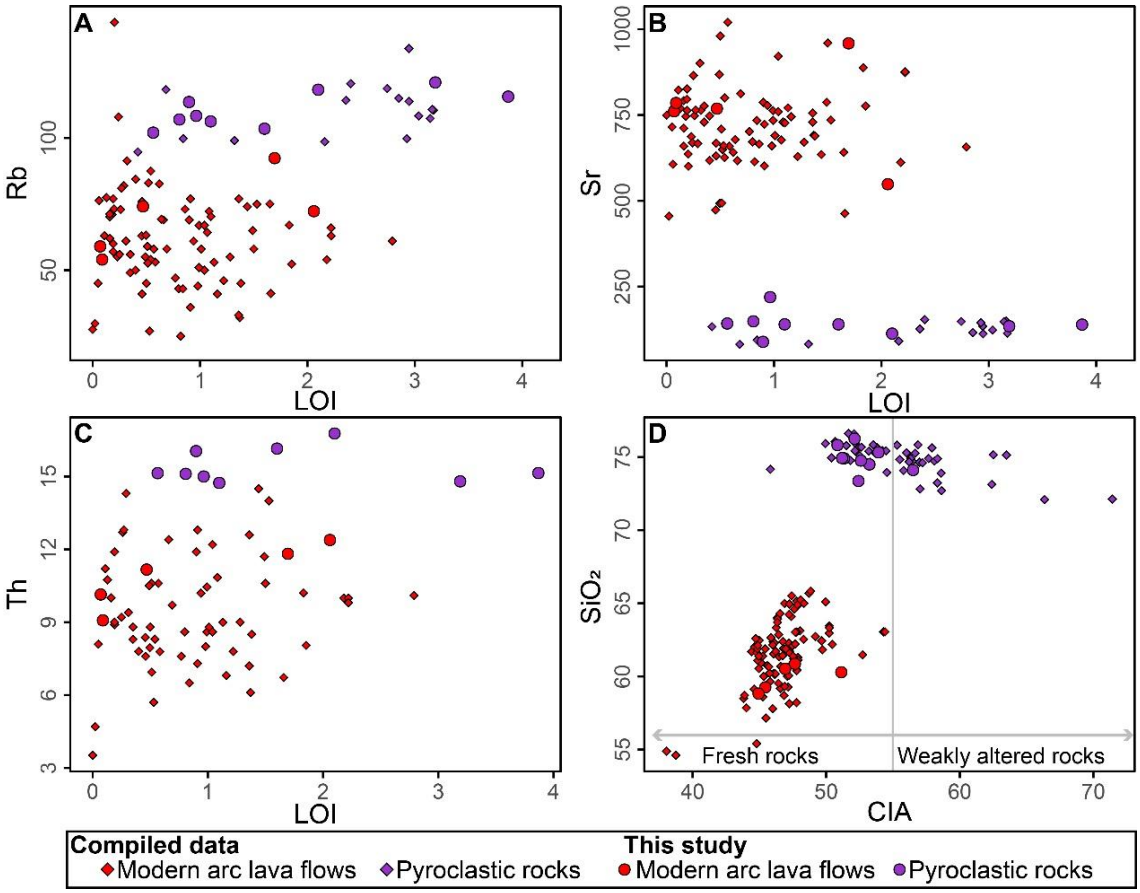

Figure 3. 7. Mobile element variations compared with the Chemical Index of Alteration (CIA; Nesbitt and Young, 1982) and the Loss on Ignition (LOI) for every sample. **A)** CIA vs SiO_2 showing that samples are fresh and only one is weakly altered. **B-D)** LOI vs mobile elements showing an almost flat geochemical behavior in the pyroclastic rocks.

3.5.4.1 Whole-rock Geochemistry in Ignimbrites

The SiO_2 contents from the ignimbrites range from 71.8 to 74.8 wt.%, Al_2O_3 from 13.4 to 15.3 wt.%, FeOt and TiO_2 values are between 0.9 to 1.7 and 0.17 to 0.27 wt.%, respectively (**Fig. 3.8A-C**). Molar Mg# values range from 18.1 to 27.1, Zr content ranges from 126 to 158 ppm (**Fig. 3.8D-E**), and LOI values are between 0.6 and 3.2 for most of the samples, with one sample with a value of 3.9. These rocks are classified as high-K peraluminous rhyolites (**Fig. 3.8F**) with enrichment in Light Rare Earth Element (LREE) with (La/Sm)n between 5.4 and 6.5 and (La/Yb)n values between 11.2 to 17.3 (**Fig. 3.9A**). They also have a general concave-upward pattern in the middle REE (MREE) with (Sm/Yb)n values ranging from 1.8 to 2.7 (**Fig. 3.9B**) and negative Eu anomalies with Eu/Eu* between 0.5 and 0.8 (**Fig. 3.9A**).

Trace-element compositions normalized to primitive mantle (McDonough and Sun, 1995) show well-defined negative anomalies in Nb and Ti and relative enrichment in Cs, Ba, K, and Pb characteristic of magmas formed in subduction-related environments (**Fig. 3.9C**). These rocks also show a relative depletion in Sr and a very strong depletion in P with P_2O_5 between 0.01 and 0.04 (**Fig. 3.9C, D**).

3.5.4.2 Andesite flows

Andesitic lava flows from the Puracé volcano present SiO2 values between 58.4 to 60.1 wt.%, Al2O3 from 16.6 to 17.4 wt.%, FeOt and TiO2 between 5.5 and 6.6, and 0.71 to 0.98 wt.%, respectively (**Fig. 3.8A-C**). The molar Mg# ranges from 47.3 to 54.8, Zr from 136 to 182 ppm (**Fig. 3.8D-E**), and LOI from 0.5 to 1.7. These rocks are classified as medium to high K calc-alkaline andesites (**Fig. 3.8F**).

These rocks are enriched in LREE (**Fig. 3.9A**) with (La/Sm)n between 3.2 and 4.0 and (La/Yb)n between 6.9 and 13.8 and also show a flat slope between the MREE and HREE with (Sm/Yb)n from 1.9 to 3.5 (**Fig. 3.9B**). Flat to subtle negative Eu anomalies are also characteristic with Eu/Eu* values between 0.85 and 0.94.

Trace-element compositions show well-defined negative Nb and Ti anomalies and relative enrichment in LILEs as well as Cs, Ba, K, Pb, and Sr, which are also characteristic of subduction-related environments (**Fig. 3.9C**). These samples also show depletion in Sr, Eu, and P, with P_2O_5 values between 0.19 and 0.32 (**Fig. 3.9C, D**).

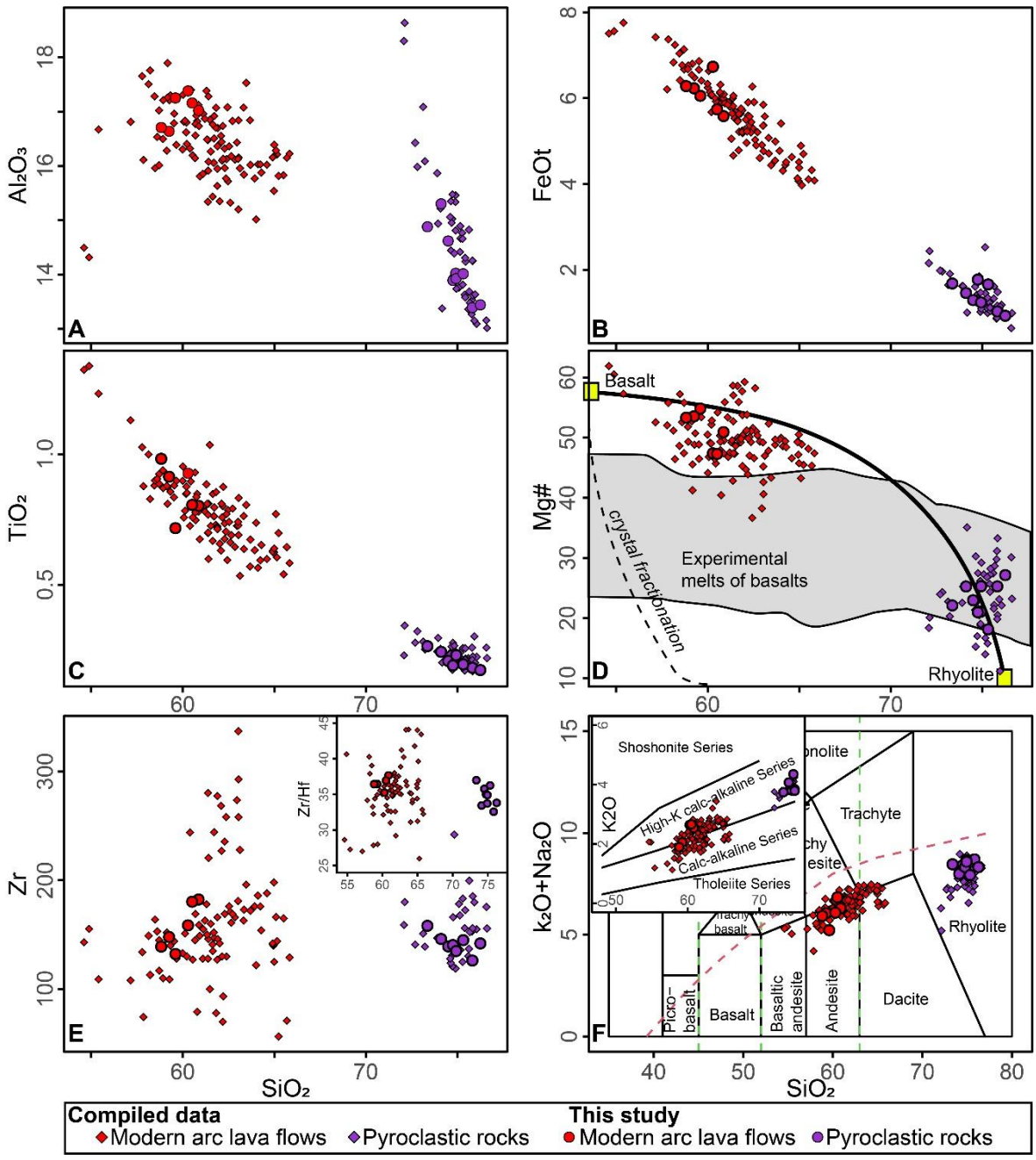

Figure 3. 8. Harker and classification diagrams. SiO_2 wt.% vs. **A)** Al_2O_3. **B)** FeOt. **C)** TiO_2. **D)** Mg# [Mg# = molar MgO/(FeO* + MgO)*100], yellow squares denote a basalt and rhyolite modeled from the Trans-Mexican Volcanic Belt, and the dotted line denotes crystal fractionation, whereas the solid line denotes a simple mixing model (Gómez-Tuena et al., 2014). **E)** Zr (ppm) (inset shows SiO_2 wt.% vs Zr/Hf ratios). **F)** Classification diagram using the total alkalis (Le Bas et al., 1986), inset shows geochemical series (Peccerillo and Taylor, 1976). References from compiled data of lava flows from the central segment of the modern Colombian magmatic arc are presented in the supplementary data.

3.5.4.3 Zircon geochemistry

Zircons from the eighth-dated ignimbrites exhibit Th/U ratios ranging from 0.4 to 6.2 (**Fig. 3.10A**), characteristic of igneous rocks (Rubatto, 2002). The Hf ranges from 6,680.6 to 10,658.6 and Ti from 4.4 to 5.5 ppm (**Fig. 3.10B**), indicating temperatures between 719 and 738 °C (Ferry and Watson, 2007). Zircons show flat to negative Eu anomaly and strong enrichment in HREE with Yb contents between 419.0 and 5,619 ppm (**Fig. 3.10C**). Due to the high compatibility of U in zircon lattice and the Yb being a mineral fractionated in the presence of garnet, the U/Yb ratios for zircon chemistry is a powerful tool to identify the magmatic source of zircons (Grimes et al., 2015). All zircons studied have U/Yb ratios higher than 0.3 (**Fig. 3.10D**), corresponding to zircons from magmatic arcs and showing an enrichment trend that could be related to amphibole or garnet fractionation. Yb/Gd ranges between 8.3 and 45.7 (**Fig. 3.10E**). The Dy concentration suggests almost two different trends when compared with Yb/Dy ratios (**Fig. 3.10F**).

3.5.4.4 Lu-Hf isotopes in zircon

$^{176}Lu/^{177}Hf$ isotopes were measured in 10-20 zircons from each pyroclastic rock dated by U-Pb. $^{176}Lu/^{177}Hf$ isotope values of 163 zircons were analyzed from the volcano-clastic sediments and the Permian granitic rock.

Ignimbrites have $^{176}Hf/^{177}Hf_{(2.6)}$ values between 0.28294 and 0.28306, corresponding to εHf values between 5.5 and 9.8 with εHf mean values between 7.2 and 7.8 (**Fig. 3.11A**). The antecrysts show $^{176}Hf/^{177}Hf_{(2.8\text{-}3.3)}$ ratios between 0.282988 and 0.0.283116 and εHf values between 7.2 and 11.2 (**Fig. 3.11A**). Zircons from the Permian basement (granitoid) has lower $^{176}Hf/^{177}Hf_{(272)}$ values from 0.28245 to 0.28262, corresponding to εHf between -5.7 and 0.3. εHf recalculated to 2.6 Ma ranging between -11.6 and -5.6 with a mean of -7.2 (**Fig. 3.11A, B**).

Detrital zircons from the volcano-clastic samples show significant isotopic variations. Upper Jurassic-Lower Cretaceous present $^{176}Hf/^{177}Hf_{(123\text{-}157)}$ (n=44) ranging from 0.282478 to 0.283019, corresponding to $\varepsilon Hf_{(123\text{-}157)}$ values between -7.6 and 11.4. Lower-Middle Jurassic zircons (n=42) have $^{176}Hf/^{177}Hf_{(171\text{-}193)}$ ranging from 0.282411 and 0.282908, and $\varepsilon Hf_{(171\text{-}193)}$ values between -9.2 and 8.5. Permian zircons (n=12), have $^{176}Hf/^{177}Hf_{(259\text{-}293)}$

ranges from 0.282366 and 0.282772 that correspond $\varepsilon Hf_{(259\text{-}293)}$ values between -8.7 and 5.6. Finally, Precambrian zircons (n=71) show $^{176}Hf/^{177}Hf_{(906\text{-}2785)}$ ratios ranging from 0.280730 and 0.282451, which correspond to $\varepsilon Hf_{(906\text{-}2785)}$ values between -2.3 and 9.6.

The εHf values recalculated to an age of 2.6 Ma, which is the age of the high-silica magma forming, range from -13.0 to +5.3 for the Mesozoic zircons, with a single value reaching +8.4 (**Fig. 3.11A**). Permian zircons also show variation in εHf between -14.5 to -0.2. In contrast, Proterozoic zircons have $\varepsilon Hf_{(2.6)}$ values between -32.6 and -10.7 (**Fig. 3.11A**).

3.5.4.5 Whole-rock Sr-Nd-Pb isotopes

Four ignimbrites and two andesites from the Puracé volcano (before being analyzed by geochemistry) show uniform Sr, Nd, and Pb isotopic compositions. The ignimbrites have initial $^{87}Sr/^{86}Sr_{(2.6)}$ values ranging from 0.704487 to 0.704550 and $^{143}Nd/^{144}Nd_{(2.6)}$ values from 0.512756 to 0.512764, corresponding to $\varepsilon Nd_{(2.6)}$ values between 2.3 and 2.5 (**Fig. 3.11C, D**). Additionally, $^{206}Pb/^{204}Pb$, $^{207}Pb/^{204}Pb$, and $^{208}Pb/^{204}Pb$ ratios range from 18.9755 to 18.9882, 15.6452 to 15.6466, and 38.8187 to 38.8299, respectively (**Fig. 3.11E**). In comparison, the andesites have $^{87}Sr/^{86}Sr_{(0)}$ values between 0.704316 and 0.704318, $^{143}Nd/^{144}Nd_{(0)}$ values range from 0.512776 to 0.512791, which correspond to $\varepsilon Nd_{(0)}$ values between 2.7 and 3. $^{206}Pb/^{204}Pb$, $^{207}Pb/^{204}Pb$, and $^{208}Pb/^{204}Pb$ range from 18.9710 to 18.9924, 15.6427 to 15.6482, and 38.8089 to 38.8338, respectively (**Fig. 3.11C-E**).

3.6 Discussion

The northernmost Andes magmatic arc is characterized by the production of high Mg andesites and less abundant dacites and basalts (**Fig. 3.8D**; Bustamante-Monsalve, 2020; Errázuriz-Henao et al., 2019; Marín-Cerón et al., 2010). Voluminous high-silica magmas are not common within the Neogene magmatic history of this Andean segment. Therefore, understanding the petrogenetic evolution of the high-silica magma will provide insights into the evolution of Andean-type magmatism and the relationship between the high-silica magma production and fast crustal thickening.

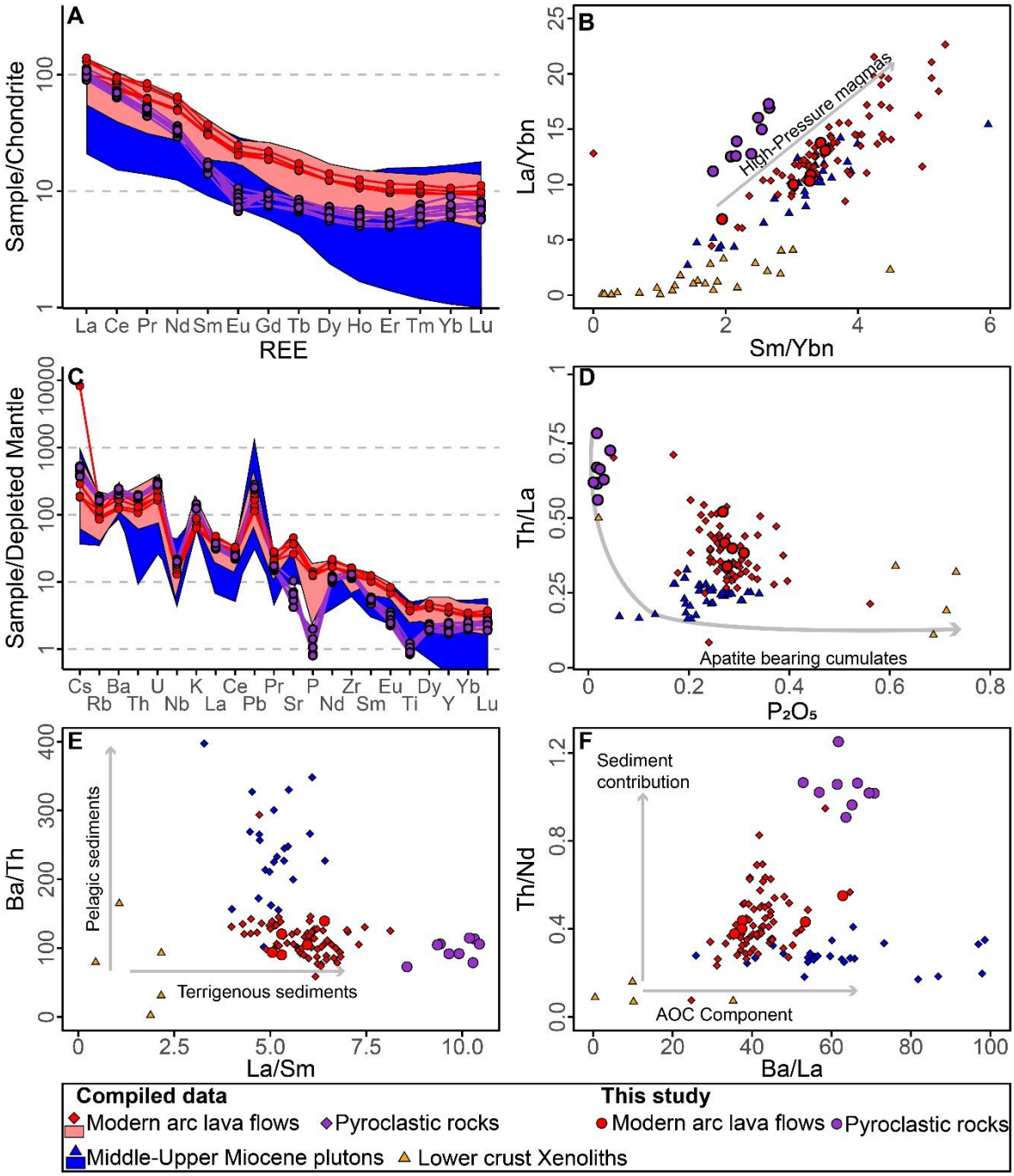

Figure 3. 9. Diagrams of whole-rock trace elements. **A)** Multielement diagram normalizing samples to C1 chondrite (McDonough and Sun, 1995). **B)** Sm/Yb and La/Yb normalized to chondrite, showing the trend of high-pressure magmas, **C)** Multielement diagram normalizing samples to Primitive Mantle (McDonough and Sun, 1995). **D)** P_2O_5 wt.% vs. Th/La, with the trend of apatite bearing cumulate (Cai et al., 2023). **E)** La/Nb vs. Th/Nb. Compiled data of Middle-Upper Miocene plutons is from Gil-Rodríguez (2014) and lower crust xenoliths from Weber et al. (2002).

3.6.1 Formation of high-silica magmas in the central segment of the Northernmost Andean arc

Zircon U-Pb geochronological data shows that a voluminous (~359 km^3) province of rhyolitic ignimbrites was formed at ~2.6 Ma in the same position as the Quaternary andesites from the central segment of the modern Colombian magmatic arc (**Fig. 3.4**). The obtained εHf values and zircon hafnium content, together with whole-rock geochemistry, suggest that these high-silica magmas were formed from a mantle-derived source.

The mean zircon εHf value of +7.5 recorded in the ignimbrites from the central segment of the modern Colombian magmatic arc can be related to mantle-derived magmas with limited assimilation (<10%) of the lower crust (Vervoort and Patchett, 1996). This value is similar to the mean εHf of +7.2 value observed in Quaternary andesites from this arc segment (Marín-Cerón et al., 2010). Both values are lower than the mean εHf of +10.7 recorded in mantle xenoliths from Mercaderes (**Fig. 3.11A**; Bloch et al., 2017). If these xenoliths are considered the mantle that originates the high-silica and andesitic magmas, it suggests a mantle origin for the magmas that generates both the high-silica and andesitic rocks, with some incorporation of the less radiogenic subducted sediments or continental crust. Moreover, sixty-nine of the analyzed zircons (69) have Hf contents below< 9000 ppm, which is characteristic of zircons derived from mafic magmas (Belousova et al., 2002).

The Eu and Sr depletions observed in the whole-rock geochemistry in the ignimbrites (**Fig. 3.9A, C**) suggest that the magmas were formed by low-temperature crystallization and were fractionated from a basaltic source (Lee and Bachmann, 2014; Rudnick, 1992). Whole rock and zircon geochemistry suggest that the magmas that formed the ignimbrite province were characterized by significant fractional crystallization after mantle magma extraction. The studied ignimbrites correspond to High-K peraluminous calc-alkaline rhyolites with SiO_2 > 70, low Al_2O_3, TiO_2 wt.% contents, and highly depleted P (**Fig. 3.8A, C; 3.9C**). The high SiO_2 values and the high Rb and Th suggest that the magma that generates the ignimbrites experienced high fractional crystallization (**Fig. 3.12A**). Zr and Zr/Hf values are usually employed to evaluate differentiation processes in magmatic suites (Claiborne et al., 2006; Linnen and Keppler, 2002). Fractional crystallization experienced by the magmas that formed the ignimbrites is also suggested by the high range (0.4 to 6) of zircon Th/U variations (Claiborne et al., 2010; Kirkland et al., 2015).

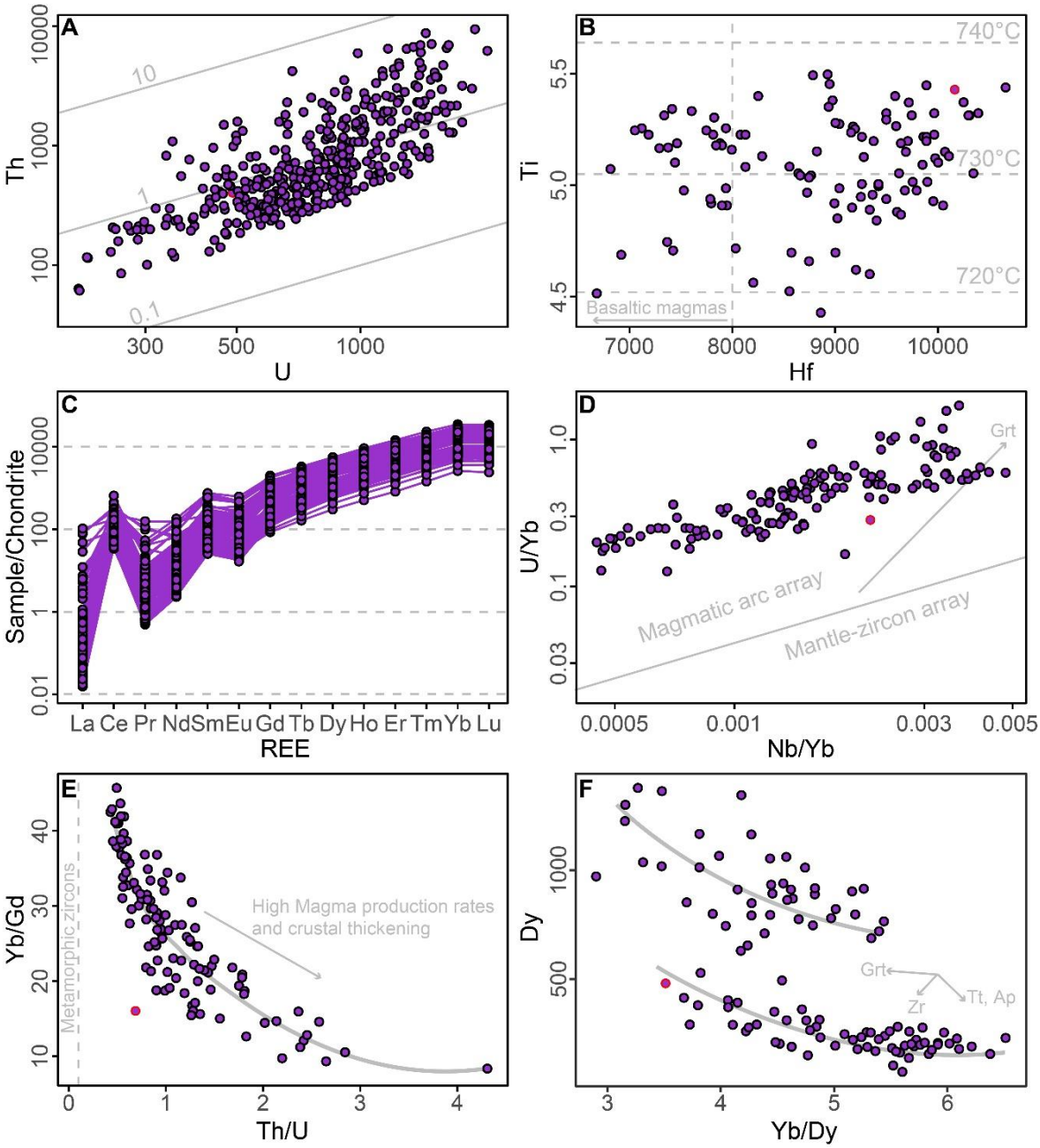

Figure 3. 10. Zircon chemistry. **A)** Th vs U diagram and Th/U ratios. **B)** Hf vs. Ti. Temperature (°C) was calculated using Ferry and Watson's (2007) method. **C)** Multielement diagram normalized to chondrite C1 (McDonough and Sun, 1995). **D)** Nb/Yb vs. U/Yb discrimination between mantle and magmatic zircons (Grimes et al., 2015). **E)** Th/U vs. Yb/Gd showing the trend line. **F)** Yb/Gd vs. Gd diagram showing magmatic trends.

As Zr and Hf are incompatible elements highly partitioned by amphibole and zircon crystallization in arc-related magmatism (Lee and Bachmann, 2014; Linnen and Keppler, 2002), the residual melt should be enriched in Zr/Hf ratios due to fractional crystallization,

same could be achieved by the Rb and Nd highly fractionated by biotite and amphibole, respectively. Since both the Quaternary andesites and ignimbrites show similar values Zr, Hf, and Zr/Hf values to different SiO_2 values (**Fig. 3.8E**) but different Rb/Nd trends (F**ig. 3.12B**), it is possible to suggest that these rocks were formed since different magmatic sources.

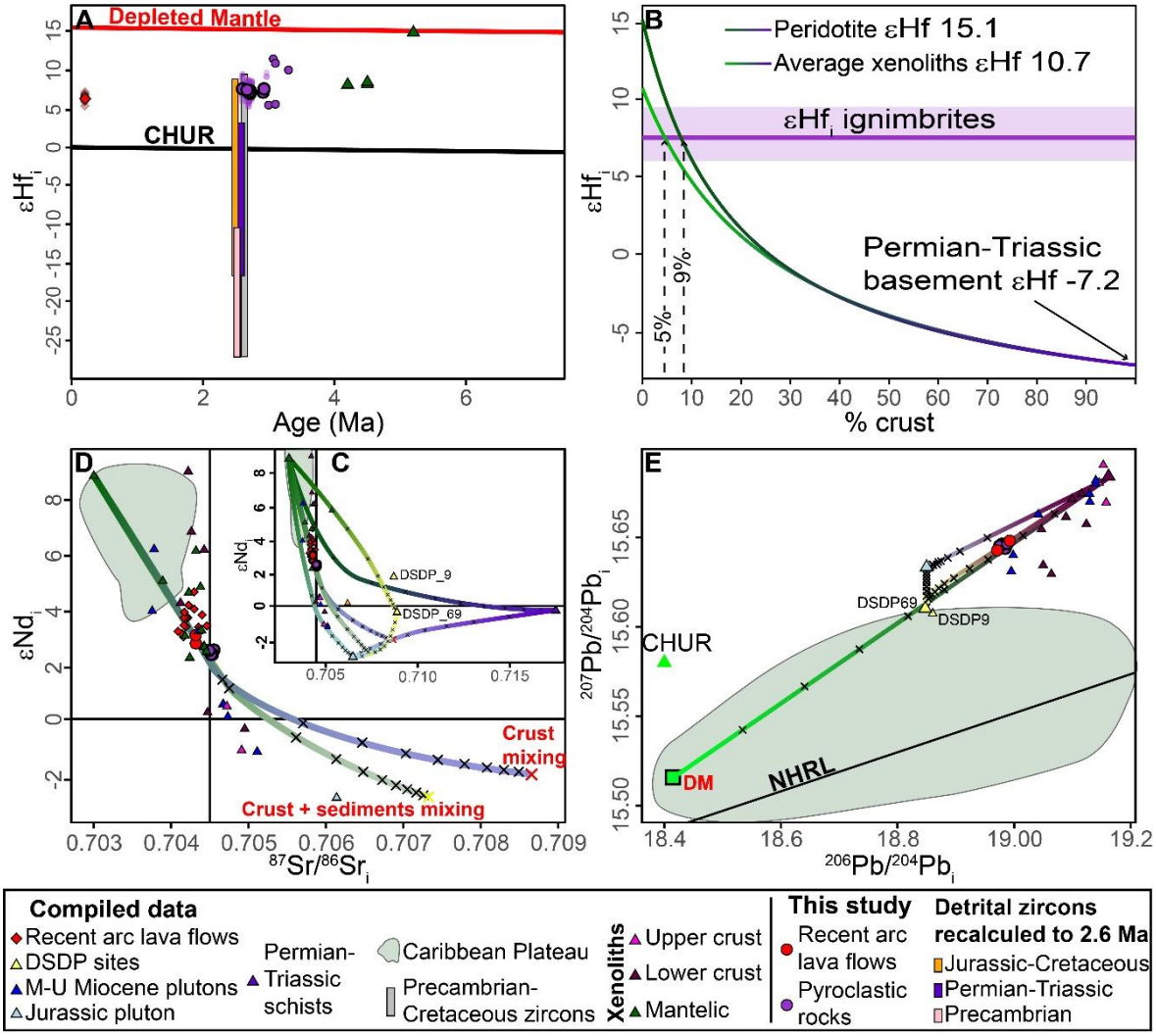

Figure 3. 11. Isotopic data plots. **A)** Ages vs. εHf showing the isotopic behavior of the rhyolites, recent arc lavas (Marín-Cerón et al., 2010), mantle xenoliths (Bloch et al., 2017), and the basement rocks recalculated to 2.6 Ma. Dashed lines indicate the εHf values. **B)** isotopic modeling considering εHf values from the mantle xenoliths (Bloch et al., 2017) and Paleozoic basement. **C)** $^{87}Sr/^{86}Sr_i$ vs εNd_i plot showing the samples and the isotopic model. **D)** Close-up view of $^{87}Sr/^{86}Sr_i$ vs. εNd_i with the best fitting models. **E)** $^{206}Pb/^{204}Pb_i$ vs. $^{207}Pb/^{204}Pb_i$ showing the best fitting models. Caribbean Plateau signatures. The black crosses in C, D, and E correspond to 10% melting. The information on the end members and models is presented in section 3.4.6.

Fractional crystallization is often associated with crustal assimilation. However, our geochemical data and petrographic observations suggest minor crustal assimilation (**Fig. 3.12A-C**). The andesites and rhyolitic ignimbrites show limited variations of the $^{87}Sr/^{86}Sr$ isotopic ratios with respect to the Zr content (**Fig. 3.12C**); conversely, $^{87}Sr/^{86}Sr$ ratios are expected to increase together with Zr contents when crustal assimilation occurs (Schiano et al., 2010).

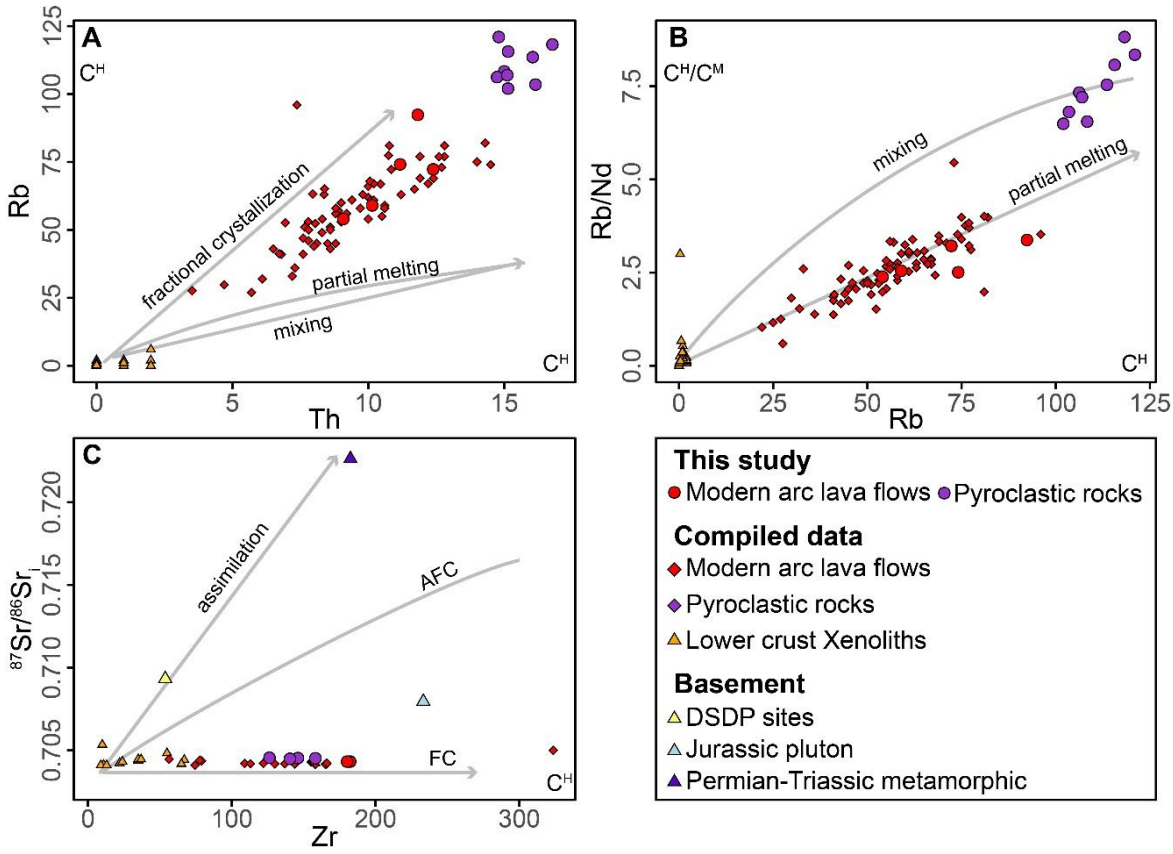

Figure 3. 12. AFC diagrams. **A)** Rb vs Th. **B)** Rb/Nd vs Rb. **C)** $^{87}Sr/^{86}Sr$ vs Zr. CH and CM elements are incompatible (Schiano et al., 2010).

Additionally, the low Al_2O_3 wt.% values in the ignimbrites concerning the Quaternary andesites, together with the absence of high-alumina minerals (e.g., muscovite or sillimanite), can also suggest that the magmas that formed these rocks have limited input from the sialic continental crust. Finally, the limited amount of lithic fragments, as well as the absence of zircon xenocrysts, suggest either that the magma that formed these pyroclastic rocks was fully homogenized after crustal assimilation or that the magma suffered limited assimilation of the host rocks, considering the already discussed evidence the minor crustal assimilation

is the most likely explanation for the lack of zircon xenocrysts. Following these characteristics, late crystallization of plagioclase at high pressures, where pyroxene incorporates high proportions of Al_2O_3, could explain the peraluminous signature of these high-silica rocks (Jagoutz, 2014).

Various isotopic evaluations were performed to quantify the crustal assimilation and evaluate additional sources involved in the genesis and evolution of this magmatism, including the participation of sediments subducted with the slab. εHf values of the Precambrian, Permian-Triassic, and Jurassic-Cretaceous detrital zircons and Permian plutonic rocks together with published data from the literature (Cochrane et al., 2014; Restrepo et al., 2023) were recalculated to 2.6 Ma in order to constrain potential crustal sources. Additionally, different εNd versus $^{87}Sr/^{8}6Sr$ and ^{207}Pb-^{206}Pb combinations (see Text S8) of the mantle xenoliths found in the region (Rodriguez-Vargas et al., 2005) and the Paleozoic-Mesozoic magmatic and metamorphic rocks, that form the basement of the Central Cordillera of Colombia (Cochrane et al., 2014; Vinasco et al., 2006), and marine sediments recovered from the Nazca Plate at Deep Sea Drilling Project -Site 69 (Errázuriz-Henao et al., 2019) were used to constrain the different mantle and crustal inputs.

Mean and maximum εHf values of 10.7 and 15.1 from the mantle xenoliths (Bloch et al., 2017) modeled with Permian-Triassic mean value of -7.2 suggests that between 5 and 9% of continental crust input was necessary to get the isotopic signature recorded by the ignimbrites (**Fig. 3.11B**). The most appropriate εNd and $^{87}Sr/^{86}Sr$ mixing model include 1) Mantle xenoliths, 2) a mix of 60% Jurassic plutonic rocks and 40% of the Permian-Triassic metamorphic rocks, and 3) a mix of 80% Permian plutonic rocks with 20% of marine sediments (**Fig. 3.11C**). This model suggests that the magmas that generated the ignimbrites may have assimilated around 9% of the subducted sediments/crustal-related sources, while the Quaternary andesites assimilated ~8% (**Fig. 3.11D**).

When isotopic Pb is modeled, it is evident that the Quaternary andesites and the high-silica rocks have a close relationship with the lower-crust xenoliths outcropping in the Mercaderes locality (**Fig. 3.11E**). The Pb isotopic model suggests that a mix of 90% lower-crust xenolith and 10% mixing between continental crust and Nazca sediments could generate the isotopic signature of the magmatic rocks studied here (**Fig. 3.11E**).

Dy and Yb concentrations in zircon are useful for discriminating depths of magmatic fractionation. Low values of Yb/Dy correspond to magmas formed at higher crustal depths where garnet or amphibole are stable (Barth et al., 2013). Two chemical clusters with Dy zircon content above and below 520 ppm can be discriminated against (**Fig. 3.10F**). The existence of these clusters could be related to different depths of fractionation associated with higher and lower crustal thicknesses where amphibole or clinopyroxene are stable.

In summary, our petrological, geochemical, geochronological, and isotopic analyses indicate that the voluminous high-silica ignimbrites in the central segment of the modern arc in the Colombian Andes were formed quickly at 2.6 Ma from a mantle source that underwent a high fractional crystallization and assimilated less than 10% of subducted sediments and minor sialic continental crust.

Two main models are usually invoked to explain the generation of high-silica magmas: 1) Fractional crystallization and crustal assimilation from a mantle-derived magma (Bachmann et al., 2014; Best et al., 2016; Chapman et al., 2021); and 2) Partial melting of continental crust (Caffe et al., 2012; Foley et al., 2023).

The most representative voluminous high-silica ignimbrites produced in the Central Andean arc and Great Basin of North America are characterized by magmas formed from subducted-relate melts and significant (>30%) partial melting of a sialic crust (Best et al., 2016; de Silva and Kay, 2018; Kay et al., 2011; Ort et al., 1996). Meanwhile, high-silica ignimbrites in the Ecuadorian Andes have been produced from mantle-derived magma, assimilating less than 20% of a sialic crust (Hammersley et al., 2022), which is a proximal value to those found in this study. Alternatively, high-silica rocks found in New Zealand are a specific example of this kind of magma generated from a mafic parent evolving in a thinner crust (Deering et al., 2011).

Unlike the Central Andes or the Great Basin (Best et al., 2016; Caffe et al., 2012; de Silva and Kay, 2018; Kay et al., 2011; Ort et al., 1996), the high-silica magmas in the central segment of the modern Colombian magmatic arc were formed by low crustal assimilation and significant magmatic differentiation. Developing high-silica magmas formed just by magmatic differentiation is uncommon; consequently, the Northern Andes ignimbrite province represents an analog of these processes in Andean-type orogens.

3.6.2 Tectonomagmatic conditions for producing high-silica Pliocene magmatism in the Northern Andes

A significant increase in mantle-derived magma production in subducted-relate orogens has been related to different processes, including the formation of a slab window associated with ridge subduction (Thorkelson et al., 2011); slab rollback (Best et al., 2016; Gravley et al., 2016), lithospheric delamination (Ducea et al., 2021b; Gall et al., 2021; Kay and Kay, 1993), or increased slab dehydration (Stern, 2020). In this section, we discuss how our findings, in conjunction with a meticulous reassessment of the tectonic framework of the Northern Andes, indicate that slab dehydration was the most plausible mechanism responsible for the intensified Pliocene magmatic activity within the central segment of the modern Colombian magmatic arc.

An increase in dehydration in the slab may be linked to higher amounts of sediments in the subducted plate, subduction erosion (Stern, 2020), and the subduction of a young and hot plate (Syracuse et al., 2010). The Th/La, La/Sm, and Th/Nd ratios are commonly used to evaluate the amount of the terrigenous and pelagic sediments involved in mantle melting due to the affinity of the La, Th, and Ba with marine and terrigenous sources (Plank, 2005; Zhao et al., 2019). Compared with the modern arc and Middle-Upper Miocene plutonic rocks, ignimbrites show higher Th/La, La/Sm, and Th/Nd ratios (**Fig. 3.9D-F**). Additionally, Pb isotopes have revealed significant sediment contribution from the Nazca Plate to the mantle wedge (**Fig. 3.11E**).

The increase in the input of the sediments from the subducted slab could be related to more available sediments associated with the rise in the uplift rates in the Colombian's Central and Western cordilleras after 10 Ma (**Fig. 3.13A, B**), as is evidenced in the forearc and hinterland basins (Echeverri et al., 2015; Zapata et al., 2023). The high exhumation rates facilitate weathering, erosion, and transportation of terrigenous sediments toward the trench. The increase in the subducted sediments promoted higher mantle dehydration rates (Stern, 2020; Zhao et al., 2019) and, consequently, major mantle-derived magma production at 2.6 Ma (**Fig. 3.13C**).

Alternative tectonic processes that may explain the Pliocene increase of magma production beneath the central segment of the Colombian volcanic arc do not align with the Northernmost Andes' regional setting and the geochemical signatures of the studied

ignimbrite province. For instance, a slab window's influence on Pliocene magmatism is diminished, as the Nazca Slab beneath the southern and central Colombian magmatic segment lacks evidence indicative of any subducted ridges (**Fig. 3.1**; Rodríguez et al., 2024). The tectonic scenario of slab rollback and the associated asthenospheric upwelling is incongruent with the observed Pliocene magmatic patterns in the Northern Andes.

Zircon and apatite saturation temperatures from the studied high-silica rocks yield 730-740°C values, similar to the crystallization temperatures of cold silicic magmas (Miller et al., 2003). Such low-temperature magmas differ from the hot melts (~800°C) associated with mantle upwelling during slab rollback (Best et al., 2016). Moreover, the arc front in the central and southern segments has migrated around 40 km between 21 and 3 Ma related to shallowing of the subduction angle (**Fig. 3.13A**; Echeverri et al., 2015), and the cordilleras have experienced significant uplift and exhumation due to compressional deformation (Anderson et al., 2016; Calderón-Diaz et al., 2024; Zapata et al., 2023). This tectonic scenario is opposite to what is seen in a rollback scenario where the arc migrates toward the trench, and extension occurs in the retro-arc position (Nakakuki and Mura, 2013).

Finally, Ignimbrites related to delamination are typically associated with tholeiitic and alkaline basaltic magmatism, commonly exhibiting asthenospheric compositions and high rates of crustal assimilation (Caffe et al., 2012; Gall et al., 2021; Kay and Kay, 1993). High rates of crustal assimilation are not the case for the Pliocene ignimbrites studied here, where high-silica rocks are mantle-derived with a limited (<10%) assimilation of subducted sediments/sialic continental crust (see Section 5.1).

3.6.3 Basaltic magmas as precursors of the SiO2-rich rocks and lower crust high-density rock formation

Magmatism, in addition to tectonic shortening, is fundamental in constructing the continental crust and crustal thickening by magmatic addition (Jagoutz and Kelemen, 2015; Jagoutz and Klein, 2018).

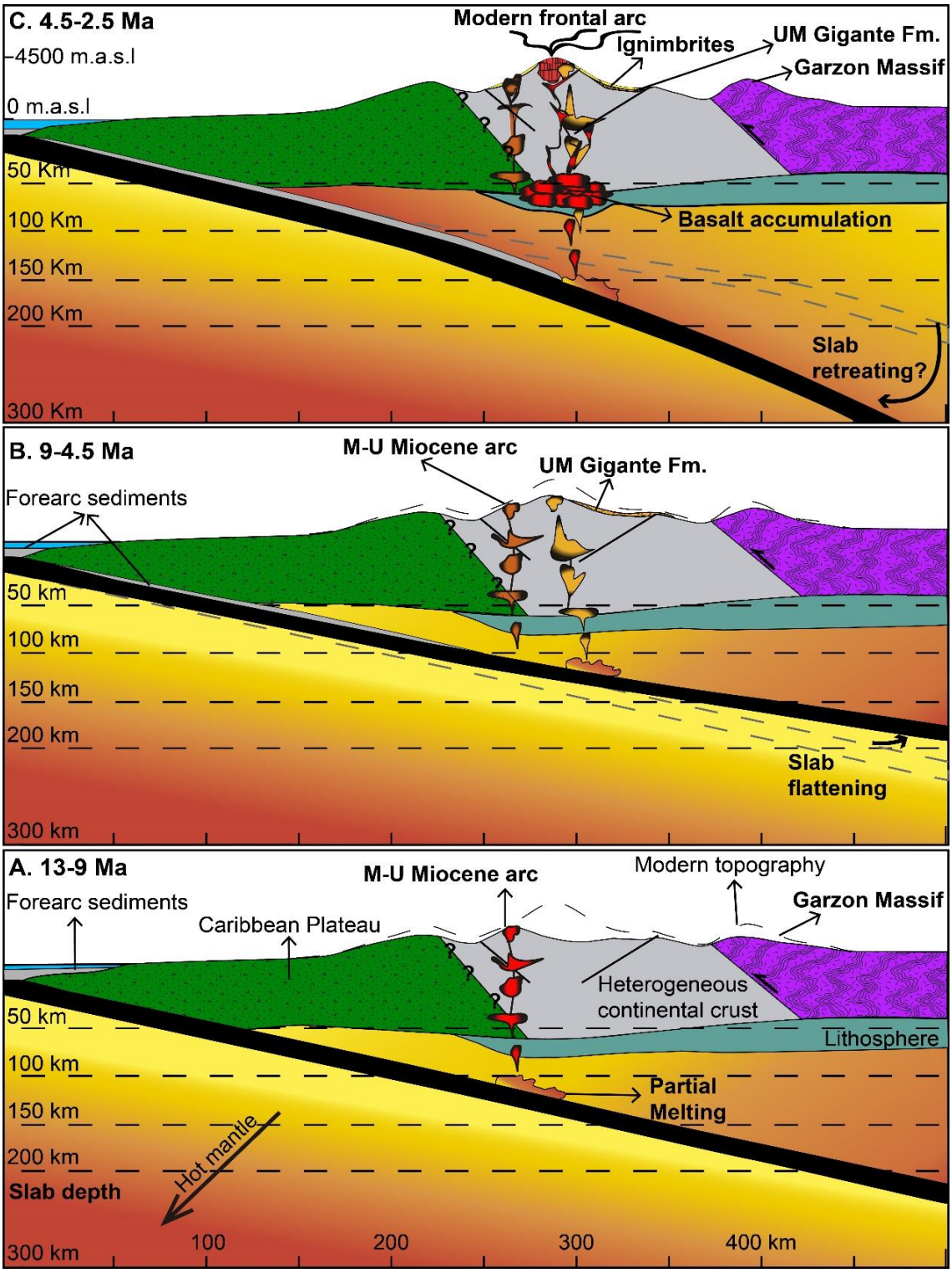

Figure 3. 13. Schematic model of the central segment of the Colombian magmatic arc evolution from mid-Miocene to recent. **A)** Middle-Upper (M-U) Miocene magmatic evolution, **B)** Plio-Pleistocene magmatic evolution, showing the slab flattening and eastward migration of the arc. **C)** Voluminous production of high-silica rocks, with a generation of voluminous restites. The heterogeneous crust refers to the mixing Paleozoic, Mesozoic, and Cenozoic rocks.

Thermobarometric data from lower crust xenoliths in the central segment of the modern Colombian arc, including garnet-bearing gabbros, pyroxenites, and hornblendites, suggests formation pressures between 1.3 and 2 GPa that are equivalent to depths between 50 and 74 km (Bloch et al., 2017; Gianola et al., 2023; Weber et al., 2022; Zieman et al., 2023). These values partially overlap the crustal thickness of 68.5 km derived from receiver functions in the same region (Avellaneda-Jimenez and Monsalve, 2022). Some of these xenoliths present well-defined arc-related geochemistry (Weber et al., 2002), suggesting they were part of the thick arclogitic arc root (Ducea et al., 2021a, 2015b).

Lu-Hf geochronological data have shown that these arclogites crystallized between 5.2 to 0 Ma (Bloch et al., 2017). The older ages are associated with lower crustal thickness (~50 km), while the younger ones could be related to higher crustal thickness (~74 km; Bloch et al., 2017; Zieman et al., 2023).

Ignimbrites are strongly depleted in phosphorus and titanium (**Fig. 3.9C**) and present low Nb/Ta (12-13) and high Th/La ratios (0.6-0.8). These values are associated with apatite, rutile, and Fe-Ti-rich oxide fractionation, which could imply the production of garnet-apatite-bearing cumulates (Cai et al., 2023; Tang et al., 2019a, b), which could be associated with the mineralogy of the arclogites in the Mercaderes locality (Weber et al., 2002). The U-shape in the middle REE (**Fig. 3.9A**), as well as the whole-rock La/Ybn >6 and Sm/Ybn <3 (**Fig. 3.9B**), indicate that the high-silica magmas from the ignimbrites underwent crystal fractionation under moderate-pressure conditions within the amphibole stability field (Balica et al., 2020). Moderate to high pressure is further supported by low zircon Yb/Gd and Yb/Dy ratios and different oxidation states suggested by the Eu/Eu* (**Fig. 3.10C, E, F**), which indicate that zircons were formed at crustal thicknesses between 51 and 65 km (Barth et al., 2013; Tang et al., 2021).

Although volume assessments were not the primary focus of this study, estimations derived from exceedingly conservative thickness and density values revealed volumes on the order of tens to hundreds of cubic kilometers of volcanic materials. These high rates of volcanic production necessitated the generation of plutonic materials, potentially exceeding their volcanic counterparts by at least tenfold in volume (Ducea et al., 2015a; Paterson et al., 2011). These calculations suggest the plausible occurrence of significant crustal thickening

attributable to magma production, which is stuck in the middle crust as stocks or batholiths (**Fig. 3.13C**). To produce 20 km^3 of high-siliceous magma via fractional crystallization, as is the case presented in this study, around ~56 km^3 of mafic cumulates are needed (Jagoutz and Klein, 2018). Due to the volumes evidenced in these high-silica rocks, more than 500 km^3 of mafic cumulates could be pounded in the lower crust in this arc section.

Therefore, in addition to contemporaneous tectonic shortening (Calderón-Diaz et al., 2024; Zapata et al., 2023), mafic underplating in the lower of the crust and intermediated plutonic rocks in the middle and upper crust promoted crustal thickening, which increases the pressure since 5 Ma. This tectonic setting favored the formation of garnet-apatite-rutile bearing cumulates that become the arclogites seen in the crustal xenoliths from this arc segment.

Thus, it seems feasible to consider that a significant increase in crustal thickness (20 km) probably occurred in a period of less than 5 Myr, a rate of 4 km/Myr. This value is like those found in the Famatinian arc, where ~30 km of continental crust was formed by magmatism in ~4 Myr with a rate of 7.5 km/Myr (Ducea et al., 2017), or the Kabye Massif, where ~44 km of continental crust was developed in ~14 Ma with a rate of 3.1 km/Myr (Ganade et al., 2021).

3.7 Conclusions

The geochronological evidence presented in this study for the central magmatic segment of the Colombian Andes demonstrates that the volumetric rhyolitic pyroclastic rocks were generated in a very short period at 2.6 Ma.

The radiogenic, juvenile εHf-εNd values and subtle unradiogenic Sr found in the high-silica rocks result from magmas formed from a mantle source with limited (<10%) crustal assimilation, which is very similar to the Quaternary andesites from the central segment of the modern Colombian magmatic arc.

The data presented in this study suggest that the formation of these Pliocene rhyolitic ignimbrites was associated with a more significant influx of sediments in the subducted slab, triggering the increase of the dehydration and partial melting of the mantle wedge.

The temperatures involved in the formation of these high-silica rocks (~725°C), the crustal thickness (45-60 km), the occurrence of zircons with mafic characteristics, the very

pronounced negative P and Ti anomalies, as well as the estimated more than 500 km^3 of basaltic melts ponded in the base of the crust, suggesting that the magma that formed these high-silica rocks could contribute to the thickening of the arc-root where the Colombian arclogites are generated.

Table 3. 1. Sample Information from the ignimbrites and andesites

Sample	*Rock type*	*Unit*	*Lat*	*Long*	*Age (Ma)*	*εHfi*	*$^{87}Sr/^{86}Sr$*	*$^{143}Nd/^{144}Nd$*	*εNdi*	*$^{206}Pb/^{204}Pb$*	*$^{207}Pb/^{204}Pb$*	*$^{208}Pb/^{204}Pb$*	*Pb*	*Rb*	*Sr*	*Nd*	*Sm*	*Reference*
36039-SA	Ignimbrite	Guacacallo	1.868	-76.278	2.6	7.3												This study
36040-SA	Ignimbrite	Guacacallo	1.867	-76.280	2.6*		0.70455	0.512766	2.5	18.98465	15.64396	38.82128	18.9	113.6	89.0	15.1	2.6	This study
36044-SA	Ignimbrite	Guacacallo	1.885	-76.230	2.6	7.3												This study
36050-Bo	Ignimbrite	Guacacallo	2.010	-76.166	2.6	7.6	0.70453	0.512766	2.3	18.97909	15.64620	38.82178	20.0	118.2	113.0	13.4	2.1	This study
36051-Bo	Ignimbrite	Guacacallo	2.008	-76.165	2.6	7.9												This study
36053-Bo	Ignimbrite	Guacacallo	1.975	-76.124	2.6*		0.70452	0.512766	2.3	18.97553	15.64522	38.81874	17.4	108.4	219.3	16.5	2.6	This study
36057-Bo	Ignimbrite	Guacacallo	1.956	-76.022	2.6	7.8												This study
36064-Ar	Ignimbrite	Guacacallo	2.202	-76.038	2.6	7.4												This study
36071-Me	Ignimbrite	Guacacallo	2.231	-76.146	2.6	7.6												This study
36083-Po	Ignimbrite	Popayan	2.512	-76.529	2.6	7.7												This study
V04	Ignimbrite	Popayan	2.462	-76.575	2.6*		0.70449	0.512766	2.4	18.98824	15.64657	38.82991	16.9	115.6	139.2	14.3	2.3	This study
V05	Ignimbrite	Popayan	2.425	-76.626														This study
V06	Ignimbrite	Popayan	2.424	-76.628														This study
36055-Bo	Andesite	Modern arc fragment	1.951	-76.070														This study
36073-Me	Andesite	Modern arc	2.241	-76.179	0.1*		0.70432	0.512788	2.7	18.99242	15.64817	38.83376	13.2	92.4	958.8	27.4	4.8	This study
36075-Co	Andesite	Modern arc	2.319	-76.281														This study
36077-Co	Andesite	Modern arc	2.342	-76.307														This study
36079-Co	Andesite	Modern arc	2.379	-76.431														This study
36081-Po	Andesite	Modern arc	2.391	-76.491	0.1*		0.70432	0.512799	3.0	18.97100	15.64275	38.80887	14.6	74.1	768.7	29.5	5.5	This study
36072-Me	granite	Permian Arc	2.231	-76.146	272.2	1.2												This study
GLP-01B	Ignimbrite	Gigante	2.209	-75.621	<9													This study

GLP-09	Conglomerate	Gigante	2.244	-75.747	<9											This study
GLP-11	Ignimbrite	Gigante	2.231	-75.664	<9											This study
YH-04	Sandstone	Gigante	2.677	-75.408	<9											This study
YH-06	Ignimbrite	Gigante	2.674	-75.405	<9											This study
YH-07	Conglomerate	Gigante	2.674	-75.399	<9											This study
								End-member compositions								
XM3	Websterite	Mantelic Mercaderes Xenolith			<4.5	0.70300	0.513088	8.7					0.1	96.1	1.4	0.4	Rodriguez-Vargas et al., 2015
KD-WR-214	Granitoid	La Argentina Granitoic	2.645	-75.712	188.4	0.706500	0.512488	-3.0	18.84990	15.63319	38.93725	9.0	100.3	477.1	28.3	5.0	Leal-Mejía et al., 2019
Depleted Mantle		All MORB				0.70282	0.513107		18.41200	15.51500	38.10000	0.6	2.9	129.0	12.0	3.8	Gale et al., 2013
BulkDSDP69	Oceanic sediments	Pacific Sediments			<10	0.70889	0.512622		18.84760	15.61005	38.59945	5.7	16.1	1019.0	10.5	2.2	Errázuriz-Henao et al., 2019
Cajamarca Felsic	schist and granitoids	Felsic Cajamarca rocks			230	0.71754	0.512622	-0.7					114.9	173.4	25.6	5.3	Vinasco et al., 2006
HBL-B-2	Hornblendite	Mercaderes Xenoliths M			<4.5	0.70483	0.512455	-3.7	19.16200	15.68400	38.98200	0.5	2.0	65.0	13.7	4.4	Weber et al., 2002

CHAPTER 4

4. Olivine basalts and andesites trace Pleistocene lithospheric dripping under the Colombian Andes

4.1 Abstract

The magmatism in continental margins is mainly characterized by the formation of rocks with calc-alkaline signatures. However, in subduction systems, OIB-like alkaline basalts, olivine tholeiitic basalts, and andesites are sporadically found. These uncommon subduction-related geochemical signatures have been related to multiple tectonic scenarios, including the formation of a slab window, slab tearing, and slab rollback, or from the upper plate processes, such as lithospheric delamination or dripping. Monogenetic volcanoes that produced olivine basalts and andesites are cutting voluminous Pliocene siliceous ignimbrites behind the frontal arc in the central segment of the modern Colombian arc. These olivine basalts and andesites have contrasting petrographic and geochemical characteristics compared to the andesites and dacites produced by the modern arc.

New geochemical, isotopic, and geochronological data suggest that these olivine basalts and andesites correspond to ultramafic to mafic rocks with silica with SiO_2 values ranging from 39.6 to 55.2 wt.%, are enriched in Light Rare Earth Element (LREE) and have OIB-like signatures, with some samples showing weak negative Nb-Ti anomalies. These magmas were formed at high pressures and temperatures between 1150 and 1400°C from the melting of garnet±amphibole-bearing pyroxenites. Two different mafic suites can be formed: a silica-deficient amphibole-garnet-bearing pyroxenite at 2.1 Ma, producing feldspathoid normative melts (alkaline magmas), and the melting of silica-excess garnet-bearing pyroxenites at 1.7 Ma, producing hypersthene normative melts (tholeiitic magmas).

Based on the obtained data and considering regional tectonic configuration, we proposed that small lithospheric pyroxenite pieces have been dripping since 2.1 Ma, forming the restricted exposures of olivine basalts and andesites. This event followed a major phase of magmatic underplating and crustal thickening during the late Neogene.

Keywords: Pleistocene dripping; Ar-Ar geochronology; Sr-Nd isotopes; Andean orogen.

4.2 Introduction

Foundering the sub-arc roots is a typical stage in the cyclic behavior of convergent margins (DeCelles et al., 2009; Jagoutz & Schmidt, 2013). This process occurs when crustal thickening associated with tectonic shortening or magmatic underplating results in the development of a weak, crustal root that exceeds mantle density and viscosity, leading to the detachment and fall of crustal pieces into the asthenosphere (Currie et al., 2015; Ducea et al., 2021a,b; Houseman et al., 1981). A process that modifies the typical subduction-related calc-alkaline signatures in magmatic arcs (Currie et al., 2015; Ducea et al., 2013; 2021; Kay & Kay, 1993; Murray et al., 2015). Crustal foundering can occur either as an utterly delaminated piece of the lithosphere (Kay & Kay, 1993; Beall et al., 2017) or just as drips of unstable and dense arc roots (Gögüs & Pysklywec, 2008; Houseman et al., 1981). In the Central Colombian volcanic arc, anomalies in the calc-alkaline Pliocene magmatic trends developed in a previously thickened continental crust may present an ideal scenario to assess the correspondence between magmatism and upper plate processes such as delamination or dripping.

Seismological and petrological constraints from the modern magmatic arc in the central segment of the modern Colombian magmatic arc, together with the petrographic study of the mantle and lower crust xenoliths found in Mid-Pleistocene pyroclastic rocks from the same region (Bloch et al., 2017; Gianola et al., 2023; Weber et al., 2002; Zieman et al., 2023), reveal the existence of crustal thickness of ~68.5 km (Avellaneda-Jimenez & Monsalve, 2022) with a dense arc-roots (Bloch et al., 2017; Rodriguez-Vargas et al., 2005; Weber et al., 2002) that are related to arclogites roots (Gianola et al., 2023; Zieman et al.,

2023). The existence of such a thick crust has been used to discuss the occurrence of an imminent dripping of the lower crust that may have a delay due to the exceptionally high temperatures at the base of this crust (e.g., Bloch et al., 2017; Zieman et al., 2023). However, no direct evidence of crustal dripping or delamination has been presented.

Several compositional anomalies in the arc volcanic record of the central Colombian Volcanic segment have been described, including small monogenetic volcanoes composed of olivine basalts and andesites emplaced in small pull-apart basins along regional faults (Diedrix et al., 2020; Kroonenberg et al., 1982, 1987; Monsalve-Bustamante et al., 2020; Fig. 1B). Despite the fact that different tectono-magmatic scenarios have been proposed for this mafic magmatism, its petrogenesis and possible relation with the crustal delamination history have yet to be addressed.

In this contribution, we present new whole-rock geochemical, geochronological ($^{40}Ar/^{39}Ar$), and isotopic (Sr, Nd) data to understand the petrogenesis of these olivine basalts and andesites and relate them to the tectonic Plio-Pleistocene evolution of the continental margin. The geochemical and isotopic composition of these rocks allows us to recognize an OIB-like signature formed at high pressure from the melting of Silica-Excess (SE) and Silica-Deficient (SD) pyroxenites that can be related to the melting of deep arclogites. This Pleistocene vulcanism, which intruded mantle-derived highly differentiated ignimbrite deposits related to the older stage of crustal thickening by magmatic underplating (Jaramillo-Ríos et al., 2024), represents clear evidence of restricted lithospheric dripping in the Northern Andes after a major phase of magmatic underplating.

4.3 Pliocene evolution of Colombia's magmatic arc

The modern magmatic arc along the Colombian Andes is located between 0.8° and 5.2° N (**Fig. 4.1A**). It mainly includes High-Mg# (55-65) andesites and basaltic andesites, which have differentiated from mantle-derived melts with limited assimilation of continental crust and subducted sediments (Errázuriz-Henao et al., 2019; Monsalve-Bustamante, 2020). The central segment of this arc, located between 1.5 and 2.9°N (**Fig. 4.1B**), is characterized by voluminous Pliocene high-silica calc-alkaline ignimbrites (Jaramillo-Ríos et al., 2024; Kroonenberg et al., 1981; van der Wiel, 1991) intruded by the andesites of the modern arc,

as well as minor monogenetic volcanoes (**Fig. 4.1B**). The monogenetic volcanoes located behind the arc consist of well-preserved volcanic cones (**Fig. 4.2A-C**), composed of olivine-rich scoria and lapilli deposits (**Fig. 4.2D-F**), as well as basaltic and andesitic flows. These monogenetic volcanoes could be divided into three groups (**Fig. 4.1B**): Acevedo (Ac); San Agustín - Isnos (SAI); and El Morro, El Pensil, and Meremberg (MPM) (Kroonenberg et al., 1982; 1987).

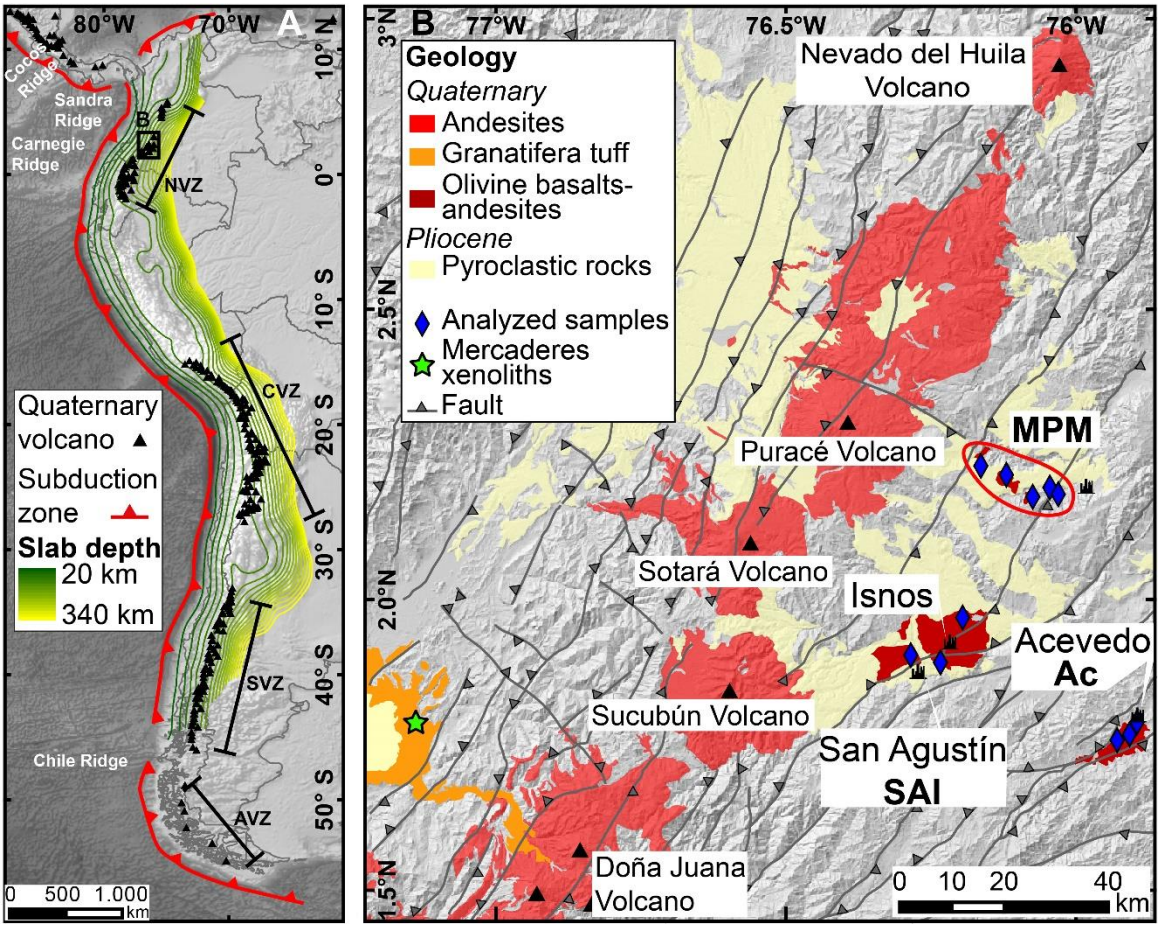

Figure 4. 1. Location map of south America and Northern Andes. **A)** South American arc, AVZ: Austral Volcanic Zone; SVZ: Southern Volcanic Zone; CVZ: Central Volcanic Zone; NVZ: Northern Volcanic Zone. **B)** Local geology of the Central segment of the modern Colombian magmatic arc.

In this arc segment, garnet-bearing pyroxenite, hornblendite, and peridotite xenoliths (**Fig. 4.1B**) dated from 5.2 to 0 Ma have been interpreted as arclogites and metasomatized mantle fragments (Bloch et al., 2017; Gianola et al., 2023; Zieman et al., 2023). The arclogites were formed at temperatures >900 °C and pressures >1.2 GPa, which represents crustal depths >50 km (Bloch et al., 2017; Gianola et al., 2023; Rodriguez-Vargas et al.,

2005; Weber et al., 2002; Zieman et al., 2023), similar to results constraint by seismological studies that have interpreted crustal thickness 68.5 km, of which ~14 km are interpreted as part of dense arc root (Avellaneda-Jiménez & Monsalve, 2022).

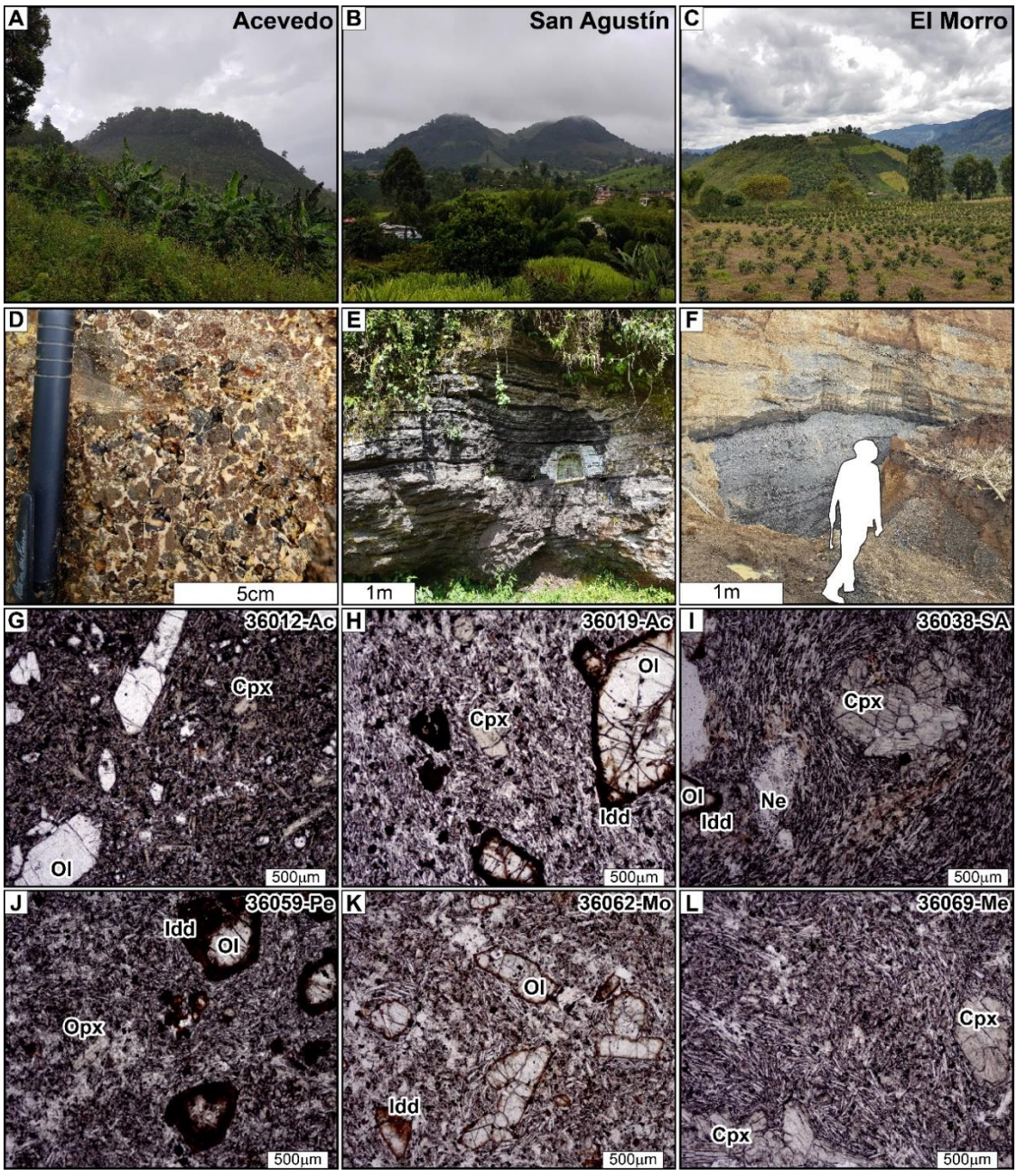

Figure 4. 2. Landscapes, outcrops, and representative microphotographs from the monogenetic olivine basalts and andesites. **A-C)** corresponds to well-preserved scoria cones from Acevedo, San Agustín, and El Morro localities, respectively**. D)** Fall deposits from Acevedo. **E)** Pyroclastic density currents from San Agustín. **F)** Fall deposits from El Morro. **G-L)** Microphotographs from different localities showing trachytic texture. See the nepheline in sample 36038-SA **(I)** and iddingsite in almost all samples. Cpx: clinopyroxene; Opx: orthopyroxene; Ol: olivine; Ne: nepheline; Idd: iddingsite.

4.4 Methods

Twenty-one samples of basaltic lava flow and bombs from scoria cones were collected at six different localities of the three different monogenetic groups (**Fig. 4.1B**). The freshest samples were selected for whole-rock geochemistry, Sr-Nd isotopic analysis, and $^{40}Ar/^{39}Ar$ geochronology. Ten samples were analyzed for whole-rock geochemistry, including three from Ac, three from SAI, and four from MPM groups at the Peter Hooper GeoAnalytical Lab at Washington State University. Eight of the samples analyzed by geochemistry were analyzed for Sr-Nd isotopes at the Radio Isotope & Geochronology Laboratory (RIGL) at Washington State University. $^{40}Ar/^{39}Ar$ ages were acquired in the groundmass of two basalts from the Ac and SAI at the Arizona Noble Gas Laboratory from the University of Arizona, following Schaen et al. (2021).

4.4.1 $^{40}Ar/^{39}Ar$ geochronology

Two $^{40}Ar/^{39}Ar$ incremental heating experiments were conducted on groundmass from the samples 36012-Ac (Acevedo) and 36030-SA (San Agustín) alkaline basalts at the Arizona Noble Gas Laboratory (ANGL) at the University of Arizona. Groundmass was isolated from the rocks by crushing and sieving from 350 and 500 μm. The purified groundmass was wrapped in aluminum foil, placed in 2.5 cm aluminum disks, and irradiated along with the 28.201 Ma Fish Canyon sanidine standard (Kuiper et al., 2008) at the Oregon State University TRIGA reactor in the Cadmium-Lined In-Core Irradiation Tube (CLICIT). Aliquots (0.5-1 mg) and single groundmass were placed in a 5 mm well within a copper planchette and incrementally heated with a Teledyne Instruments 55 W CO_2 laser.

Extracted gas was cleaned for 20-30 mins using two SAES GP50 getter at 450°C, one SAES NP10 getter at room temperature, and an Edwards Polycold® PCC Compact Cooler maintained at -90 °C before being analyzed using a Thermo Fisher Scientific Argus VI multicollector noble gas mass spectrometer. $^{40}Ar/^{39}Ar$ dates are calculated using the decay constants of Min et al. (2000), and analytical uncertainties, including J contributions, are reported at 2σ. Samples were corrected using an atmospheric $^{40}Ar/^{36}Ar$ ratio of 298.56 ± 0.31 (Lee et al., 2006). Data reduction was performed using Pychron software (Ross, 2019).

4.4.2 Whole-rock geochemistry

Ten olivine basalts (three from Acevedo, three from San Agustín-Isnos, and four from El Morro-El Pensil-Meremberg localities) were chosen, avoiding veins and weathered surfaces for whole-rock chemical analyses. The samples were crushed using a jaw crusher and powdered using a tungsten carbide ball mill at Zirchron LLC. Major and trace elements were analyzed using a Rigaku 3370 X-ray fluorescence (XRF) spectrometer at Washington State University. Details of sample preparation, dilution, and analytical procedures have been described by Johnson et al. (1999).

Trace elements, including Rare Earth Elements (REEs), were determined by ICP-MS (Agilent 7700) at Washington State University. A 2g aliquot was weighed into a graphite crucible and mixed with 2 g of $LiBO_2$ flux. The crucibles were placed in an oven and fused at 1000°C in a muffle furnace for 30 min. The resultant bead was ground in a steel ring mill, and a 0.25 mg portion was dissolved using HNO_3 (2 mL), HF (6 mL), and $HClO_4$ (2 mL) at 110 °C. Calibration standards and reagent blanks were added to the sample sequence. Sample solutions were aspirated into an ICP emission spectrograph (Jarrel Ash Atom Comb 975) to determine major oxides and certain trace elements (Ba, Nb, Ni, Sr, Sc, Y, and Zr).

The crystallization temperatures of these basalts-andesites were calculated with the concentration of Mg of each sample following the formula $T(\pm 5°C, 1\sigma) = 27.35(\pm 0.65) * (MgO^{liq}) + 984(\pm 4)$ (Salazar-Naranjo & Farias-Vlach, 2023). This new experimental method was developed for alkali ultrabasic to intermediate magmas, concordant with those found in this study.

4.4.3 Whole-rock isotopes

Whole-rock Sr and Nd isotope composition of eight olivine basalts were acquired at the RIGL using the Thermo-Finnigan Neptune+ multi-collector system. After crushing the samples, they were powdered using an agate mill jar and balls at Zirchron LLC. The procedures for Sr and Nd isotope preparation are the same as those in Gaschnig et al. (2011). The Sr analyses were corrected for mass fractionation using $^{86}Sr/^{88}Sr = 0.1194$ and normalized using the NBS-987 standard. The average reproducibility, with two standard deviations of $^{87}Sr/^{86}Sr$, was ± 0.00005. The initial isotopic values were calculated using Rb and Sr concentrations from the XRF. The Sm and Nd isotope analyses followed the

procedures described in Vervoort and Blichert-Toft (1999). Sm and Nd mass fractionation were corrected using $^{147}Sm/^{152}Sm = 0.56081$ and $^{146}Nd/^{144}Nd = 0.7219$, respectively, and normalized using the Ames Nd standard (±0.000020 2σ average reproducibility). The εNd values were calculated using present-day values of $^{143}Nd/^{144}Nd = 0.512630$ and $^{147}Sm/^{144}Nd = 0.1960$ for CHUR (Bouvier et al., 2008).

4.5 Petrography, geochronology, geochemistry, and isotopic results

Basaltic lava flows and bombs from scoria cones were collected at six different localities of the three different monogenetic groups (**Fig. 4.1B**). Groundmass contents of the lavas vary between 70 and 95 vol.%, and olivine, clinopyroxene, and orthopyroxene phenocrysts content is between 30 and 5% (**Fig. 4.2G-L**). Some crystals of olivine and pyroxene are replaced by iddingsite (**Fig. 4.2H-K**). The main texture is trachyte and pilotaxitic (**Fig. 4.2E-L**), and the samples are petrographically classified as basalts and andesites.

Whole rock $^{40}Ar/^{39}Ar$ results yield overlapping isochronal ages of 2.01 ± 0.26 for sample 36012-Ac from Acevedo basalt and 1.71 ± 0.36 Ma for sample 36026-SA from a San Agustín basalt (**Fig. 4.3**). These ages are younger than the age of 2.6 Ma from the ignimbrite host rocks from the Guacacallo Formation (Jaramillo-Ríos et al., 2024; Sanín et al., 2022) and are younger than the $^{40}K/^{40}Ar$ age of 31.2 ± 2.7 Ma from the Acevedo basalts (Kroonenberg et al., 1982).

Analyzed samples have MgO ranging from 8.0 to 14.9 wt.% (**Fig. 4.4A**), Na_2O and K_2O ranging from 2.3 to 3.9 and 0.4 to 1.7 wt.% (**Fig. 4.4A, B).** These rocks have Al_2O_3 and CaO ranging from 10.1 to 16.9 and 6.3 to 16.3 wt.% (**Fig. 4.4C, D**). The FeO total and TiO_2 range from 7.1 to 11.3 and 1.1 to 2.5 wt.% (**Fig. 4.4E, F**). The Ni and Cr ranged from 65.2 to 432.4 and 166.4 to 751.3 ppm (**Fig. 4.4G, H**). The SiO_2 and total alkalis (Na_2O+K_2O) range from 39.6 to 55.2 and 2.9 to 5.2 wt.% (**Fig. 4.4A**), respectively. These rocks correspond to basanites, picrobasalts, basalts, and basaltic andesites varying from sub-alkaline to alkaline series (**Fig. 4.4I**).

However, following the immobile elements, these rocks are classified as alkali basalts, except for one sample classified as basalt (**Fig. 4.5A**). These basalts present CaO/Al_2O_3 values from 0.5 to 1.5 (**Fig. 4.5C**). The Mg# varies from 60.6 to 72 (**Fig. 4.5D**). The temperatures from these basalts range from 1156 to 1430 °C (**Fig. 4.5B, C**).

These results show that these rocks are remarkably primitive, silica-undersaturated, with the presence of nepheline, and were produced by low degrees of partial melting of an extreme mafic source.

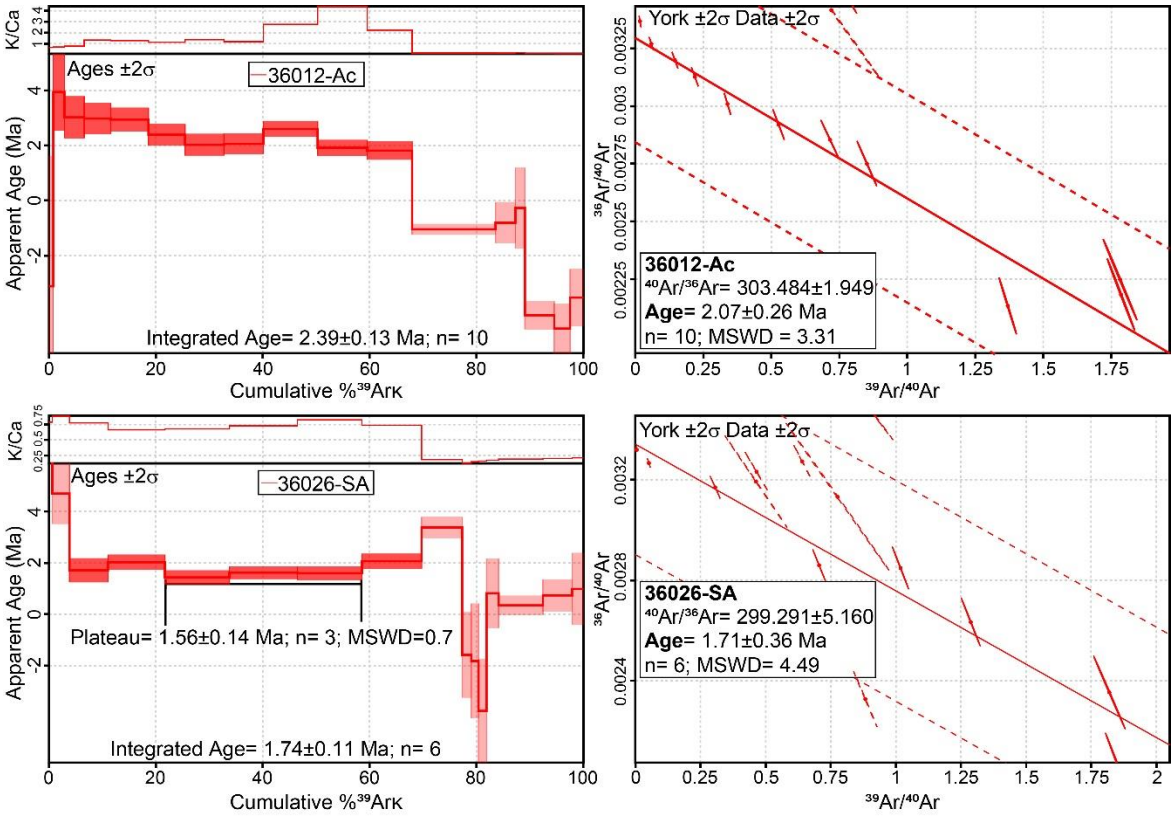

Figure 4. 3. $^{40}Ar/^{39}Ar$ geochronology on groundmass extracted from two olivine basalts. Sample 36012-Ac corresponds to the Acevedo basalts, while sample 36036-SA corresponds to San Agustín basalts. The left side shows the incremental heating experiments on each sample, whereas the right side corresponds to the isochrones of each sample.

All the basalts from Ac and two from SAI are enriched in light rare earth elements (LREE) and have a pronounced depletion in the heavy rare earth elements (HREE) compared with basalts-andesites from MPM and one from SAI. Almost all samples (except sample 36069-Me) have OIB-like signatures (**Fig. 4.5E**).

Ac basalts are also characterized by their negative K anomaly and flat Nb and P patterns that contrast with the weak-negative Nb and positive Pb anomalies in the SAI and

MPM (**Fig. 4.5F**). εNd_i varies between 0.6 and 4.1, whereas $^{87}Sr/^{86}Sr_i$ extend between 0.70413 and 0.70436 (**Fig. 4.6A**).

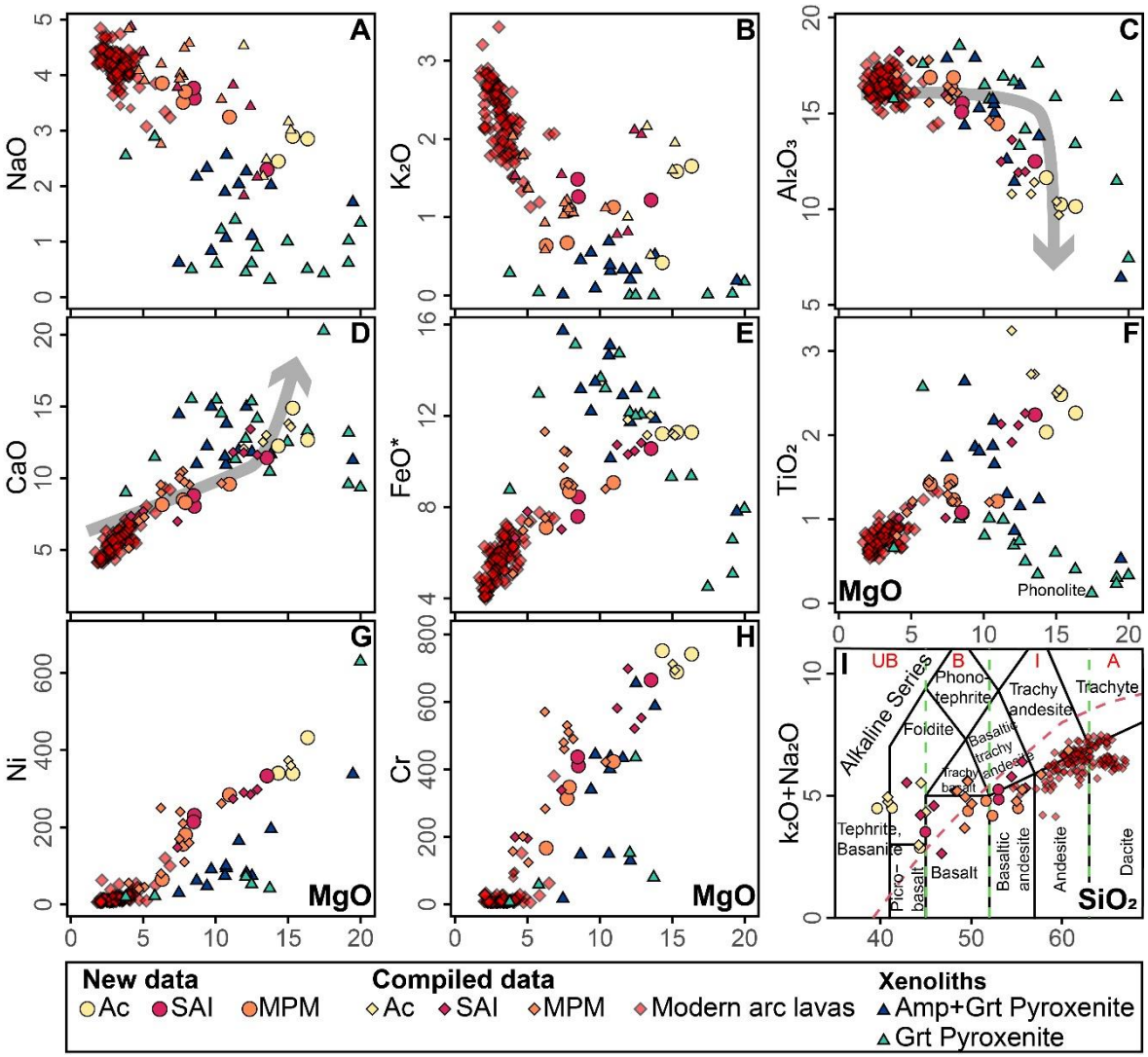

Figure 4. 4. Harker-type and classification diagrams. A-H) Harker-type diagrams of MgO vs major elements and traces. I) TAS diagram (Le Bas et al., 1986). Gray arrows in C-D indicate the compositions of melting increasing pressure since an olivine-free source (Kogiso et al., 2004). Compiled data of alkaline basalts is from Kroonenberg et al. (1987), Rodriguez & González. (2004), and Rodriguez & Sánchez. (2017). Compiled data from the recent volcanic arc is from Correa-Tamayo et al. (2020), Droux & Delaloye. (1996), Jaramillo-Ríos et al. (2024), Marín-Cerón et al. (2010).

4.6 Discussion

Silica-undersaturated rocks with OIB-like signatures and nepheline-olivine normative minerals, as well as hypersthene normative minerals, are not expected in a typical

subduction-relate regime, where the fusion of the asthenospheric wedge in the presence of water gives the typical click-alkaline signature (Gómez-Tuena et al., 2014; Grove et al., 2009; 2012).

The isotope εNd_i and $^{87}Sr/^{86}Sr_i$ signatures of this basaltic-andesitic magmatism are similar to the andesites from the modern arc and some garnet-bearing pyroxenites and hornblendites (arclogites) found in Mercaderes xenoliths (Bucheli et al., 2024; Jaramillo-Ríos et al., 2024; Marín-Cerón et al., 2010; Monsalve-Bustamante, 2020; Rodriguez-Vargas et al., 2005; Weber et al., 2002; **Fig. 4.6A**), suggesting a genetic link between them.

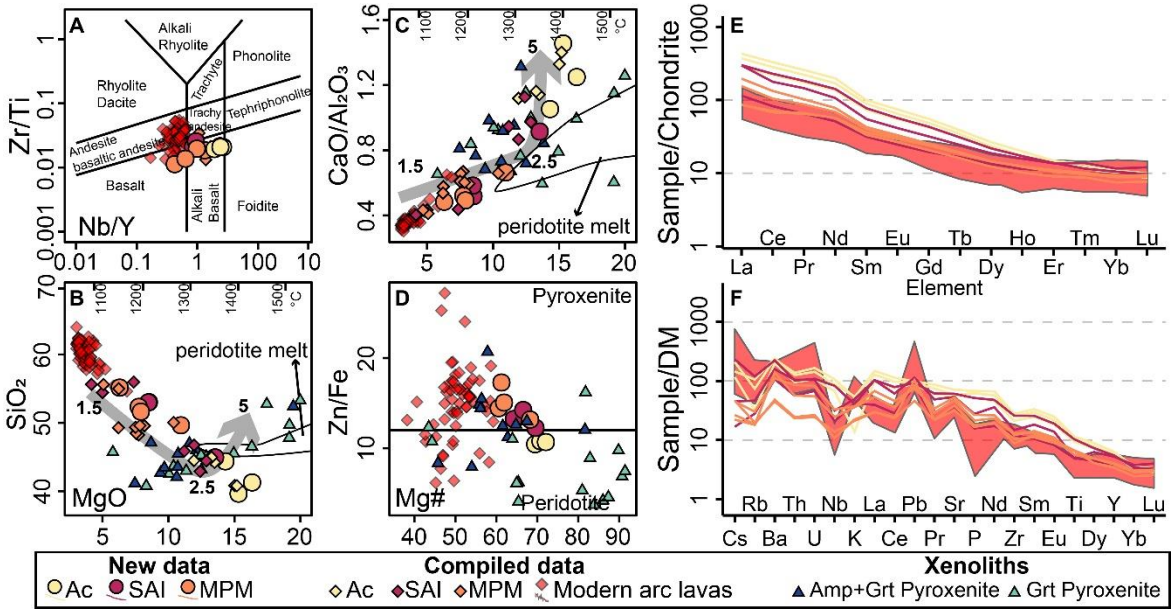

Figure 4. 5. Classification, Harker-type, and multielement diagrams. **A)** Classification diagram (Pearce, 1996), **B-D)** Harker-type diagrams of MgO vs. **B)** SiO_2. **C)** CaO/Al_2O_3 with the respective temperatures and **D)** Mg# vs. Zn/Fe, **E)** Spider diagram normalized to Chondrite. **F)** Spider diagram normalized to Depleted Mantle (McDonough & Sun, 1995). Samples correspond to olivine basalts from the same locations. Gray arrows in B-C indicate the compositions of melting increasing pressure since an olivine-free source (Kogiso et al., 2004).

This olivine volcanism has been commonly related to rear magmatism (Monsalve-Bustamante et al., 2020) or slab windows associated with the subduction of the Carnegie Ridge (Kroonenberg et al., 1982; 1987; Rodríguez & González, 2004). The absence of well-defined subducted-related signatures, including Nb or Ti anomalies or enrichment in Th (**Fig. 4.5F**), together with their proximity to the modern arc front and the bimodal silica-undersaturated and silica-saturated rocks, ruled out the possibility of these rocks forming due to melting by late dehydration of the subducted slab in a rear arc position (Garrison et al., 2018; Hildreth et al., 2004).

On the other hand, the spatial distribution of magmatism during slab window formation commonly follows the geometry of a subducted ridge and includes magmatic activity in the fore-arc (Thorkelson et al., 2011). In this segment of the Northern Andes, there is no evidence of magmatism following the possible geometry of the Carnegie Ridge (**Fig. 4.1A, B**). Also, geophysical and structural evidence does not support slab tearing (Rosenbaum et al., 2019), as the Nazca slab in this segment of the Colombian Andes is subducting without lateral interruptions (Hayes et al., 2018; Rodriguez et al., 2024).

When the three monogenetic groups are compared, the Ac and (5) samples from SAI present lower SiO_2 (<45 wt.%) and higher MgO (13 -16 wt.%), and CaO/Al_2O_3 (0.9 - 1.5) values (**Fig. 4.5B-D**), as well as higher enrichments in LREE (**Fig. 4.5E**), nepheline-olivine normative minerals, that also yield crystallization temperatures between 1280 and 1430°C (**Fig. 4.5B-C**), these geochemical signatures can relate to the melting of a garnet-rich pyroxenite (Schiano et al., 2000) or a CO_2-rich mantle peridotite (Dasgupta et al., 2007). Usually, CO2-rich peridotites produce basalts with high CaO (>16 wt.%) contents (Dasgupta et al., 2007; Schiano et al., 2000), which is not the case with the samples presented in this study. Thus, the melting of garnet-amphibole-rich pyroxenites or hornblendites, where the amphibole is an early exhausted mineral phase, could generate depleted SiO_2 and CaO-Al_2O_3-rich melts (Medard et al., 2006; Schiano et al., 2000).

On the other hand, intermediate rocks with SiO_2 >49 wt.%, lower MgO and CaO/Al_2O_3 values, and crystallization temperatures between 1153 and 1215°C (**Fig. 4.5B-D**), as well as hypersthene-normative found in the basalts-andesites from the MPM and the SAI, could typically be formed from melting an SE source (Kogiso et al., 2004).

The Zn/Fe ratio is particularly sensitive to the melting of Cpx-Grt-rich (pyroxenite) or Ol-Opx-rich (peridotite) lithologies (Bowman & Ducea, 2023; Le Roux et al., 2010). At least all the studied basalts and andesites show Zn/Fe ranges from 10.4 to 17.3 (**Fig. 4.5D**). Commonly, Zn/Fe ratios >12 are related to the melting of a garnet-bearing pyroxenite (Bowman & Ducea, 2023). Samples from Ac that present with a Zn/Fe ratio <12 could be related to the melt of a peridotite. However, melting pyroxenites with a high quantity of amphibole, as in the case of the Mercaderes arclogites (Weber et al., 2002), could have reduced the Zn/Fe fractionation.

The pseudo-ternary diagram of Fo–CaTs-Qz projected from diopside (**Fig. 4.6B**) is crucial to diagnosing the sources that produced basaltic magmas under high-pressure conditions (O'Hara, 1968). It is possible to observe how almost all the studied basaltic samples plot towards the left side of the division line between calcium Tschermak's pyroxene (CaTs) and Enstatite (En) (**Fig. 4.6B**). The left side of this diagram is related to the melting forming from SD sources at high pressures (Bowman & Ducea, 2023; Kogiso et al., 2004). On the other hand, some samples from MPM and SAI fell on the right side of this diagram, which suggests the melts formed from SE sources also at high pressures (Hirschmann et al., 2003; Lambart et al., 2013).

The crystallization temperatures of these mafic rocks with values between 1156 and 1431 °C (**Fig. 4.5B-C**) are similar to those from the arclogites xenoliths from the central segment of the Colombian magmatic arc that show temperatures ranging from 910 to 1400°C (Bloch et al., 2017; Gianola et al., 2023; Weber et al., 2002; Zieman et al., 2023). Therefore, we suggest that hot asthenospheric upwelling facilitated the high-temperature melting of a thick arclogite root, such as those recovered in the xenoliths.

Table 4. 1. Analyzed sample from the olivine basalts and andesites.

Sample	Rock Type	Unit	Age (Ma)	Lat	Long	$^{87}Sr/^{86}Sr$	$^{143}Nd/^{144}Nd$	εNd	SiO2
36011-Ac	Olivine Basalt	Acevedo Basalts		1.792	-75.894				43.01
36012-Ac	Picrite	Acevedo Basalts	2.1±0.3	1.771	-75.906	0.70435	0.51284	4.0	38.50
36017-Ac	Olivine Basalt	Acevedo Basalts		1.760	-75.927	0.70424	0.51284	4.0	40.67
36026-SA	Olivine Basalt	San Agustín-Isnos Basalts	1.7±0.4	1.902	-76.281	0.70436	0.51280	3.2	51.85
36045-Is	Olivine Basalt	San Agustín-Isnos Basalts		1.890	-76.236	0.70425	0.51280	3.2	52.57
36049-Is	Olivine Basalt	San Agustín-Isnos Basalts		1.972	-76.194	0.70429	0.51285	4.1	43.91
36059-Pe	Olivine Basalt	El Pensil Basalts		2.178	-76.072				51.59
36060-Mo	Olivine Basalt	El Morro Basalts		2.186	-76.036	0.70413	0.51283	3.7	49.15
36062-Mo	Olivine Basalt	El Morro Basalts		2.183	-76.031	0.70423	0.51279	3.0	50.69
36069-Me	Olivine Basalt	Meremberg Basalts		2.216	-76.120	0.70436	0.51267	0.6	54.47

Seismological and petrological constraints from crustal and mantle xenoliths suggest that magmas for the central segment of the Colombian magmatic arc must have evolved within crustal thicknesses of ~64 km (Avellaneda-Jimenez & Monsalve, 2022; Bloch et al., 2017; Gianola et al., 2023; Zieman et al., 2023). The petrologic studies of these arclogites show that these rocks are denser than the underlying mantle (Zieman et al., 2023) and are

susceptible to foundering into the asthenosphere due to the highly negative buoyancy (Lee, 2014). Nevertheless, the olivine basalts and andesites produced in the monogenetic volcanic fields in the central segment of the Colombian magmatic arc are associated with the foundering or dripping of small lithosphere pieces in this arc section.

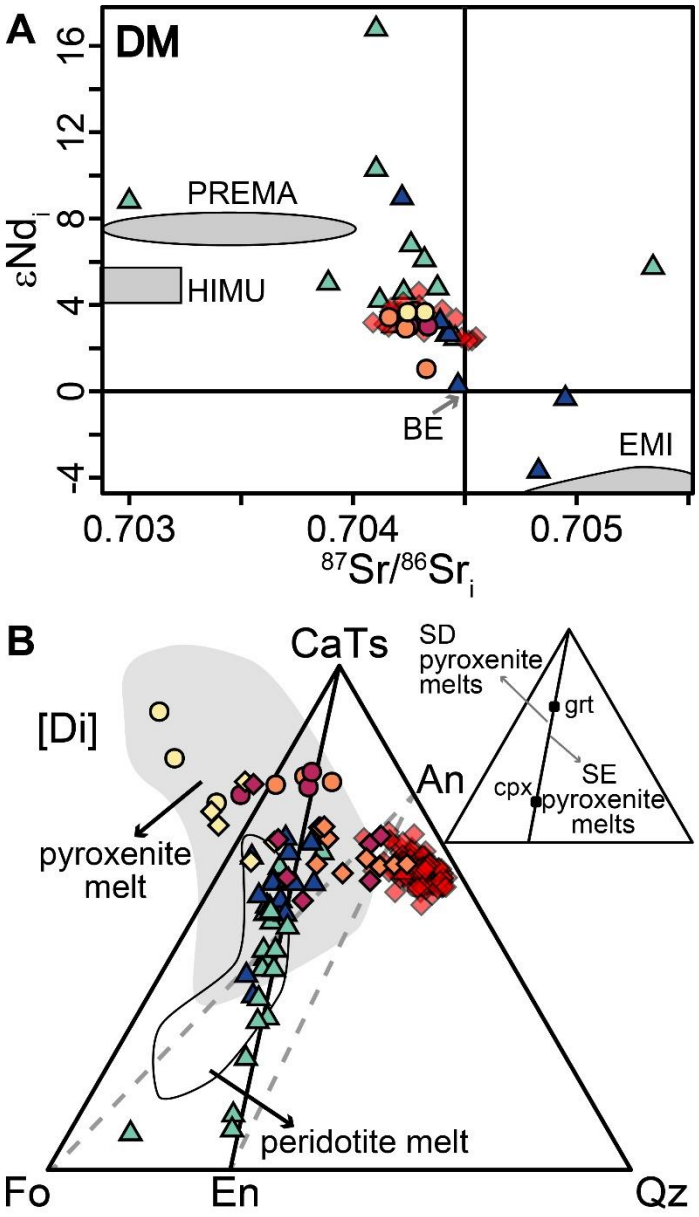

Figure 4. 6. Isotopic and pseudo-ternary diagram projected from [Di]. **A)** $^{87}Sr/^{86}Sr_i$ vs. εNd_i plot showing the samples and the different mantle reservoirs. **B)** Forsterite (Fo)–calcium Tschermak's pyroxene (CaTs)–quartz (Qz) pseudo-ternary diagram projected from [Di] following the method of O'Hara, (1968). The dashed line between enstatite (En) and anorthite (An) corresponds to the separation between undersaturated and oversaturated magmas. Compositions of minerals are also shown in the inset: grt: garnet; cpx: clinopyroxene. DM: depleted mantle; PREMA: prevalent mantle; HIMU: high-u(U/Pb), BE: bulk silicate earth; and EM1: enriched mantle. Symbols are as in **Fig. 4.5**.

The limited distribution of this mafic alkaline magmatism, their intrusive relation with older ignimbrites associated with a significant Pliocene crustal thickening by magmatic addition (**Fig. 4.7A**; Jaramillo et al., 2024), and their association with small pull-apart basins (Diedrix et al., 2020) claim for small and localized lithospheric pieces foundering into the asthenosphere, as is expected in a dripping event (**Fig. 4.7B**), as it also suggests for the local preservation of crustal thickness of ~ 68 km in this arc segment (Avellaneda-Jiménez & Monsalve, 2022).

Although Zieman et al. (2023) have suggested that the existence of ~10% of partial melts entrapped into the arclogites prevents the arc root from falling into the mantle and causing a delamination event, we suggest that the intense strike-slip tectonics experienced by the Northern Andes at least since the Eocene (e.g., Montes et al., 2019; Zapata et al., 2023), the more limited shortening in the Central Cordillera dominated by a metamorphic and igneous basement, and the non-stationary character of this arc that precludes longer-term magmatic addition within the same crustal domain (Echeverri et al., 2015; Wagner et al., 2017; **Fig. 4.7A**), also limits the entire delamination of the lower crust.

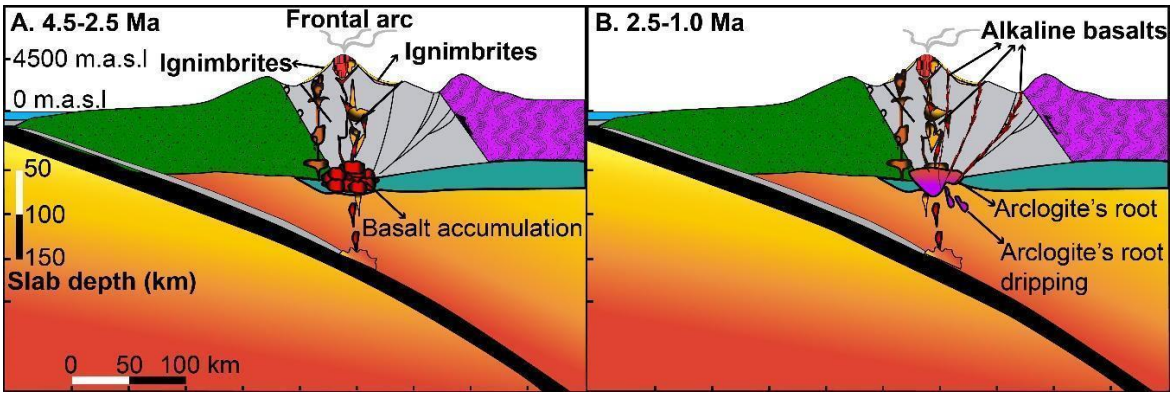

Figure 4. 7. Schematic model of the Colombian magmatic arc evolution from Upper Miocene to recent. **A)** Voluminous production of high-silica volcanic rocks, with a generation of voluminous cumulates. **B)** Lithospheric dripping of the basaltic cumulates, which became arclogites.

4.7 Conclusions

Based on the data presented in this study, low-volume OIB-type mafic volcanic rocks, varying between picrites, basanites, basalts, and andesites, are outcropping behind the frontal arc in the central segment of the modern Colombian magmatic arc.

Petrological constraints suggest that two types of pyroxenites were dripped and melted to form these kinds of magmas: an SD amphibole-garnet-bearing pyroxenite dripped at 2.1

Ma, gave rise to silica-undersaturated magmas, which are olivine-nepheline-normative, have the higher concentrations of CaO/Al_2O_3, and MgO, as well as high Mg#. In contrast, a SE garnet-bearing pyroxenite dripped at 1.6 Ma gave rise to silica-saturated magmas that are hypersthene-normative and have an andesitic signature.

These rocks are a direct record of small pieces of arc-root dripping during the Pleistocene after forming a denser and unstable lower crust in an intense phase of Pliocene magmatic underplating.

Density factors and the particular crustal architecture of the Colombian Arc limit the existence of a broader-scale delamination event.

CHAPTER 5

5. General Discussion and Concluding Remarks

5.1 Crustal evolution in an accretionary margin

The Colombian margin has broadly been recognized as a collisional orogen. At least two collisions of Caribbean-derived blocks in this margin occurred during the Upper Mesozoic and the Cenozoic (Kennan & Pindell, 2009; Montes et al., 2019; Restrepo & Toussaint, 1988). The collision of the Caribbean Plateau with the continental margin at ~72 Ma (Jaramillo et al., 2017; Villagómez & Spikings, 2013; Zapata-Villada et al., 2021) produced a rapid uplift and exhumation in the continental crust (Zapata et al., 2021). These high rates are evidenced in the thermochronological data and basin evolution (Pardo-Trujillo et al., 2020; Bayona et al., 2012).

Due to the sensitivity of magmatism to changes in tectonic settings and the evolution of continental crust, the PECMA is critical for the understanding of crustal evolution after the Caribbean Plateau collisional event (Bayona et al., 2012; Bustamante et al., 2017; Cardona et al., 2018; Duque-Trujillo et al., 2019a; Leal-Mejía et al., 2019; León et al., 2022). This magmatism, dated between 62 and 50 Ma in plutonic rocks, is characterized by adakite-like signatures and bi-modal isotopic behavior (Bustamante et al., 2017; Cardona et al., 2018; Leal-Mejía et al., 2019), as well as, for the lack of proximal volcanic rocks and the small volume of the plutonic rocks **(Fig. 1.1B; 2.1**). It has also been related to contrasting tectonic settings, such as slab break-off of the subducted Caribbean Plate at ~ 58 Ma (Leal-Mejía et al., 2019) and to high-pressure magmatic evolution controlled by a thick continental crust (Bustamante et al., 2017; Cardona et al., 2018; León et al., 2022).

Due to the scarce exposure of the PECMA, the detrital proxy was used to evaluate the period of magmatic activity and its evolution (Chapter 2). The Bogotá Formation, a Paleocene-Eocene sedimentary formation outcropping in the Eastern Cordillera of the Colombian Andes, has been broadly studied due to its paleontological interest in the chemical characterization of the Paleocene-Eocene Thermal Optimum (Jaramillo &

Cardenas, 2013; Morón et al., 2013). In this study, the new LA-ICP-MS and CA-ID-TIMS geochronology shows that the arc restarted at ~66 Ma, at least 4 Ma earlier than previously published (Duque-Trujillo et al., 2019b). The discrepancy in the restart time could be related to the bias due to the erosion of the volcanic and plutonic rocks from the PECMA and, therefore, the lack of outcrops older than 62 Ma. The mean values of the detrital record in the Bogotá Formation yield an age of ~59.4 Ma. In contrast, the mean age of the plutonic rocks is ~55.7 Ma, reinforcing the hypothesis that the continental crust suffered high weathering and erosion, producing a bias in the whole-rock analysis derived from the plutonic record. The geochronological data shows that 66 - 62 Ma ages are restricted to the lower layers of the Bogotá Formation, whereas the 62 - 55 Ma increased in the upper layers, which could be related to a systematic unroofing (**Fig. 2.4**).

The statistical evaluation of these detrital zircons suggests that the magmatic record between 66 and 62 Ma could be grouped into different age groups concerning those between 62 and 50 Ma (**Fig. 2.3A, C**). The chemical results presented in this manuscript show that zircons between 66 and 62 Ma were generated under a thick crust, with Hf contents related to differentiated rocks (**Fig. 2.6E**), and εHf values suggest significant crustal assimilation (**Fig. 2.7F**). These data are consistent with the thick continental crust following the Caribbean Plateau collision, as León et al. proposed (2021).

The behavior of the arc between 62 and 55 Ma is bimodal. It is possible to observe Hf concentrations ca 15,000 ppm corresponding to highly differentiated magmas for one group and <11,000 ppm corresponding to intermediate magmas for another group (**Fig. 2.6E**). The same changes are observed in the Th/U and U concentrations (**Fig. 2.6C**). A weak bimodal Yb/Gd is also observed (**Fig. 2.7C**), according to the crustal thickness estimations (**Fig. 2.8A, B**). Bimodal isotopic signatures also characterized the whole-rock and zircon analyses (**Fig. 2.7E, F**). The crustal thickness estimates suggest that between 62 and 55 Ma, the magmatic arc was developed into two different crustal thicknesses. Lower temperatures accompanied the thinned crust of ~40 km, whereas the thicker crust of ~70 km was accompanied by higher temperatures (**Fig. 2.8A-C**). The CA-ID-TIMS geochronology and chemistry endorse these differences in the crustal thickness and chemical behavior.

Although the whole-rock analysis is mainly developed in rocks aged between 55 and 50 Ma, it is possible to observe a clear relation between whole-rock geochemistry and isotopic

data and with the zircon chemistry and isotopic data. This bimodal magmatism includes magmatic rocks formed from mantle sources with different quantities of crust assimilation, where those magmas formed in a thick crust usually suffer more substantial crustal contamination than those developed in a thinner crust. This continental magmatism finishes at ~ 48 Ma due to the high obliquity of the continental margin and the beginning of the block drifting to the north (Bayona et al., 2012; Montes et al., 2019).

5.2 Pliocene to Modern crustal and magmatic evolution of the central segment from the modern Colombian magmatic arc

The formation of high-silica magmas in a magmatic arc dominated by andesites and basaltic andesites (Correa-Tamayo et al., 2020; Marín-Cerón et al., 2010; Monsalve-Bustamante, 2022) could be related to magmas being differentiated in the thicker continental crust where the residence time of magma is more significant than in thinner crust and, therefore, could suffer more differentiation (Annen et al., 2006; Ducea et al., 2015a; Lee & Anderson, 2015; Paterson & Ducea, 2015). Alternatively, the melting of the continental crust could form silica-rich magmatic rocks (Caffe et al., 2012; Foley et al., 2023).

The geochemical and isotopic signatures suggest that the continental crust quickly thickened between 50 and 60 km during the high-silica magma formation and shows an important mantle input in the formation of basalt that was subsequently differentiated (Jaramillo-Ríos et al., 2024). The differentiation could occur in a MASH zone (Hildreth & Moorbath, 1988). Still, cumulates were probably ponded in the lower crust, as has been observed by the arclogites in this arc segment (Gianola et al., 2023). More than 500 km^3 of mafic cumulated could be ponded in the lower crust, and more material could be accumulated in the middle and upper crust (**Fig. 3.13C**), promoting the crustal thickness and the formation of arclogites.

The alkaline basalts that outcropped close to the modern arc lavas and intruded the ignimbrites yielded ages between 2.1 Ma for the easternmost and 1.7 Ma for the ones that intruded the ignimbrites. The geochemical and isotopic compositions are peculiar and suggest melting a garnet-bearing pyroxenitic source. The isotopic data is similar to some

garnet-bearing pyroxenites from the Mercaderes xenoliths (Rodriguez-Vargas et al., 2005; Weber et al., 2002). The geochemical data suggest two different sources to form these basalts: silica-excess (SE) and silica-deficient (SD).

The SD source promoted the formation of depleted SiO_2 and LREE and enriched CaO magmas (**Fig. 4.5; 4.6**). These characteristics are typical of the melting of amphibole-garnet bearing pyroxenites, where the melting at high pressures of the amphibole produces the depletion in silica (Lambart et al., 2012; 2013; Sorbader et al., 2013) and the melting of the pyroxene could enrich the CaO content (Kogiso et al., 2003; Medard et al., 2006) generating feldspathoidal normative minerals. The SE source at high pressures generates hypersthene normative magmas. Nepheline normative magmas formed in both the easternmost and the closer-to-arc alkaline location, whereas hypersthene normative magmas were only recorded in the alkaline location.

5.3 The continental crust dynamics during the Cenozoic in the Northern Andes

From the chapters developed in this thesis, it is evident that magmatism was chemically sensible to the changes in the continental crust during the Cenozoic. It shows how the continental crust has suffered different episodes of thickening and thinning after the collisions of Caribbean blocks.

In addition to magmatism, sedimentological and stratigraphic studies have been recently published, suggesting changes in the dynamic of the continental crust during the Eocene-Miocene for the Magdalena Valley (Zapata et al., 2023a). On the other hand, volcano-sedimentary and thermochronological studies have been developed using rock from the Cauca Canyon, showing crustal thickness and movement changes over time (Bernet et al., 2020; MacDonald et al., 1996; Perez-Consuegra et al., 2021; Piedrahita et al., 2017; Zapata et al., 2023b).

In summary, the continental crust after the collision of the Caribbean Plate at ~72 Ma was thicker than the Cretaceous (Bustamante et al., 2017; Cardona et al., 2018; León et al., 2021), involving high exhumations and uplift rates (Zapata et al., 2021). Due to the oblique displacement of the Caribbean Plate that migrates from the Pacific to the Atlantic position

(Kennan & Pindell, 2009; Pindell & Kennan, 2009), strike-slip tectonics was developed in the continental crust during the Paleocene-Eocene. These tectonics favored the contemporaneous formation of thick continental crust, promoting the dripping of the thicker crust (Jaramillo et al., 2022), as is observed in New Zealand (Stern et al., 2013). Recent 2D numerical models show that at least to the Sierra Nevada de Santa Marta, a lithospheric removal that occurred between 56 and 40 Ma could be a feasible model to explain the high topography and localized positive Bouguer anomaly present in this zone (Quiroga et al., 2014).

During the Eocene- Miocene, the strike-slip controlled the basin filling and the continental crust exhumation. The Collision of the Panama-Chocó at ~ 20 Ma was held by oblique convergence (Montes et al., 2012; 2015), and the Timbiquí arc was juxtaposed in southwestern Colombia (Cardona et al., 2018).

Due to the strike-slip tectonics in the continental crust, it was possible to preserve rivers draining from the west to the east and filling basins in the Magdalena Valley (Montes et al., 2021; Zapata et al., 2023a). During this time, the continental magmatism restarted at ~ 25 Ma in southwestern Colombia (Echeverri et al., 2015; Leal-Mejía et al., 2019) and continuously migrated up to reach the recent position (Echeverri et al., 2015; Wagner et al., 2017). This magmatism migration contributed to the passage closing, which allowed for the western-eastern drainages. The closure of these passages is also evidenced in the sedimentological and thermochronological data (Montes et al., 2021; Zapata et al., 2023).

From the Upper Miocene to the present, magmatism, at least in the modern arc's central segment, has probably been developed *in situ.* In the Upper Miocene, between 9 and 6 Ma, magmatism is only recorded by volcaniclastic rocks from the Gigante Formation (Anderson et al., 2016; Jaramillo et al., 2020; van der Wield, 1990). A pause in the magmatism of ~ 3 Ma is recorded in this section of the arc, just until the magmatic flare-up that gave rise to the Popayan and Guacacallo formations (Jaramillo-Ríos et al., 2023; 2024). Producing these voluminous volcanic rocks suggests a significant quantity of material stacked in the lower, middle, and upper crust (Chapter 3).

The recent and rapid structuration of the Central Cordillera of Colombia, suggested by the magmatic evolutionary patterns, has also been proposed from a botanical approach. Ceroxylon is a genus of palms endemic to the Tropical Andean region that is dispersed only

over 1400 m.a.s.l (Sanín & Galeano, 2011). Genetic studies of the palms have shown that the dispersal of highland Ceroxylon palms in the Northern Andes coincided with the formation at 2.6 Ma of highly voluminous SiO_2-rich ignimbrites in the central segment of the modern Colombian magmatic arc (Sanin et al., 2022). It is proposed that the high topography needed for the dispersal of these palms was promoted by crustal uplift through magmatic inflation and valley filling by pyroclastic currents (Sanin et al., 2022).

5.4 Concluding remarks

This study shows how magmatism has been sensible to the dynamics of the Northern Andean continental crust. Using different chemical and isotopic tools made it possible to reinforce the hypothesis that strike-slip tectonics played a critical role in constructing the continental crust and how the lithospheric dripping has been present in the crustal evolution and topography changes.

This study suggests at least two episodes of lithospheric dripping. The first occurred in the Eocene and was triggered by the crust dynamics after the collision of the Caribbean Plateau. The second dripping happened during the Pliocene and was triggered by the voluminous mafic magmatic addition, resulting in flare-up episodes.

In this contribution, I show how using the detrital zircons improved the interpretation of the magmatic evolution, especially in countries such as Colombia, where the high weathering and erosion rates destroy and completely disappear the in situ proximal and primary rocks. In this study, using the high-precision zircon CA-ID-TIMS geochronology and chemistry was fundamental to splitting different magmatic trends occurring into short periods.

Using the whole-rock analysis and the zircon petrochronology was fundamental to understanding the building of the central segment of the modern magmatic arc. The magmatic flare-up recorded in the voluminous SiO_2-rich volcanic rocks suggests that a high volume of magma is ponded in the lower and upper crust, contributing to a rapid crustal thickening.

Restricted olivine basalts and andesites, some with OIB-like alkaline geochemical signatures, suggest melting SD and SE garnet-baring pyroxenites. As is evidenced by the

Mercaderes xenoliths, those pyroxenites are common in the Northern Andean magmatic arc, and both garnet-bearing pyroxenites and hornblendites are found.

Despite that, a thick continental crust is evident in the central segment of the modern magmatic arc; the chemical, geochronological, and isotopic data of the OIB-like alkaline basalts suggest that small pieces of the lower crust have dripped in the Pliocene at this section of the arc.

Bibliography

Acosta, J. E., & Ulloa, C. E. (1998). Geología de la Plancha 246 Fusagasugá.

Alberts, D., Gehrels, G. E., & Nelson, J. (2021). U-Pb and Hf Analyses of Detrital Zircons from Paleozoic and Cretaceous Strata on Vancouver Island, British Columbia: Constraints on the Paleozoic Tectonic Evolution of Southern Wrangellia. Lithosphere, 2021(1), 1-20. https://doi.org/10.2113/2021/7866944

Alonso-Perez, R., Müntener, O., & Ulmer, P. (2009). Igneous garnet and amphibole fractionation in the roots of island arcs: experimental constraints on andesitic liquids. Contributions to Mineralogy and Petrology. 157(4), 541-558. https://doi.org/10.1007/s00410-008-0351-8

Anderson, R. B., Long, S. P., Horton, B. K., Calle, A. Z., & Ramirez, V. (2017). Shortening and structural architecture of the Andean fold-thrust belt of southern Bolivia (21°S): Implications for kinematic development and crustal thickening of the central Andes. Geosphere, 13(2), 538-558. https://doi.org/10.1130/ges01433.1

Anderson, V. J., Horton, B. K., Saylor, J. E., Mora, A., Tesón, E., Breecker, D. O., & Ketcham, R. A. (2016). Andean topographic growth and basement uplift in southern Colombia: Implications for the evolution of the Magdalena, Orinoco, and Amazon River systems. Geosphere, 12(4), 1235-1256. https://doi.org/10.1130/ges01294.1

Annen, C., Blundy, J.D., & Sparks, R.S.J. (2006). The genesis of intermediate and silicic magmas in deep crustal hot zones. Journal of Petrology, 47, 505-539. https://doi.org/10.1093/petrology/egi084

Attia, S., Paterson, S. R., Jiang, D., & Miller, R. B. (2022). Spatiotemporally heterogeneous deformation, indirect tectonomagmatic links, and lithospheric evolution during orogenic activity coeval with an arc flare-up. Geosphere, 18(6), 1752-1782. https://doi.org/10.1130/GES02478.1

Avellaneda-Jiménez, D. S., & Monsalve, G. (2022). Arclogite nature of the Colombian Andes magmatic arc root: A receiver-function approach. Tectonophysics, 836(229417), 229417. https://doi.org/10.1016/j.tecto.2022.229417

Bachmann, O., & Bergantz, G. W. (2008). Rhyolites and their source mushes across tectonic settings. Journal of Petrology, 49(12), 2277-2285. https://doi.org/10.1093/petrology/egn068

Bachmann, O., Deering, C. D., Lipman, P. W., & Plummer, C. (2014). Building zoned ignimbrites by recycling silicic cumulates: insight from the 1,000 km3 Carpenter Ridge Tuff, CO. Contributions to Mineralogy and Petrology, 167(6). https://doi.org/10.1007/s00410-014-1025-3

Balica, C., Ducea, M. N., Gehrels, G. E., Kirk, J., Roban, R. D., Luffi, P., Chapman, J. B., Triantafyllou, A., Guo, J., Stoica, A. M., Ruiz, J., Balintoni, I., Profeta, L., Hoffman, D., & Petrescu, L. (2020). A zircon petrochronologic view on granitoids and continental evolution. Earth and Planetary Science Letters, 531(116005). https://doi.org/10.1016/j.epsl.2019.116005

Barbosa-Espitia, Á. A., Kamenov, G. D., Foster, D. A., Restrepo-Moreno, S. A., & Pardo-Trujillo, A. (2019). Contemporaneous Paleogene arc-magmatism within continental and accreted oceanic arc complexes in the northwestern Andes and Panama. Lithos, 348-349. https://doi.org/10.1016/j.lithos.2019.105185

Barth, A. P., Wooden, J. L., Jacobson, C. E., Economos, R. C. (2013). Detrital zircon as a proxy for tracking the magmatic arc system: The California arc example. Geology, 41(2), 223-226. https://doi.org/10.1130/G33619.1

Bayona, G., Baquero, M., Ramírez, C., Tabares, M., Salazar, A. M., Nova, G., Duarte, E., Pardo, A., Plata, A., Jaramillo, C., Rodríguez, G., Caballero, V., Cardona, A., Montes, C., Gómez Marulanda, S., & Cárdenas-Rozo, A. L. (2021). Unravelling the widening of the earliest Andean northern orogen: Maastrichtian to early Eocene intra-basinal deformation in the northern Eastern Cordillera of Colombia. Basin Research, 33(1), 809-845. https://doi.org/10.1111/bre.12496

Bayona, G., Bustamante, C., Nova, G. & Salazar-Franco, A. M. (2020). Jurassic evolution of the northwestern corner of Gondwana: Present knowledge and future challenges in studying Colombian Jurassic rocks. In: Gómez, J. & Pinilla-Pachon, A. O. (editors), The Geology of Colombia, Volume 2 Mesozoic. Servicio Geológico Colombiano, Publicaciones Geológicas Especiales 36, 171-207. https://doi.org/10.32685/pub.esp.36.2019.05

Bayona, G., Cardona, A., Jaramillo, C., Mora, A., Montes, C., Valencia, V., Ayala, C., Montenegro, O., & Ibañez-Mejia, M. (2012). Early Paleogene magmatism in the northern

Andes: Insights on the effects of Oceanic Plateau-continent convergence. Earth and Planetary Science Letters, 331-332, 97-111. https://doi.org/10.1016/j.epsl.2012.03.015

Bayona, G., Montenegro, O., Cardona, A., Jaramillo, C., & Lamus, F. (2010). Estratigrafía, procedencia, subsidencia y exhumación de las unidades paleógenas en el Sinclinal de Usme, sur de la zona axial de la Cordillera Oriental. Geología Colombiana, 35(0), 5-35. https://revistas.unal.edu.co/index.php/geocol/article/view/21100

Bayona, G., Montes, C., Cardona, A., Jaramillo, C., Ojeda, G., Valencia, V., & Ayala-Calvo, C. (2011). Intraplate subsidence and basin filling adjacent to an oceanic arc-continent collision: A case from the southern Caribbean-South America plate margin. Basin Research, 23(4), 403-422. https://doi.org/10.1111/j.1365-2117.2010.00495.x

Beall, A. P., Moresi, L., & Stern, T. (2017). Dripping or delamination? A range of mechanisms for removing the lower crust or lithosphere. Geophysical Journal International, 210(2), 671-692. https://doi.org/10.1093/gji/ggx202

Belousova, E., Griffin, W., O'Reilly, S. Y., & Fisher, N. (2002). Igneous zircon: trace element composition as an indicator of source rock type. Contributions to Mineralogy and Petrology, 143(5), 602-622. https://doi.org/10.1007/s00410-002-0364-7

Best, M. G., Christiansen, E. H., de Silva, S., & Lipman, P. W. (2016). Slab-rollback ignimbrite flare-ups in the southern Great Basin and other Cenozoic American arcs: A distinct style of arc volcanism. Geosphere, 12(4), 1097-1135. https://doi.org/10.1130/ges01285.1

Best, M. G., Christiansen, E. H., Deino, A. L., Gromme, S., Hart, G. L., & Tingey, D. G. (2013). The 36-18 Ma Indian Peak-Caliente ignimbrite field and calderas, southeastern Great Basin, USA: multicyclic super-eruptions. Geosphere, 9(4), 864-950. https://doi.org/10.1130/GES00902.1

Black, L. P., Kamo, S. L., Allen, C. M., Davis, D. W., Aleinikoff, J. N., Valley, J. W., Mundil, R., Campbell, I. H., Korsch, R. J., Williams, I. S., & Foudoulis, C. (2004). Improved 206Pb/238U microprobe geochronology by the monitoring of a trace-element-related matrix effect; SHRIMP, ID-TIMS, ELA-ICP-MS and oxygen isotope documentation for a series of zircon standards. Chemical Geology, 205(1-2), 115-140. https://doi.org/10.1016/j.chemgeo.2004.01.003

Bloch, E., Ibañez-Mejia, M., Murray, K., Vervoort, J., & Müntener, O. (2017). Recent crustal foundering in the Northern Volcanic Zone of the Andean arc: Petrological insights from the

roots of a modern subduction zone. Earth and Planetary Science Letters, 476, 47-58. https://doi.org/10.1016/j.epsl.2017.07.041

Borrero, C. A., & Castillo, H. (2006). Vulcanitas del S-SE de Colombia: retro-arco alcalino y su posible relación con una ventana astenosférica. Boletín de Geología, 28(2).

Bottinga, Y., & Weill, D. F. (1970). Densities of liquid silicate systems calculated from partial molar volumes of oxide components. American Journal of Science, 269(2), 169-182. https://doi.org/10.2475/ajs.269.2.169

Bouvier, A., Vervoort, J. D., & Patchett, P. J. (2008). The Lu-Hf and Sm-Nd isotopic composition of CHUR: constraints from unequilibrated chondrites and implications for the bulk composition of terrestrial planets. Earth and Planetary Science Letters, 273, 48-57. doi:10.1016/j.epsl.2008.06.010

Bowman, E. E., & Ducea, M. N. (2023). Pyroxenite melting at subduction zones. Geology, 51(4), 383-386. https://doi.org/10.1130/g50929.1

Bowman, E. E., Ducea, M. N., & Triantafyllou, A. (2021). Arclogites in the subarc lower crust: Effects of crystallization, partial melting, and retained melt on the foundering ability of residual roots. Journal of Petrology, 62(12). https://doi.org/10.1093/petrology/egab094

Brown, D., & Ryan, P. D. (2011). Arc-continent collision. Frontiers in Earth Sciences, 4. https://doi.org/10.1007/978-3-540-88558-0

Bucheli, C., Pardo, N., Larrea, P., de Ignacio, C., Correa-Tamayo, A. M., Arnosio, M., & Pulgarín, B. A. (2024). What can we learn from geothermobarometry at the dacitic Doña Juana Volcanic Complex (Colombia)? Implications for understanding Pleistocene crystal mushes and pre-eruptive storage conditions in the Northern Andes. Contributions to Mineralogy and Petrology, 179(3). https://doi.org/10.1007/s00410-024-02103-6

Bustamante, C., Archanjo, C. J., Cardona, A., & Restrepo, M. (2021). Magnetic fabric of the Parashi stock and related dyke swarm, Alta Guajira (Colombia): The Caribbean-South American plates oblique convergence. Andean Geology, 48(2), 219-236. https://doi.org/10.5027/andgeov48n2-3332

Bustamante, C., Archanjo, C. J., Cardona, A., & Vervoort, J. D. (2016). Late Jurassic to Early Cretaceous plutonism in the Colombian Andes: A record of long-term arc maturity. Bulletin of the Geological Society of America, 128(11-12), 1762-1779. https://doi.org/10.1130/B31307.1

Bustamante, C., Cardona, A., Archanjo, C. J., Bayona, G., Lara, M., & Valencia, V. (2017). Geochemistry and isotopic signatures of Paleogene plutonic and detrital rocks of the Northern Andes of Colombia: A record of post-collisional arc magmatism. Lithos, 277, 199-209. https://doi.org/10.1016/j.lithos.2016.11.025

Caballero, V. M., Rodríguez, G., Naranjo, J. F., Mora, A. & De La Parra, F. (2020). From facies analysis, stratigraphic surfaces, and depositional sequences to stratigraphic traps in the Eocene - Oligocene record of the southern Llanos Basin and northern Magdalena Basin. In: Gómez, J. & Mateus-Zabala, D. (editors), The Geology of Colombia, Volume 3 Paleogene - Neogene. Servicio Geológico Colombiano, Publicaciones Geológicas Especiales 37, 283-330. Bogotá. https://doi.org/10.32685/pub.esp.37.2019.1

Caffe, P. J., Trumbull, R. B., & Siebel, W. (2012). Petrology of the Coyaguayma ignimbrite, northern Puna of Argentina: Origin and evolution of a peraluminous high-SiO2 rhyolite magma. Lithos, 134-135, 179-200. https://doi.org/10.1016/j.lithos.2011.12.013

Cai, R., Liu, J., Sun, Y., & Gao, R. (2023). Phosphorus deficit in continental crust induced by recycling of apatite-bearing cumulates. Geology, 51(5), 500-504. https://doi.org/10.1130/g51027.1

Calderon-Diaz, L., Zapata, S., Cardona, A., Parra, M., Sobel, E. R., Patiño, A. M., Valencia, V., Jaramillo-Rios, J. S., & Glodny, J. (2024). Cretaceous extensional and contractional stages in the Colombian Andes unraveled by a source-to-sink geochronological and thermochronological study in the Upper Magdalena Basin. Tectonophysics, 878, 230303. https://doi.org/10.1016/j.tecto.2024.230303

Capaldi, T. N., McKenzie, N. R., Horton, B. K., Mackaman-Lofland, C., Colleps, C. L., & Stockli, D. F. (2021). Detrital zircon record of Phanerozoic magmatism in the southern Central Andes. Geosphere, 17(3), 876-897. https://doi.org/10.1130/ges02346.1

Cardona, A., León, S., Jaramillo, J. S., Montes, C., Valencia, V., Vanegas, J., Bustamante, C., & Echeverri, S. (2018). The Paleogene arcs of the northern Andes of Colombia and Panama: Insights on plate kinematic implications from new and existing geochemical, geochronological and isotopic data. Tectonophysics, 749, 88-103. https://doi.org/10.1016/j.tecto.2018.10.032

Cardona, A., Valencia, V. A., Bayona, G., Duque, J., Ducea, M., Gehrels, G., Jaramillo, C., Montes, C., Ojeda, G., & Ruiz, J. (2011). Early-subduction-related orogeny in the northern

Andes: Turonian to Eocene magmatic and provenance record in the Santa Marta Massif and Rancheria Basin, northern Colombia. Terra Nova, 23(1), 26-34. https://doi.org/10.1111/j.1365-3121.2010.00979.x

Carrapa, B., DeCelles, P. G., Ducea, M. N., Jepson, G., Osakwe, A., Balgord, E., Stevens Goddard, A. L., & Giambiagi, L. A. (2022). Estimates of paleo-crustal thickness at Cerro Aconcagua (Southern Central Andes) from detrital proxy-records: Implications for models of continental arc evolution. Earth and Planetary Science Letters, 585, 117526. https://doi.org/10.1016/j.epsl.2022.117526

Cavosie, A. J., Valley, J. W., & Wilde, S. A. (2005). Magmatic δ18O in 4400-3900 Ma detrital zircons: A record of the alteration and recycling of crust in the Early Archean. Earth and Planetary Science Letters, 235(3-4), 663-681. https://doi.org/10.1016/j.epsl.2005.04.028

Cavosie, A. J., Valley, J. W., & Wilde, S. A. (2006). Correlated microanalysis of zircon: Trace element, δ18O, and U-Th-Pb isotopic constraints on the igneous origin of complex >3900 Ma detrital grains. Geochimica et Cosmochimica Acta, 70(22), 5601-5616. https://doi.org/10.1016/j.gca.2006.08.011

Cawood, P. A., Hawkesworth, C. J., & Dhuime, B. (2013). The continental record and the generation of continental crust. Bulletin of the Geological Society of America, 125(1-2), 14-32. https://doi.org/10.1130/B30722.1

Cawood, P. A., Kröner, A., Collins, W. J., Kusky, T. M., Mooney, W. D., & Windley, B. F. (2009). Accretionary orogens through Earth history. Geological Society Special Publication, 318(1), 1-36. https://doi.org/10.1144/sp318.1

Chang, Z., Vervoort, J. D., McClelland, W. C., & Knaack, C. (2006). U-Pb dating of zircon by LA-ICP-MS. Geochemistry, Geophysics, Geosystems: G(3), 7(5). https://doi.org/10.1029/2005gc001100

Chapman, J. B., Ducea, M. N., DeCelles, P. G., & Profeta, L. (2015). Tracking changes in crustal thickness during orogenic evolution with Sr/Y: An example from the North American Cordillera. Geology, 43(10), 919-922. https://doi.org/10.1130/G36996.1

Chapman, J. B., Shields, J. E., Ducea, M. N., Paterson, S. R., Attia, S., & Ardill, K. E. (2021). The causes of continental arc flare ups and drivers of episodic magmatic activity in Cordilleran orogenic systems. Lithos, 398-399, 106307. https://doi.org/10.1016/j.lithos.2021.106307

Chase, C. G., Sussman, A. J., & Coblentz, D. D. (2009). Curved Andes: Geoid, forebulge, and flexure. Lithosphere, 1(6), 358-363. https://doi.org/10.1130/l67.1

Chen, J., Kufner, S.-K., Yuan, X., Heit, B., Wu, H., Yang, D., Schurr, B., & Kay, S. (2020). Lithospheric delamination beneath the southern Puna plateau resolved by local earthquake tomography. Journal of Geophysical Research. Solid Earth, 125(10). https://doi.org/10.1029/2019jb019040

Chiarabba, C., De Gori, P., Faccenna, C., Speranza, F., Seccia, D., Dionicio, V., & Prieto, G. A. (2015). Subduction system and flat slab beneath the Eastern Cordillera of Colombia. Geochemistry, Geophysics, Geosystems: G(3), 17(1), 16-27. https://doi.org/10.1002/2015gc006048

Chiaradia, M., Müntener, O., Beate, B., & Fontignie, D. (2009). Adakite-like volcanism of Ecuador: Lower crust magmatic evolution and recycling. Contributions to Mineralogy and Petrology, 158(5), 563-588. https://doi.org/10.1007/s00410-009-0397-2

Cilliers, C. D., Tucker, R. T., Crowley, J. L., & Zanno, L. E. (2021). Age constraint for the Moreno Hill Formation (Zuni Basin) by CA-TIMS and LA-ICP-MS detrital zircon geochronology. PeerJ, 9, 1-39. https://doi.org/10.7717/peerj.10948

Claiborne, L. L., Miller, C. F., & Wooden, J. L. (2010). Trace element composition of igneous zircon: A thermal and compositional record of the accumulation and evolution of a large silicic batholith, Spirit Mountain, Nevada. Contributions to Mineralogy and Petrology, 160(4), 511-531. https://doi.org/10.1007/s00410-010-0491-5

Claiborne, L. L, Miller, C. F., Walker, B. A., Wooden, J. L., Mazdab, F. K., & Bea, F. (2006). Tracking magmatic processes through Zr/Hf ratios in rocks and Hf and Ti zoning in zircons: An example from the Spirit Mountain batholith, Nevada. Mineralogical Magazine, 70(5), 517-543. https://doi.org/10.1180/0026461067050348

Cochrane, R., Spikings, R., Gerdes, A., Ulianov, A., Mora, A., Villagómez, D., Putlitz, B., & Chiaradia, M. (2014). Permo-Triassic anatexis, continental rifting and the disassembly of western Pangaea. Lithos, 190-191, 383-402. https://doi.org/10.1016/j.lithos.2013.12.020

Condie, K. C. (2007). Accretionary orogens in space and time. In Geological Society of America Memoirs, 145-158. Geological Society of America. https://doi.org/10.1130/2007.1200(09)

Condon D. J., Schoene B., McLean N. M., Bowring S. A., Parrish R, 2015, Metrology and traceability of U-Pb isotope dilution geochronology (EARTHTIME Tracer Calibration Part

I). Geochimica et Cosmochimica Acta, 164, 464-480. https://doi.org/10.1016/j.gca.2015.05.026

Corfu, F. (2003). Atlas of zircon textures. Reviews in Mineralogy and Geochemistry, 53(1), 469-500. https://doi.org/10.2113/0530469

Correa-Tamayo, A. M., 2009. Estudio petrologico, geoquímico y vulcanológico para establecer la evolución magmática del complejo volcánico Nevado del Huila, Colombia. Universidad Complutense de Madrid, 545 p.

Correa-Tamayo, A. M., Pulgarín-Alzate, B. A. & Ancochea-Soto, E. (2020). The Nevado del Huila Volcanic Complex. In: Gómez, J. & Pinilla-Pachon, A. O. (editors), The Geology of Colombia, Volume 4 Quaternary. Servicio Geológico Colombiano, Publicaciones Geológicas Especiales 38, 227-265. Bogotá. doi.org/10.32685/pub.esp.38.2019.06

Crowley, J. L., Schoene, B., & Bowring, S. A. (2007). U-Pb dating of zircon in the Bishop Tuff at the millennial scale. Geology, 35(12), 1123-1126. https://doi.org/10.1130/G24017A.1

Currie, C. A., Ducea, M. N., DeCelles, P. G., & Beaumont, C. (2015). Geodynamic models of Cordilleran orogens: Gravitational instability of magmatic arc roots. In DeCelles, P. G., Ducea, M. N., Carrapa, B., & Kapp, P. A. (Eds.), Geodynamics of a Cordilleran Orogenic System: The Central Andes of Argentina and Northern Chile (pp. 1-22). Geological Society of America Memoir 212. https://doi.org/10.1130/2015.1212(01)

Dasgupta, R., Hirschmann, M. M., & Smith, N. D. (2007). Partial melting experiments of peridotite + CO2 at 3 GPa and genesis of alkalic ocean island basalts. Journal of Petrology, 48(11), 2093-2124. https://doi.org/10.1093/petrology/egm053

de Silva, S. L., & Kay, S. M. (2018). Turning up the heat: High-flux magmatism in the central Andes. Elements, 14(4), 245-250. https://doi.org/10.2138/gselements.14.4.245

de Silva, S.L., Riggs, N.R., & Barth, A.P. (2015). Quickening the pulse: Fractal tempos in continental arc magmatism. Elements, 11(2), 113-118. https://doi.org/10.2113/gselements.11.2.113

DeCelles, P. G., Ducea, M. N., Kapp, P., & Zandt, G. (2009). Cyclicity in Cordilleran orogenic systems. Nature Geoscience, 2(4), 251-257. https://doi.org/10.1038/ngeo469

Deering, C. D., Bachmann, O., Dufek, J., & Gravley, D. M. (2011). Rift-related transition from andesite to rhyolite volcanism in the Taupo Volcanic Zone (New Zealand) controlled by

crystal-melt dynamics in mush zones with variable mineral assemblages. Journal of Petrology, 52(11), 2243-2263. https://doi.org/10.1093/petrology/egr046

DePaolo, D. J., & Wasserburg, G. J. (1976). Nd isotopic variations and petrogenetic models. Geophysical Research Letters, 3(5), 249-252. https://doi.org/10.1029/gl003i005p00249

DePaolo, D. J., Harrison, T. M., Wielicki, M., Zhao, Z., Zhu, D.-C., Zhang, H., & Mo, X. (2019). Geochemical evidence for thin syn-collision crust and major crustal thickening between 45 and 32 Ma at the southern margin of Tibet. Gondwana Research: International Geoscience Journal, 73, 123-135. https://doi.org/10.1016/j.gr.2019.03.011

Diederix, H., Bohórquez, O. P., Mora-Páez, H., Peláez, J. R., Cardona, L., Corchuelo, Y., Ramírez, J. & Díaz-Mila, F. (2020). The Algeciras Fault System of the Upper Magdalena Valley, Huila Department. In: Gómez, J. & Pinilla-Pachon, A. O. (editors), The Geology of Colombia, Volume 4 Quaternary. Servicio Geológico Colombiano, Publicaciones Geológicas Especiales 38, 423-452. Bogotá. https://doi.org/10.32685/pub.esp.38.2019.12

Draut, A. E., & Clift, P. D. (2001). Geochemical evolution of arc magmatism during arc-continent collision, South Mayo, Ireland. Geology, 29(6), 543-546. https://doi.org/10.1130/0091-7613(2001)029<0543:GEOAMD>2.0.CO;2

Droux, A., & Delaloye, M. (1996). Petrography and geochemistry of Plio-Quaternary calc-alkaline volcanoes of Southwestern Colombia. Journal of South American Earth Sciences, 9(1-2), 27-41. https://doi.org/10.1016/0895-9811(96)00025-9

Ducea, M. N., Bergantz, G. W., Crowley, J. L., & Otamendi, J. (2017). Ultrafast magmatic buildup and diversification to produce continental crust during subduction. Geology, 45(3), 235-238. https://doi.org/10.1130/g38726.1

Ducea, M. N., Chapman, A. D., Bowman, E., & Balica, C. (2021b). Arclogites and their role in continental evolution; part 2: Relationship to batholiths and volcanoes, density and foundering, remelting and long-term storage in the mantle. Earth-Science Reviews, 214, 103476. https://doi.org/10.1016/j.earscirev.2020.103476

Ducea, M. N., Chapman, A. D., Bowman, E., & Triantafyllou, A. (2021a). Arclogites and their role in continental evolution; part 1: Background, locations, petrography, geochemistry, chronology and thermobarometry. Earth-Science Reviews, 214, 103375. https://doi.org/10.1016/j.earscirev.2020.103375

Ducea, M. N., Paterson, S. R., & DeCelles, P. G. (2015b). High-volume magmatic events in subduction systems. Elements, 11(2), 99-104. https://doi.org/10.2113/gselements.11.2.99

Ducea, M. N., Saleeby, J. B., & Bergantz, G. (2015a). The architecture, chemistry, and evolution of continental magmatic arcs. Annual Review of Earth and Planetary Sciences, 43(1), 299-331. https://doi.org/10.1146/annurev-earth-060614-105049

Ducea, M. N., Seclaman, A. C., Murray, K. E., Jianu, D., & Schoenbohm, L. M. (2013). Mantle-drip magmatism beneath the Altiplano-Puna plateau, central Andes. Geology, 41(8), 915-918. https://doi.org/10.1130/g34509.1

Duque-Trujillo, J. F., Bustamante, C., Solari, L., Gómez-Mafla, Á., Toro-Villegas, G., & Hoyos, S. (2019b). Reviewing the Antioquia batholith and satellite bodies : a record of Late Cretaceous to Eocene syn- to post-collisional arc magmatism in the Central Cordillera of Colombia. Andean Geology, 46(1), 82-101. https://doi.org/10.5027/andgeoV46n1-3124

Duque-Trujillo, J. F., Orozco-Esquivel, T., Sánchez, C. J., & Cárdenas-Rozo, A. L. (2019a). Paleogene magmatism of the Maracaibo Block and its tectonic significance. In Geology and Tectonics of Northwestern South America, Frontiers in Earth Sciences, (pp. 551-601). https://doi.org/10.1007/978-3-319-76132-9_7

Echeverri, S., Cardona, A., Pardo, A., Monsalve, G., Valencia, V. A., Borrero, C., Rosero, S., & López, S. (2015). Regional provenance from southwestern Colombia fore-arc and intra-arc basins: implications for Middle to Late Miocene orogeny in the Northern Andes. Terra Nova, 27(5), 356-363. https://doi.org/10.1111/ter.12167

Errázuriz-Henao, C., Gómez-Tuena, A., Duque-Trujillo, J., & Weber, M. (2019). The role of subducted sediments in the formation of intermediate mantle-derived magmas from the Northern Colombian Andes. Lithos, 336-337, 151-168. https://doi.org/10.1016/j.lithos.2019.04.007

Faccenna, C., & Becker, T. W. (2020). Topographic expressions of mantle dynamics in the Mediterranean. Earth-Science Reviews, 209, 103327. https://doi.org/10.1016/j.earscirev.2020.103327

Faccenna, C., Becker, T. W., Auer, L., Billi, A., Boschi, L., Brun, J. P., Capitanio, F. A., Funiciello, F., Horvàth, F., Jolivet, L., Piromallo, C., Royden, L., Rossetti, F., & Serpelloni, E. (2014). Mantle dynamics in the Mediterranean: Mediterranean dynamic. Reviews of Geophysics, 52(3), 283-332. https://doi.org/10.1002/2013rg000444

Ferrari, L., Petrone, C. M., & Francalanci, L. (2001). Generation of oceanic-island basalt-type volcanism in the western Trans-Mexican volcanic belt by slab rollback, asthenosphere infiltration, and variable flux melting. Geology, 29(6), 507. https://doi.org/10.1130/0091-7613(2001)029<0507:gooibt>2.0.co;2

Ferry, J. M., & Watson, E. B. (2007). New thermodynamic models and revised calibrations for the Ti-in-zircon and Zr-in-rutile thermometers. Contributions to Mineralogy and Petrology, 154(4), 429-437. https://doi.org/10.1007/s00410-007-0201-0

Fisher, C. M., Vervoort, J. D., & DuFrane, S. A. (2014). Accurate Hf isotope determinations of complex zircons using the “laser ablation split stream” method. Geochemistry, Geophysics, Geosystems: G(3), 15(1), 121-139. https://doi.org/10.1002/2013gc004962

Foley, M. L., Putlitz, B., Baumgartner, L. P., Bégué, F., Siron, G., & Kosmal, A. (2023). Generating large volumes of crust-derived high δ18O rhyolites in the Chon Aike Silicic Large Igneous Province, Patagonia. Geosphere, 19(4), 975-1005. https://doi.org/10.1130/ges02551.1

Gale, A., Dalton, C. A., Langmuir, C. H., Su, Y., & Schilling, J.-G. (2013). The mean composition of ocean ridge basalts: MEAN MORB. Geochemistry, Geophysics, Geosystems: G(3), 14(3), 489-518. https://doi.org/10.1029/2012gc004334

Galer, S. J. G. & Abouchami, W. (1998). Practical application of lead triple spiking for correction of instrumental mass discrimination. Mineralogical Magazine, 62A(1), 491-492. https://doi.org/10.1180/minmag.1998.62a.1.260

Gall, H., Furman, T., Hanan, B., Kürkcüoğlu, B., Sayıt, K., Yürür, T., Sjoblom, M.P., Şen, E., Şen, P.A. (2021). Post-delamination magmatism in south-central Anatolia. Lithos 398-399. https://doi.org/10.1016/j.lithos.2021.106299

Ganade, C. E., Lanari, P., Rubatto, D., Hermann, J., Weinberg, R. F., Basei, M. A. S., Tesser, L. R., Caby, R., Agbossoumondé, Y., & Ribeiro, C. M. (2021). Magmatic flare-up causes crustal thickening at the transition from subduction to continental collision. Communications Earth & Environment, 2(1), 1-10. https://doi.org/10.1038/s43247-021-00103-z

Garrison, J. M., Sims, K. W. W., Yogodzinski, G. M., Escobar, R. D., Scott, S., Mothes, P., Hall, M. L., & Ramon, P. (2018). Shallow-level differentiation of phonolitic lavas from Sumaco

Volcano, Ecuador. Contributions to Mineralogy and Petrology, 173(1). https://doi.org/10.1007/s00410-017-1431-4

Gaschnig, R. M., Vervoort, J. D., Lewis, R. S., & Tikoff, B. (2011). Isotopic evolution of the Idaho batholith and Challis intrusive province, northern US Cordillera. Journal of Petrology, 52(12), 2397-2429. doi.org/10.1093/petrology/egr050

Gaschnig, R. M., Vervoort, J. D., Tikoff, B., & Lewis, R. S. (2017). Construction and preservation of batholiths in the northern U.S. Cordillera. Lithosphere, 9(2), 315-324. https://doi.org/10.1130/L497.1

Gehrels, G. (2014). Detrital zircon U-Pb geochronology applied to tectonics. Annual Review of Earth and Planetary Sciences, 42, 127-149. https://doi.org/10.1146/annurev-earth-050212-124012

Gehrels, G., Valencia, V. A., & Ruiz, J. (2008). Enhanced precision, accuracy, efficiency, and spatial resolution of U-Pb ages by laser ablation-multicollector-inductively coupled plasma-mass spectrometry. Geochemistry, Geophysics, Geosystems: G(3), 9(3), 1-13. https://doi.org/10.1029/2007GC001805

George, S. W. M., Horton, B. K., Vallejo, C., Jackson, L. J., & Gutierrez, E. G. (2021). Did accretion of the Caribbean oceanic plateau drive rapid crustal thickening in the northern Andes? Geology, 49(8), 936-940. https://doi.org/10.1130/g48509.1

Gerstenberger, H., & Haase, G. (1997). A highly effective emitter substance for mass spectrometric Pb isotope ratio determinations. Chemical Geology, 136(3-4), 309-312. https://doi.org/10.1016/s0009-2541(96)00033-2

Gerya, T. V., & Meilick, F. I. (2011). Geodynamic regimes of subduction under an active margin: Effects of rheological weakening by fluids and melts. Journal of Metamorphic Geology, 29(1), 7-31. https://doi.org/10.1111/j.1525-1314.2010.00904.x

Giambiagi, L., Tassara, A., Echaurren, A., Julve, J., Quiroga, R., Barrionuevo, M., Liu, S., Echeverría, I., Mardónez, D., Suriano, J., Mescua, J., Lossada, A. C., Spagnotto, S., Bertoa, M., & Lothari, L. (2022). Crustal anatomy and evolution of a subduction-related orogenic system: Insights from the Southern Central Andes (22-35°S). Earth-Science Reviews, 232(104138), 104138. https://doi.org/10.1016/j.earscirev.2022.104138

Gianola, O., Costa, B., Ferri, F., Gilio, M., Petrelli, M., Murri, M., Barbaro, A., Alvaro, M., Rodríguez-Vargas, A., Poli, S., & Cesare, B. (2023). Melt inclusions in arclogitic xenoliths

constrain the genesis of the lower continental arc crust beneath the northern volcanic zone, Colombia. Journal of Petrology, 64(6). https://doi.org/10.1093/petrology/egad038

Gil-Rodriguez, J. (2014). Petrology of the betulia igneous complex, Cauca, Colombia. Journal of South American Earth Sciences, 56, 339-356. https://doi.org/10.1016/j.jsames.2014.09.016

Glazner, A. F., Coleman, D. S., & Mills, R. D. (2015). The volcanic-plutonic connection. In Physical Geology of Shallow Magmatic Systems (pp. 61–82). Springer International Publishing. https://doi.org/10.1007/978-3-319-14084-1

Global Volcanism Program. (2023). Volcanoes of the World, 5.1.5. compiled by Venzke, E, Distributed by Smithsonian Institution. https://doi.org/10.5479/si.GVP.VOTW5-2023.5.1

Göğüş, O. H., & Pysklywec, R. N. (2008). Mantle lithosphere delamination driving plateau uplift and synconvergent extension in eastern Anatolia. Geology, 36(9), 723. https://doi.org/10.1130/g24982a.1

Gómez, J., & Montes, N. E. (2020). Mapa Geológico de Colombia en Relieve (Vol. 1). https://www2.sgc.gov.co/MGC/Paginas/mgc_1M2020.aspx

Gómez, J., Nivia, Á., Montes, N. E., Almanza, M. F., Alcárcel, F. A., & Madrid, C. A. (2015). Compilando la geología de Colombia: Una visión a 2015. Bogotá. Servicio Geológico Colombiano, Publicaciones Geológicas Especiales, 33.

Gómez-Tuena, A., Díaz-Bravo, B., Vázquez-Duarte, A.V., Pérez-Arvizu, O., & Mori, L. (2014). Andesite petrogenesis by slab-derived plume pollution of a continental rift. Geological Society Special Publications 385, 65-101. https://doi.org/10.1144/SP385.4

González, P. D., Sato, A. M., Naipauer, M., Varela, R., Basei, M., Sato, K., Llambías, E. J., Chemale, F., & Dorado, A. C. (2018). Patagonia-Antarctica Early Paleozoic conjugate margins: Cambrian synsedimentary silicic magmatism, U-Pb dating of K-bentonites, and related volcanogenic rocks. Gondwana Research, 63, 186-225. https://doi.org/10.1016/j.gr.2018.05.015

Gravley, D. M., Deering, C. D., Leonard, G. S., & Rowland, J. V. (2016). Ignimbrite flare-ups and their drivers: A New Zealand perspective. Earth-Science Reviews, 162, 65-82. https://doi.org/10.1016/j.earscirev.2016.09.007

Grimes, C. B., John, B. E., Cheadle, M. J., Mazdab, F. K., Wooden, J. L., Swapp, S., & Schwartz, J. J. (2009). On the occurrence, trace element geochemistry, and crystallization history of

zircon from in situ ocean lithosphere. Contributions to Mineralogy and Petrology, 158(6), 757-783. https://doi.org/10.1007/s00410-009-0409-2

Grimes, C. B., Wooden, J. L., Cheadle, M. J., & John, B. E. (2015). "Fingerprinting" tectono-magmatic provenance using trace elements in igneous zircon. Contributions to Mineralogy and Petrology, 170(5-6), 1-26. https://doi.org/10.1007/s00410-015-1199-3

Grove, T. L., Till, C. B., & Krawczynski, M. J. (2012). The role of H2O in subduction zone magmatism. Annual Review of Earth and Planetary Sciences, 40(1), 413-439. https://doi.org/10.1146/annurev-earth-042711-105310

Grove, T. L., Till, C. B., Lev, E., Chatterjee, N., & Médard, E. (2009). Kinematic variables and water transport control the formation and location of arc volcanoes. Nature, 459(7247), 694-697. https://doi.org/10.1038/nature08044

Hammersley, L., DePaolo, D. J., Beate, B., Deino, A. L. (2022). Rhyolite ignimbrite generation in the northern andes: The chalupas caldera, Ecuador, In: Sims, K. W. W., Maher, K., Schrag, D. P. (Eds.), Isotopic Constraints on Earth System Processes. American Geophysical Union, pp. 87-132. https://doi.org/10.1002/9781119595007.ch05

Haschke, M., Günther, A. (2003). Balancing crustal thickening in arcs by tectonic vs. magmatic means. Geology 31, 933-936. https://doi.org/10.1130/G19945.1

Hayden, L. A., & Watson, E. B. (2007). Rutile saturation in hydrous siliceous melts and its bearing on Ti-thermometry of quartz and zircon. Earth and Planetary Science Letters, 258(3-4), 561-568. https://doi.org/10.1016/j.epsl.2007.04.020

Hayes, G. P., Moore, G. L., Portner, D. E., Hearne, M., Flamme, H., Furtney, M., & Smoczyk, G. M. (2018). Slab2, a comprehensive subduction zone geometry model. Science, 362(6410), 58-61. https://doi.org/10.1126/science.aat4723

Herriott, T. M., Crowley, J. L., Schmitz, M. D., Wartes, M. A., & Gillis, R. J. (2019). Exploring the law of detrital zircon: LA-ICP-MS and CA-TIMS geochronology of Jurassic forearc strata, Cook Inlet, Alaska, USA. Geology, 47(11), 1044-1048. https://doi.org/10.1130/G46312.1

Hiess, J., Condon, D. J., McLean, N., & Noble, S. R. (2012). 238U/ 235U systematics in terrestrial uranium-bearing minerals. Science, 335(6076), 1610-1614. https://doi.org/10.1126/science.1215507

Hildreth, W., & Moorbath, S. (1988). Crustal contributions to arc magmatism in the Andes of Central Chile. Contributions to Mineralogy and Petrology, 98(4), 455-489. https://doi.org/10.1007/bf00372365

Hildreth, W., Fierstein, J., Siems, D. F., Budahn, J. R., & Ruíz, J. (2004). Rear-arc vs. arc-front volcanoes in the Katmai reach of the Alaska Peninsula: a critical appraisal of across-arc compositional variation. Contributions to Mineralogy and Petrology, 147(3), 243-275. https://doi.org/10.1007/s00410-004-0558-2

Hirschmann, M. M., Kogiso, T., Baker, M. B., & Stolper, E. M. (2003). Alkalic magmas generated by partial melting of garnet pyroxenite. Geology, 31(6), 481. https://doi.org/10.1130/0091-7613(2003)031<0481:amgbpm>2.0.co;2

Holder, R. M., Yakymchuk, C., & Viete, D. R. (2020). Accessory Mineral Eu Anomalies in Suprasolidus Rocks: Beyond Feldspar. Geochemistry, Geophysics, Geosystems: G(3), 21(8), 1-16. https://doi.org/10.1029/2020GC009052

Holtz, F., & Johannes, W. (1994). Maximum and minimum water contents of granitic melts: implications for chemical and physical properties of ascending magmas. Lithos, 32(1-2), 149-159. https://doi.org/10.1016/0024-4937(94)90027-2

Horton, B. K. (2018). Sedimentary record of Andean mountain building. Earth-Science Reviews, 178, 279-309. https://doi.org/10.1016/j.earscirev.2017.11.025

Horton, B. K., Anderson, V. J., Caballero, V., Saylor, J. E., Nie, J., Parra, M., & Mora, A. (2015). Application of detrital zircon U-Pb geochronology to surface and subsurface correlations of provenance, paleodrainage, and tectonics of the Middle Magdalena Valley Basin of Colombia. Geosphere, 11(6), 1790-1811. https://doi.org/10.1130/GES01251.1

Horton, B. K., Saylor, J. E., Nie, J., Mora, A., Parra, M., Reyes-Harker, A., & Stockli, D. F. (2010). Linking sedimentation in the northern Andes to basement configuration, Mesozoic extension, and Cenozoic shortening: Evidence from detrital zircon U-Pb ages, Eastern Cordillera, Colombia. Bulletin of the Geological Society of America, 122(9-10), 1423-1442. https://doi.org/10.1130/B30118.1

Houseman, G. A., McKenzie, D. P., & Molnar, P. (1981). Convective instability of a thickened boundary layer and its relevance for the thermal evolution of continental convergent belts. Journal of Geophysical Research, 86, 6115-6132. https://doi.org/10.1029/jb086ib07p06115

Iizuka, T., Yamaguchi, T., Itano, K., Hibiya, Y., & Suzuki, K. (2018). What Hf isotopes in zircon tell us about crust-mantle evolution. Lithos, 274-275, 304-327. http://dx.doi.org/10.1016/j.lithos.2017.01.006

Jaffey, A. H., Flynn, K. F., Glendenin, L. E., Bentley, W. C., and Essling, A. M. (1971). Precision measurements of half-lives and specific activities of 235U and 238U, Physical Review C, 4:1889-1906. https://doi.org/10.1103/PhysRevC.4.1889

Jagoutz, O. (2014). Arc crustal differentiation mechanisms. Earth and Planetary Science Letters, 396, 267-277. https://doi.org/10.1016/j.epsl.2014.03.060

Jagoutz, O., & Behn, M. D. (2013). Foundering of lower island-arc crust as an explanation for the origin of the continental Moho. Nature, 504(7478), 131–134. https://doi.org/10.1038/nature12758

Jagoutz, O., & Kelemen, P. B. (2015). Role of arc processes in the formation of continental crust. Annual Review of Earth and Planetary Sciences, 43(1), 363-404. https://doi.org/10.1146/annurev-earth-040809-152345

Jagoutz, O., & Klein, B. (2018). On the importance of crystallization-differentiation for the generation of SiO2-rich melts and the compositional build-up of arc (and continental) crust. American Journal of Science, 318(1), 29-63. https://doi.org/10.2475/01.2018.03

Jagoutz, O., & Schmidt, M. W. (2013). The composition of the foundered complement to the continental crust and a re-evaluation of fluxes in arcs. Earth and Planetary Science Letters, 371-372, 177-190. https://doi.org/10.1016/j.epsl.2013.03.051

Jaramillo, C., & Cárdenas, A. (2013). Global warming and neotropical rainforests: A historical perspective. Annual Review of Earth and Planetary Sciences, 41(1), 741-766. https://doi.org/10.1146/annurev-earth-042711-105403

Jaramillo, J. S., Cardona, A., León, S., Valencia, V., & Vinasco, C. (2017). Geochemistry and geochronology from Cretaceous magmatic and sedimentary rocks at 6°35′ N, western flank of the Central cordillera (Colombian Andes): Magmatic record of arc growth and collision. Journal of South American Earth Sciences, 76, 460-481. https://doi.org/10.1016/j.jsames.2017.04.012

Jaramillo, J. S., Cardona, A., Monsalve, G., Valencia, V., & León, S. (2019). Petrogenesis of the late Miocene Combia volcanic complex, northwestern Colombian Andes: Tectonic

implication of short term and compositionally heterogeneous arc magmatism. Lithos, 330-331, 194-210. https://doi.org/10.1016/j.lithos.2019.02.017

Jaramillo, J. S., Zapata, S., Carvalho, M., Cardona, A., Jaramillo, C., Crowley, J. L., Bayona, G., & Caballero-Rodriguez, D. (2022). Diverse magmatic evolutionary trends of the northern Andes unraveled by Paleocene to early Eocene detrital zircon geochemistry. Geochemistry, Geophysics, Geosystems: G(3), 23(9). https://doi.org/10.1029/2021gc010113

Jaramillo, J.S., Cardona, A., Zapata, S., Jaramillo, C., & Valencia, V. (2020). Neogene magmatic record of the southern Colombian Andes: tectonic and mountain building implications. GSA meeting. doi: 10.1130/abs/2020AM-358191.

Jaramillo-Ríos, J. S., Cardona, A., Zapata, S., Valencia, V., Monsalve, G., & Vervoort, J. (2024). A mantle origin for Pliocene SiO2-rich ignimbrites in the modern Colombian magmatic arc. Lithos, 480-481, 107666. https://doi.org/10.1016/j.lithos.2024.107666

Jaramillo-Ríos, J. S., Cardona, A., Zapata, S., & Valencia, V. (2023). High-volume ignimbrites and alkaline basalts triggered by slab-retreating and incipient delamination in the Central Volcanic zone of the Colombian Andes. XVI Congreso Geológico Chileno.

Johnson, D.M., Hooper, P.R., & Conrey, R.M., (1999). XRF analysis of rocks and minerals for major and trace elements on a single low dilution Li-tetraborate fused bead. Adv. X-ray Anal, v. 41, p. 843-867.

Jordan, T. E., Reynolds, J. H., III, & Erikson, J. P. (1997). Variability in age of initial shortening and uplift in the central Andes, 16-33°30′S. In Tectonic Uplift and Climate Change (pp. 41-61). Springer.

Juggins, S. (2020). rioja: Analysis of quaternary science data, R package version (0.9-26). Retrieved from https://cran.r-project.org/package=rioja

Kaoungku, N., Suksut, K., Chanklan, R., Kerdprasop, K., & Kerdprasop, N. (2018). The silhouette width criterion for clustering and association mining to select image features. International Journal of Machine Learning and Computing, 8(1), 69-73. https://doi.org/10.18178/ijmlc.2018.8.1.665

Karlstrom, L., Lee, C.-T. A., & Manga, M. (2014). The role of magmatically driven lithospheric thickening on arc front migration. Geochemistry, Geophysics, Geosystems: G(3), 15(6), 2655-2675. https://doi.org/10.1002/2014gc005355

Kay, R. W., & Kay, S. M. (1993). Delamination and delamination magmatism. Tectonophysics, 219(1-3), 177-189. https://doi.org/10.1016/0040-1951(93)90295-u

Kay, S. M., Coira, B. L., Caffe, P. J., & Chen, C. H. (2010). Regional chemical diversity, crustal and mantle sources and evolution of central Andean Puna plateau ignimbrites. Journal of Volcanology and Geothermal Research, 198(1-2), 81-111. https://doi.org/10.1016/j.jvolgeores.2010.08.013

Kay, S. M., Coira, B., Wörner, G., Kay, R. W., & Singer, B. S. (2011). Geochemical, isotopic and single crystal 40Ar/39Ar age constraints on the evolution of the Cerro Galán ignimbrites. Bulletin of Volcanology, 73(10), 1487-1511. https://doi.org/10.1007/s00445-010-0410-7

Kay, S. M., Mpodozis, C., & Gardeweg, M. (2014). Magma sources and tectonic setting of Central Andean andesites (25.5-288S) related to crustal thickening, forearc subduction erosion and delamination. Geological Society Special Publication, 385(1), 303-334. https://doi.org/10.1144/SP385.11

Kay, S. M., Mpodozis, C., Ramos, V. A., & Munizaga, F. (1991). Magma source variations for mid-late Tertiary magmatic rocks associated with a shallowing subduction zone and a thickening crust in the central Andes (28 to 33°S). Geological Society of America Special Publication, 265, 113-137. https://doi.org/10.1130/SPE265-p113

Kennan, L., & Pindell, J. L. (2009). Dextral shear, terrane accretion and basin formation in the Northern Andes: Best explained by interaction with a Pacific-derived Caribbean plate? Geological Society Special Publication, 328, 487-531. https://doi.org/10.1144/SP328.20

Kennedy, A. K., Wotzlaw, J. F., Schaltegger, U., Crowley, J. L., Schmitz, M., 2014, Eocene zircon reference material for microanalysis of U-Th-Pb isotopes and trace elements. The Canadian Mineralogist, 52, 409-421.

Kerr, A. C., Marriner, G. F., Tarney, J., Nivia, A., Saunders, A. D., Thirlwall, M. F., & Sinton, C. W. (1997). Cretaceous basaltic terranes in Western Colombia: Elemental, chronological and Sr-Nd isotopic constraints on petrogenesis. Journal of Petrology, 38(6), 677-702. https://doi.org/10.1093/petroj/38.6.677

Kerr, A. C., Tarney, J., Marriner, G. F., Nivia, A., Klaver, G. T., & Saunders, A. D. (1996). The geochemistry and tectonic setting of late Cretaceous Caribbean and Colombian volcanism.

Journal of South American Earth Sciences, 9(1-2), 111-120. https://doi.org/10.1016/0895-9811(96)00031-4

Kirkland, C. L., Smithies, R. H., Taylor, R. J. M., Evans, N., & McDonald, B. (2015). Zircon Th/U ratios in magmatic environs. Lithos, 212-215, 397-414. https://doi.org/10.1016/j.lithos.2014.11.021

Klein, B. Z., Jagoutz, O., Schmidt, M. W., & Kueter, N. (2023). A global assessment of the controls on the fractionation of arc magmas. Geochemistry, Geophysics, Geosystems: G(3), 24, e2023GC010888. https://doi.org/10.1029/2023GC010888

Kogiso, T., Hirshcmann, M. M., & Petermann, M. (2004). High-pressure partial melting of mafic lithologies in the mantle. Journal of Petrology, 45(12), 2407-2422. https://doi.org/10.1093/petrology/egh057

Kohut, E. J., Stern, R. J., Kent, A. J. R., Nielsen, R. L., Bloomer, S. H., & Leybourne, M. (2006). Evidence for adiabatic decompression melting in the Southern Mariana Arc from high-Mg lavas and melt inclusions. Contributions to Mineralogy and Petrology, 152(2), 201-221. https://doi.org/10.1007/s00410-006-0102-7

Koppers, A. A. P., Becker, T. W., Jackson, M. G., Konrad, K., Müller, R. D., Romanowicz, B., Steinberger, B., & Whittaker, J. M. (2021). Mantle plumes and their role in Earth processes. Nature Reviews. Earth & Environment, 2(6), 382-401. https://doi.org/10.1038/s43017-021-00168-6

Krogh, T. E. (1973). A low contamination method for hydrothermal decomposition of zircon and extraction of U and Pb for isotopic age determination. Geochimica et Cosmochimica Acta, 37(3), 485-494. https://doi.org/10.1016/0016-7037(73)90213-5

Kroonenberg, S. B., León-Silvestre, L. A., Pastana, J. M. do N., & Pessoa, M. R. (1981). Ignimbritas Pliopleistocenicas en el Suroeste del Huila, Colombia y su Influencia en el Desarrollo Morfológico. CIAF, 6(1-3), 293-3214.

Kroonenberg, S. B., Pichler, H., & Diederix, H. (1982). Cenozoic alkalibasaltic to ultrabasic volcanism in the upermost Magdalena Valley, Southern Huila Department, Colombia. Geología Norandina, (5), 19-26.

Kroonenberg, S. B., Pichler, H., & Schmitt-Riegraf, C. (1987). Young alkalibasaltic to nephelinitic volcanism in the Southern Colombian Andes - Origin by subduction of a spreading rift? Zentralblatt für Geologie und Paläontologie, Teil I, 919-936.

Kuiper, K. F., Deino, A., Hilgen, F. J., Krijgsman, W., Renne, P. R., & Wijbrans, J. R., (2008). Synchronizing Rock Clocks of Earth History. Science, 320(5875), 500-504. doi:10.1126/science.1154339

Lambart, S., Laporte, D., Provost, A., & Schiano, P. (2012). Fate of pyroxenite-derived melts in the peridotitic mantle: Thermodynamic and experimental constraints. Journal of Petrology, 53(3), 451-476. https://doi.org/10.1093/petrology/egr068

Lambart, S., Laporte, D., & Schiano, P. (2013). Markers of the pyroxenite contribution in the major-element compositions of oceanic basalts: Review of the experimental constraints. Lithos, 160-161, 14-36. https://doi.org/10.1016/j.lithos.2012.11.018

Lanphere, M. A., & Baadsgaard, H. (2001). Precise K-Ar, 40Ar/39Ar, Rb-Sr and U/Pb mineral ages from the 27.5 Ma Fish Canyon Tuff reference standard. Chemical Geology, 175(3-4), 653-671. https://doi.org/10.1016/s0009-2541(00)00291-6

Le Bas, M. J., Maitre, R. W. L., Streckeisen, A., Zanettin, B., & IUGS Subcommission on the Systematics of Igneous Rocks. (1986). A chemical classification of volcanic rocks based on the total alkali-silica diagram. Journal of Petrology, 27(3), 745-750. https://doi.org/10.1093/petrology/27.3.745

Le Roux, V., Lee, C.-T. A., & Turner, S. J. (2010). Zn/Fe systematics in mafic and ultramafic systems: Implications for detecting major element heterogeneities in the Earth's mantle. Geochimica et Cosmochimica Acta, 74(9), 2779-2796. https://doi.org/10.1016/j.gca.2010.02.004

Leal-Mejía, H. (2011). Phanerozoic gold metallogeny in the Colombian Andes: A tectono-magmatic approach, PhD. Thesis. University of Barcelona, 1-1000p.

Leal-Mejía, H., Shaw, R. P., & Melgarejo-i Draper, J. C. (2019). Spatial-Temporal Migration of Granitoid Magmatism and the Phanerozoic Tectono- Magmatic Evolution of the Colombian Andes. In Cediel, C. & Shaw, R. P. (Eds.), Geology and Tectonics of Northwestern South (pp. 253-410).

Lee, C. -T. A. (2014). Physics and chemistry of deep continental crust recycling. Treatise on Geochemistry, 423-456. https://doi.org/10.1016/B978-0-08-095975-7.00314-4

Lee, C. -T. A., & Bachmann, O. (2014). How important is the role of crystal fractionation in making intermediate magmas? Insights from Zr and P systematics. Earth and Planetary Science Letters, 393, 266-274. https://doi.org/10.1016/j.epsl.2014.02.044

Lee, C.-T. A, Cheng, X., & Horodyskyj, U. (2006). The development and refinement of continental arcs by primary basaltic magmatism, garnet pyroxenite accumulation, basaltic recharge and delamination: insights from the Sierra Nevada, California. Contributions to Mineralogy and Petrology, 151(2), 222-242. https://doi.org/10.1007/s00410-005-0056-1

Lee, C.-T. A., & Anderson, D. L. (2015). Continental crust formation at arcs, the arclogite "delamination" cycle, and one origin for fertile melting anomalies in the mantle. Science Bulletin, 60(13), 1141-1156. https://doi.org/10.1007/s11434-015-0828-6

Lee, C.-T. A., Luffi, P., Plank, T., Dalton, H., & Leeman, W. P. (2009). Constraints on the depths and temperatures of basaltic magma generation on Earth and other terrestrial planets using new thermobarometers for mafic magmas. Earth and Planetary Science Letters, 279(1-2), 20-33. https://doi.org/10.1016/j.epsl.2008.12.020

Lee, J. Y., Marti, K., Severinghaus, J. P., Kawamura, K., Yoo, H. S., Lee, J. B., & Kim, J. S. (2006). A redetermination of the isotopic abundances of atmospheric Ar. Geochimica et Cosmochimica Acta, v. 70(17), p. 4507-4512. doi.org/10.1016/j.gca.2006.06.1563

Lemiszki, P. J., & Brown, L. D. (1988). Variable crustal structure of strike-slip fault zones as observed on deep seismic reflection profiles. Geological Society of America Bulletin, 100(5), 665-676. https://doi.org/10.1130/0016-7606(1988)100<0665:vcsoss>2.3.co;2

León, S., Cardona, A., Parra, M., Sobel, E. R., Jaramillo, J. S., Glodny, J., Valencia, V. A., Chew, D., Montes, C., Posada, G., Monsalve, G., & Pardo-Trujillo, A. (2018). Transition From Collisional to Subduction-Related Regimes: An Example From Neogene Panama-Nazca-South America Interactions: From collision to subduction. Tectonics, 37(1), 119-139. https://doi.org/10.1002/2017tc004785

León, S., Monsalve, G., & Bustamante, C. (2021). How Much Did the Colombian Andes Rise by the Collision of the Caribbean Oceanic Plateau? Geophysical Research Letters, 48(7), 1-11. https://doi.org/10.1029/2021GL093362

Levene, H. (1960). "Robust Tests for Equality of Variances." Contributions to Probability and Statistics. (Edited by I. Olkin, et al.) Stanford: Stanford University Press. Chapter 25. pp. 278-292.

Linnen, R. L., & Keppler, H. (2002). Melt composition control of Zr/Hf fractionation in magmatic processes. Geochimica et Cosmochimica Acta, 66(18), 3293-3301. https://doi.org/10.1016/S0016-7037(02)00924-9

Lonsdale, P. (2005). Creation of the Cocos and Nazca plates by fission of the Farallon plate. Tectonophysics, 404(3-4), 237-264. https://doi.org/10.1016/j.tecto.2005.05.011

Ludwig, K. R., (2003). User's Manual for Isoplot 3.00. Berkeley Geochronology Center: Berkeley, CA, 70 p.

Ludwig, K. R., 2012. Isoplot 3.75: A geochronological toolkit for Microsoft Excel: Spec. Publ., no. 5, Berkeley Geochronological Center, Berkeley, California, 75 p.

Luffi, P., & Ducea, M. N. (2022). Chemical mohometry: Assessing crustal thickness of ancient orogens using geochemical and isotopic data. Reviews of Geophysics, 60(2), e2021RG000753. https://doi.org/10.1029/2021RG000753

Lustrino, M. (2005). How the delamination and detachment of lower crust can influence basaltic magmatism. Earth-Science Reviews, 72(1-2), 21-38. https://doi.org/10.1016/j.earscirev.2005.03.004

MacDonald, W. D., Estrada, J. J., Sierra, G. M., & Gonzalez, H. (1996). Late Cenozoic tectonics and paleomagnetism of North Cauca Basin intrusions, Colombian Andes: Dual rotation modes. Tectonophysics, 261(4), 277-289. https://doi.org/10.1016/0040-1951(95)00184-0

Malusà, M. G., Villa, I. M., Vezzoli, G., & Garzanti, E. (2011). Detrital geochronology of unroofing magmatic complexes and the slow erosion of Oligocene volcanoes in the Alps. Earth and Planetary Science Letters, 301(1-2), 324-336. https://doi.org/10.1016/j.epsl.2010.11.019

Mann, H. B., & Whitney, D. R. (1947). On a Test of Whether one of Two Random Variables is Stochastically Larger than the Other. The annals of mathematical statistics, 18(1), 50-60. https://doi.org/10.1214/aoms/1177730491

Marín-Cerón, M. I., Moriguti, T., Makishima, A., & Nakamura, E. (2010). Slab decarbonation and CO2 recycling in the Southwestern Colombian volcanic arc. Geochimica et Cosmochimica Acta, 74(3), 1104-1121. https://doi.org/10.1016/j.gca.2009.10.031

Marriner, G. F., & Millward, D. (1984). The petrology and geochemistry of Cretaceous to Recent volcanism in Colombia: the magmatic history of an accretionary plate margin. Journal of the Geological Society, 141(3), 473-486. https://doi.org/10.1144/gsjgs.141.3.0473

Mattinson, J. M. (2005). Zircon U-Pb chemical abrasion ("CA-TIMS") method: Combined annealing and multi-step partial dissolution analysis for improved precision and accuracy of zircon ages. Chemical Geology, 220(1-2), 47-66. https://doi.org/10.1016/j.chemgeo.2005.03.011

McCourt, W., Muñoz, U., & Villegas, V. (1990). Regional Geology and Gold Potential of the GuapieNapi Drainage Basin and Upper Timbiqui River. In: British Geological Survey, Overseas Geology Series. Technical Report WC/90/34. Cauca Department, SW Colombia.

McDonough, W. F., & Sun, S.-S. (1995). The composition of the earth. Chemical Geology, 120(3-4), 223-253. https://doi.org/10.1016/0009-2541(94)00140-4

McKay, M. P., Jackson, W. T., & Hessler, A. M. (2018). Tectonic stress regime recorded by zircon Th/U. Gondwana Research, 57, 1-9. https://doi.org/10.1016/j.gr.2018.01.004

McKenzie, N. R., Smye, A. J., Hegde, V. S., & Stockli, D. F. (2018). Continental growth histories revealed by detrital zircon trace elements: A case study from India. Geology, 46(3), 275-278. https://doi.org/10.1130/G39973.1

Médard, E., Schmidt, M. W., Schiano, P., & Ottolini, L. (2006). Melting of amphibole-bearing wehrlites: An experimental study on the origin of ultra-calcic nepheline-normative melts. Journal of Petrology, 47(3), 481-504. https://doi.org/10.1093/petrology/egi083

Miller, C. F., McDowell, S. M., & Mapes, R. W. (2003). Hot and cold granites: Implications of zircon saturation temperatures and preservation of inheritance. Geology, 31(6), 529-532. https://doi.org/10.1130/0091-7613(2003)031<0529:HACGIO>2.0.CO;2

Miller, K. G., Sugarman, P. J., Browning, J. V., Kominz, M. A., Hernández, J. C., Olsson, R. K., Wright, J. D., Feigenson, M. D., & Van Sickel, W. (2003). Late Cretaceous chronology of large, rapid sea-level changes: Glacioeustasy during the greenhouse world. Geology, 31(7), 585. https://doi.org/10.1130/0091-7613(2003)031<0585:lccolr>2.0.co;2

Min K., Mundil R., Renne P. R., and Ludwig K. R. (2000) A test for systematic errors in 40Ar-39Ar geochronology through comparison with U-Pb analysis of a 1.1 Ga rhyolite. Geochimica et Cosmochimica Acta, 64, 73-98. doi.org/10.1016/S0016-7037(99)00204-5

Monsalve, M. L., & Pulgarín, B. (1999). Cadena volcánica de Los Coconucos (Colombia): Centros eruptivos y productos recientes. Boletín Geológico, 37(1-3), 16-51.

Monsalve-Bustamante, M. L. (2020). The volcanic front in Colombia: Segmentation and recent and historical activity. In: Gómez, J. & Pinilla-Pachon, A. O. (editors), The Geology of

Colombia, Volume 4 Quaternary. Servicio Geológico Colombiano, Publicaciones Geológicas Especiales 38, 97-159. Bogotá. https://doi.org/10.32685/pub.esp.38.2019.0

Monsalve-Bustamante, M. L., Gómez, J. & Núñez-Tello, A. (2020). Rear-arc small-volume basaltic volcanism in Colombia: Monogenetic volcanic fields. In: Gómez, J. & Pinilla-Pachon, A. O. (editors), The Geology of Colombia, Volume 4 Quaternary. Servicio Geológico Colombiano, Publicaciones Geológicas Especiales 38, 353-396. Bogotá. https://doi.org/10.32685/pub.esp.38.2019.10

Montes, C., Cardona, A., Jaramillo, C., Pardo, A., Silva, J. C., Valencia, V., Ayala, C., Pérez-Angel, L. C., Rodriguez-Parra, L. A., Ramirez, V., & Niño, H. (2015). Middle Miocene closure of the Central American Seaway. Science, 348(6231), 226-229. https://doi.org/10.1126/science.aaa2815

Montes, C., Cardona, A., McFadden, R., Moron, S. E., Silva, C. A., Restrepo-Moreno, S., Ramirez, D. A., Hoyos, N., Wilson, J., Farris, D., Bayona, G. A., Jaramillo, C. A., Valencia, V., Bryan, J., & Flores, J. A. (2012). Evidence for middle Eocene and younger land emergence in central Panama: Implications for Isthmus closure. Geological Society of America Bulletin, 124(5-6), 780-799. https://doi.org/10.1130/b30528.1

Montes, C., Guzman, G., Bayona, G., Cardona, A., Valencia, V., & Jaramillo, C. (2010). Clockwise rotation of the Santa Marta massif and simultaneous Paleogene to Neogene deformation of the Plato-San Jorge and Cesar-Ranchería basins. Journal of South American Earth Sciences, 29(4), 832-848. https://doi.org/10.1016/j.jsames.2009.07.010

Montes, C., Rodriguez-Corcho, A. F., Bayona, G., Hoyos, N., Zapata, S., & Cardona, A. (2019). Continental margin response to multiple arc-continent collisions: The Northern Andes-Caribbean margin. Earth-Science Reviews, 198, 102903. https://doi.org/10.1016/j.earscirev.2019.102903

Mora-Páez, H., Kellogg, J. N., Freymueller, J. T., Mencin, D., Fernandes, R. M. S., Diederix, H., LaFemina, P., Cardona-Piedrahita, L., Lizarazo, S., Peláez-Gaviria, J.-R., Díaz-Mila, F., Bohórquez-Orozco, O., Giraldo-Londoño, L., & Corchuelo-Cuervo, Y. (2019). Crustal deformation in the northern Andes - A new GPS velocity field. Journal of South American Earth Sciences, 89, 76-91. https://doi.org/10.1016/j.jsames.2018.11.002

Morency, C., & Doin, M.-P. (2004). Numerical simulations of the mantle lithosphere delamination. Journal of Geophysical Research, 109(B03410), 1-17. https://doi.org/10.1029/2003jb002414

Morón, S., Fox, D. L., Feinberg, J. M., Jaramillo, C., Bayona, G., Montes, C., & Bloch, J. I. (2013). Climate change during the Early Paleogene in the Bogotá Basin (Colombia) inferred from paleosol carbon isotope stratigraphy, major oxides, and environmental magnetism. Palaeogeography, Palaeoclimatology, Palaeoecology, 388, 115-127. https://doi.org/10.1016/j.palaeo.2013.08.010

Morton, A. C., & Hallsworth, C. (2007). Stability of detrital heavy minerals during burial diagenesis. In Developments in Sedimentology, 58, 215-245. https://doi.org/10.1016/S0070-4571(07)58007-6

Murray, K. E., Ducea, M. N., & Schoennbohm, L. (2015). Foundering-driven lithospheric melting: The source of central Andean mafic lavas on the Puna Plateau (22 S-27 S). In: DeCelles, P. G., Ducea, M. N., Carrapa, B., & Kapp, P. A. (Eds.), Geodynamics of a Cordilleran Orogenic System: The Central Andes of Argentina and Northern Chile (pp. 139-166). Geological Society of America Memoir 212. https://doi.org/10.1130/2015.1212(08)

Nakakuki, T., & Mura, E. (2013). Dynamics of slab rollback and induced back-arc basin formation. Earth and Planetary Science Letters, 361, 287-297. https://doi.org/10.1016/j.epsl.2012.10.031

Nesbitt, H. W., & Young, G. M. (1982). Early Proterozoic climates and plate motions inferred from major element chemistry of lutites. Nature, 299(5885), 715-717. https://doi.org/10.1038/299715a0

Notini, L., Scambelluri, M., Tommasi, A., Zanetti, A., Ferri, F., Rodríguez-Vargas, A., & Rampone, E. (2024). Probing the deep mantle wedge in an active subduction zone: Xenoliths from the Mercaderes Volcanic District, Southern Colombia. Lithos, 464-465, 107401. https://doi.org/10.1016/j.lithos.2023.107401

O'Hara, M. J. (1968). The bearing of phase equilibria studies in synthetic and natural systems on the origin and evolution of basic and ultrabasic rocks. Earth-Science Reviews 4, 69-133.

Ordoñez, O., Pimentel, M., Armstrong, R., Gioias, S., & Junges, S. (2001). U-Pb SHRIMP and Rb-Sr ages of the Sonsón Batholith. Symposium A Quarterly Journal in Modern Foreign Literatures.

Ort, M. H., Coira, B. L., & Mazzoni, M. M. (1996). Generation of a crust-mantle magma mixture: magma sources and contamination at Cerro Panizos, central Andes. Contributions to Mineralogy and Petrology, 123(3), 308-322. https://doi.org/10.1007/s004100050158

Pardo-Trujillo, A., Cardona, A., Giraldo, A. S., León, S., Vallejo, D. F., Trejos-Tamayo, R., Plata, A., Ceballos, J., Echeverri, S., Barbosa-Espitia, A., Slattery, J., Salazar-Ríos, A., Botello, G. E., Celis, S. A., Osorio-Granada, E., & Giraldo-Villegas, C. A. (2020). Sedimentary record of the Cretaceous-Paleocene arc-continent collision in the northwestern Colombian Andes: Insights from stratigraphic and provenance constraints. Sedimentary Geology, 401, 105627. https://doi.org/10.1016/j.sedgeo.2020.105627

Parra, M., Echeverri, S., Patiño, A. M., Ramírez, J.C., Mora, A., Sobel, E. R., Almendral, A. & Pardo-Trujillo, A. (2020). Cenozoic evolution of the Sierra Nevada de Santa Marta, Colombia. In: Gómez, J. & Mateus-Zabala, D. (editors), The Geology of Colombia, Volume 3 Paleogene - Neogene. Servicio Geológico Colombiano, Publicaciones Geológicas Especiales 37, 185-213. Bogotá. https://doi.org/10.32685/pub.esp.37.2019.07

Paterson, B. A., & Stephens, W. E. (1992). Kinetically induced compositional zoning in titanite: implications for accessory-phase/melt partitioning of trace elements. Contributions to Mineralogy and Petrology, 109(3), 373-385. https://doi.org/10.1007/BF00283325

Paterson, S. R., & Ducea, M. N. (2015). Arc magmatic tempos: Gathering the evidence. Elements, 11(2), 91-98. https://doi.org/10.2113/gselements.11.2.91

Paterson, S. R., Okaya, D., Memeti, V., Economos, R., & Miller, R. B. (2011). Magma addition and flux calculations of incrementally constructed magma chambers in continental margin arcs: Combined field, geochronologic, and thermal modeling studies. Geosphere, 7(6), 1439-1468. https://doi.org/10.1130/ges00696.1

Paton, C., Hellstrom, J., Paul, B., Woodhead, J., & Hergt, J. (2011). Iolite: Freeware for the visualisation and processing of mass spectrometric data. Journal of Analytical Atomic Spectrometry, 26(12), 2508. https://doi.org/10.1039/c1ja10172b

Peccerillo, A., & Taylor, S. R. (1976). Geochemistry of eocene calc-alkaline volcanic rocks from the Kastamonu area, Northern Turkey. Contributions to Mineralogy and Petrology, 58(1), 63-81. https://doi.org/10.1007/bf00384745

Pérez-Consuegra, N., Hoke, G. D., Mora, A., Fitzgerald, P., Sobel, E. R., Sandoval, J. R., Glodny, J., Valencia, V., Parra, M., & Zapata, S. (2021). The case for tectonic control on

erosional exhumation on the tropical northern Andes based on thermochronology data. Tectonics, 40(4). https://doi.org/10.1029/2020tc006652

Piedrahita, V. A., Bernet, M., Chadima, M., Sierra, G. M., Marín-Cerón, M. I., & Toro, G. E. (2017). Detrital zircon fission-track thermochronology and magnetic fabric of the Amagá Formation (Colombia): Intracontinental deformation and exhumation events in the northwestern Andes. Sedimentary Geology, 356, 26-42. https://doi.org/10.1016/j.sedgeo.2017.05.003

Pindell, J. L., & Kennan, L. (2009). Tectonic evolution of the Gulf of Mexico, Caribbean and northern South America in the mantle reference frame: An update. Geological Society Special Publication, 328(1982), 1-55. https://doi.org/10.1144/SP328.1

Pinilla-Ocampo, A., Ríos-Blandon, P. A., Rodríguez-Ramos, B. P., Sánchez-Aguilar, J. J., Pulgarín-Alzate, B., Borrero-Peña, C. A., & Roa-Vargas, H. J. (2008). El Neogeno Volcánico en el Altiplano Nariñense, suroccidente Colombiano. Geología Colombiana, 33, 69-78.

Plank, T. (2005). Constraints from thorium/lanthanum on sediment recycling at subduction zones and the evolution of the continents. Journal of Petrology, 46(5), 921-944. https://doi.org/10.1093/petrology/egi005

Poveda, E., Monsalve, G., & Vargas, C. A. (2015). Receiver functions and crustal structure of the northwestern Andean region, Colombia: Receiver functions in Colombia. Journal of Geophysical Research. Solid Earth, 120(4), 2408-2425. https://doi.org/10.1002/2014jb011304

Priestley, K., Ho, T., & Mitra, S. (2019). The crustal structure of the Himalaya: A synthesis. Geological Society, London, Special Publications, 483(1), 483-516. https://doi.org/10.1144/sp483-2018-127

Profeta, L., Ducea, M. N., Chapman, J. B., Paterson, S. R., Gonzales, S. M. H., Kirsch, M., Petrescu, L., & DeCelles, P. G. (2015). Quantifying crustal thickness over time in magmatic arcs. Scientific Reports, 5(1), 17786. https://doi.org/10.1038/srep17786

Pyle, D. M. (2015). Sizes of volcanic eruptions. In The Encyclopedia of Volcanoes (pp. 257-264). Elsevier.

Quiroga, D. E., Currie, C. A., & Pearse, J. (2024). Lithosphere removal in the Sierra Nevada de Santa Marta, Colombia. Journal of Geophysical Research. Solid Earth, 129, e2023JB027646. https://doi.org/10.1029/2023JB027646

Ramos, V. A. (2009). Anatomy and global context of the Andes: Main geologic features and the Andean orogenic cycle. En S. M. Kay, V. A. Ramos, & W. R. Dickinson (Eds.), Backbone of the Americas: Shallow Subduction, Plateau Uplift, and Ridge and Terrane Collision (pp. 31-65). Geological Society of America, Memoir 204. https://doi.org/10.1130/2009.1204(02)

Ramos, V. A., & Folguera, A. (2009). Andean flat-slab subduction through time. En J. B. Murphy, J. D. Keppie, & A. J. Hynes (Eds.), Ancient Orogens and Modern Analogues (pp. 31-54). Geological Society, London, Special Publications, 327. https://doi.org/10.1144/sp327.3

Restrepo, J. J., & Toussaint, J. F. (1988). Terranes and continental accretion in the Colombian Andes. Episodes. https://doi.org/10.18814/epiiugs/1988/v11i3/006

Restrepo, M., Bustamante, C., Cardona, A., Beltrán-Triviño, A., & Valencia, V. A. (2023). Geochemistry and geochronology of Permian plutonic rocks at the north-western margin of Gondwana. Geological Journal, 58(7), 2818-2840. https://doi.org/10.1002/gj.4743

Rodríguez, E. E., Beck, S. L., Ruiz, M., Meltzer, A., Portner, D. E., Hernández, S., Segovia, M., Agurto-Detzel, H., & Charvis, P. (2023). Seismic imaging of the Northern Andean subduction zone from teleseismic tomography: a torn and fragmented Nazca slab. Geophysical Journal International, 236(1), 593-606. https://doi.org/10.1093/gji/ggad421

Rodríguez, G., & González, H. (2004). Caracteristicas geoquimicas y marco tectonico de los basaltos alcalinos del sur de Colombia. Boletín de Ciencias de la Tierra, 16, 9-22.

Rodríguez, L. M., & Sánchez, J. J. (2018). Morfometría, estratigrafía, petrografía y geoquímica del cono de escoria El Morro, municipio La Argentina (Huila, Colombia). Boletín de Geología, 40(3), 49-65. dx.doi.org/10.18273/revbol.v40n3-2018003

Rodríguez-Alonso, M. D., Peinado, M., López-Plaza, M., Franco, P., Carnicero, A., & Gonzalo, J. C. (2004). Neoproterozoic-Cambrian synsedimentary magmatism in the Central Iberian Zone (Spain): Geology, petrology and geodynamic significance. International Journal of Earth Sciences, 93(5), 897-920. https://doi.org/10.1007/s00531-004-0425-4

Rodriguez-Vargas, A., Koester, E., Mallmann, G., Conceição, R. V., Kawashita, K., & Weber, M. B. I. (2005). Mantle diversity beneath the Colombian Andes, Northern Volcanic Zone:

Constraints from Sr and Nd isotopes. Lithos, 82(3-4), 471-484. https://doi.org/10.1016/j.lithos.2004.09.027

Rosenbaum, G., Caulfield, J. T., Ubide, T., Ward, J. F., Sandiford, D., & Sandiford, M. (2021). Spatially and geochemically anomalous arc magmatism: Insights from the Andean arc. Geochemistry, Geophysics, Geosystems: G(3), 22(6). https://doi.org/10.1029/2021gc009688

Rosenbaum, G., Sandiford, M., Caulfield, J., & Garrison, J. M. (2019). A trapdoor mechanism for slab tearing and melt generation in the northern Andes. Geology, 47(1), 23-26. https://doi.org/10.1130/g45429.1

Ross, J., 2019, NMGRL/pychron v. 18.2: Zenodo, https://doi.org/10.5281/zenodo.3237834.

Rubatto, D. (2002). Zircon trace element geochemistry: partitioning with garnet and the link between U-Pb ages and metamorphism. Chemical Geology, 184(1-2), 123-138. https://doi.org/10.1016/s0009-2541(01)00355-2

Rubatto, D. (2017). Zircon: The Metamorphic Mineral. Reviews in Mineralogy and Geochemistry, 83(1), 261-295.. https://doi.org/10.2138/rmg.2017.83.09

Rudnick, R. L. (1992). Restites, Eu anomalies and the lower continental crust. Geochimica et Cosmochimica Acta, 56(3), 963-970. https://doi.org/10.1016/0016-7037(92)90040-p

Rueda-Gutiérrez, J. B. (2019). Contributions to the Magmatism knowledge of the Central Cordillera of Colombia in its Eastern Flank: Geothermal Area of San Diego, Samaná, Caldas. Boletin de Geologia, 41(2), 45-70. https://doi.org/10.18273/revbol.v41n2-2019003

Sakata, S., Hirakawa, S., Iwano, H., Danhara, T., Guillong, M., & Hirata, T. (2017). A new approach for constraining the magnitude of initial disequilibrium in Quaternary zircons by coupled uranium and thorium decay series dating. Quaternary Geochronology, 38, 1-12. https://doi.org/10.1016/j.quageo.2016.11.002

Salazar, C. A., Bustamante, C., & Archanjo, C. J. (2016). Magnetic fabric (AMS, AAR) of the Santa Marta batholith (northern Colombia) and the shear deformation along the Caribbean Plate margin. Journal of South American Earth Sciences, 70, 55-68. https://doi.org/10.1016/j.jsames.2016.04.011

Salazar-Naranjo, A. F., & Vlach, S. R. F. (2023). New experimental constraints for the evolution and thermobarometry of alkali ultrabasic to intermediate igneous rocks. Journal of Petrology, 64(11). https://doi.org/10.1093/petrology/egad078

Samacá-Torres, W. (2016). Análisis morfométrico y Geomorfológico de la Caldera de Paletará (Cauca), Colombia. MsC. Thesis. Universidad Nacional de Colombia, 1-132p.

Sánchez-Torres, L., Murcia, H., & Schonwalder-Ángel, D. (2022). The northernmost volcanoes in South America (Colombia, 5-6°N): The potentially active Samaná monogenetic volcanic field. Frontiers in earth science, 10. https://doi.org/10.3389/feart.2022.880003

Sanín, M. J., & Galeano, G. (2011). A revision of the Andean wax palms, Ceroxylon (Arecaceae). Phytotaxa, 34(1), 1. https://doi.org/10.11646/phytotaxa.34.1.1

Sanín, M. J., Cardona, A., Valencia-Montoya, W. A., Jiménez-Torres, M. F., Carvalho-Madrigal, S., Gómez, A. C., Bacon, C. D., Roquemen-Tangarife, T., Jaramillo, J. S., Zapata, S., Valencia, V., Arboleda-Valencia, J. W., Vargas, V., & Paris, M. (2022). Volcanic events coincide with plant dispersal across the Northern Andes. Global and Planetary Change, 210, 103757. https://doi.org/10.1016/j.gloplacha.2022.103757

Schaen, A. J., Jicha, B. R., Hodges, K. V., Vermeesch, P., Stelten, M. E., Mercer, C. M., Phillips, D., Rivera, T. A., Jourdan, F., Matchan, E. L., Hemming, S. R., Morgan, L. E., Kelley, S. P., Cassata, W. S., Heizler, M. T., Vasconcelos, P. M., Benowitz, J. A., Koppers, A. A. P., Mark, D. F., … Singer, B. S. (2021). Interpreting and reporting 40Ar/39Ar geochronologic data. Geological Society of America Bulletin, 133(3-4), 461-487. https://doi.org/10.1130/b35560.1

Schaltegger, U., Schmitt, A. K., & Horstwood, M. S. A. (2015). U-Th-Pb zircon geochronology by ID-TIMS, SIMS, and laser ablation ICP-MS: Recipes, interpretations, and opportunities. Chemical Geology, 402, 89-110. https://doi.org/10.1016/j.chemgeo.2015.02.028

Schärer, U. (1984). The effect of initial230Th disequilibrium on young UPb ages: the Makalu case, Himalaya. Earth and Planetary Science Letters, 67(2), 191-204. https://doi.org/10.1016/0012-821x(84)90114-6

Schiano, P., Eiler, J. M., Hutcheon, I. D., & Stolper, E. M. (2000). Primitive CaO-rich, silica-undersaturated melts in island arcs: Evidence for the involvement of clinopyroxene-rich lithologies in the petrogenesis of arc magmas. Geochemistry, Geophysics, Geosystems: G3, 1(1). https://doi.org/10.1029/1999gc000032

Schiano, P., Monzier, M., Eissen, J.-P., Martin, H., & Koga, K. T. (2010). Simple mixing as the major control of the evolution of volcanic suites in the Ecuadorian Andes. Contributions to Mineralogy and Petrology, 160(2), 297-312. https://doi.org/10.1007/s00410-009-0478-2

Schmitz, M. D., & Schoene, B. (2007). Derivation of isotope ratios, errors and error correlations for U-Pb geochronology using 205Pb-235U-(233U)-spiked isotope dilution thermal ionization mass spectrometric data. Geochemistry, Geophysics, Geosystems: G(3), 8(8), Q08006. https://doi.org/10.1029/2006GC001492

Schmitz, M., Ramírez, K., Mazuera, F., Ávila, J., Yegres, L., Bezada, M., & Levander, A. (2021). Moho depth map of northern Venezuela based on wide-angle seismic studies. Journal of South American Earth Sciences, 107, 103088. https://doi.org/10.1016/j.jsames.2020.103088

Schulte-Pelkum, V., & Ben-Zion, Y. (2012). Apparent vertical Moho offsets under continental strike-slip faults from lithology contrasts in the seismogenic crust. Bulletin of the Seismological Society of America, 102(6), 2757-2763. https://doi.org/10.1785/0120120139

Schwartz, T. M., Surpless, K. D., Colgan, J. P., Johnstone, S. A., & Holm-Denoma, C. S. (2021). Detrital zircon record of magmatism and sediment dispersal across the North American Cordilleran arc system (28-48°N). Earth-Science Reviews, 220, 103734. https://doi.org/10.1016/j.earscirev.2021.103734

Sheldrake, T., Caricchi, L., & Scutari, M. (2020). Tectonic Controls on Global Variations of Large-Magnitude Explosive Eruptions in Volcanic Arcs. Frontiers in Earth Science, 8, 1-14. https://doi.org/10.3389/feart.2020.00127

Sláma, J., Košler, J, Condon, D.J., Crowley, J.L., Gerdes, A., Hanchar, J.M., Horstwood, M.S.A., Morris, G.A., Nasdala, L., Norberg, N., Schaltegger, U., Schoene, B. Tubrett, M.N, Whitehouse, M.J., 2008, Plešovice zircon — A new natural reference material for U-Pb and Hf isotopic microanalysis. Chemical Geology, 249: 1-35.

Sorbadere, F., Médard, E., Laporte, D., & Schiano, P. (2013). Experimental melting of hydrous peridotite-pyroxenite mixed sources: Constraints on the genesis of silica-undersaturated magmas beneath volcanic arcs. Earth and Planetary Science Letters, 384, 42-56. https://doi.org/10.1016/j.epsl.2013.09.026

Stern, C. R. (2020). The role of subduction erosion in the generation of Andean and other convergent plate boundary arc magmas, the continental crust and mantle. Gondwana Research. 88, 220-249. https://doi.org/10.1016/j.gr.2020.08.006

Stern, T., Houseman, G., Salmon, M., & Evans, L. (2013). Instability of a lithospheric step beneath western North Island, New Zealand. Geology, 41(4), 423-426. https://doi.org/10.1130/g34028.1

Sundell, K. E., George, S. W. M., Carrapa, B., Gehrels, G. E., Ducea, M. N., Saylor, J. E., & Pepper, M. (2022). Crustal thickening of the northern central Andean plateau inferred from trace elements in zircon. Geophysical Research Letters, 49(3). https://doi.org/10.1029/2021gl096443

Sundell, K., Laskowski, A., Kapp, P., Ducea, M., & Chapman, J. (2021). Jurassic to Neogene quantitative crustal thickness estimates in southern Tibet. GSA today, 31(6), 4-10. https://doi.org/10.1130/gsatg461a.1

Sundell, K., Laskowski, A., Kapp, P., Ducea, M., & Chapman, J. (2021). Jurassic to Neogene quantitative crustal thickness estimates in southern Tibet. GSA today: a publication of the Geological Society of America, 31(6), 4-10. https://doi.org/10.1130/gsatg461a.1

Syracuse, E. M., & Abers, G. A. (2006). Global compilation of variations in slab depth beneath arc volcanoes and implications. Geochemistry, Geophysics, Geosystems: G(3), 7(5). https://doi.org/10.1029/2005GC001045

Syracuse, E. M., Maceira, M., Prieto, G. A., Zhang, H., & Ammon, C. J. (2016). Multiple plates subducting beneath Colombia, as illuminated by seismicity and velocity from the joint inversion of seismic and gravity data. Earth and Planetary Science Letters, 444, 139-149. https://doi.org/10.1016/j.epsl.2016.03.050

Syracuse, E. M., van Keken, P. E., & Abers, G. A. (2010). The global range of subduction zone thermal models. Physics of the Earth and Planetary Interiors, 183(1–2), 73–90. https://doi.org/10.1016/j.pepi.2010.02.004

Tang, M., Erdman, M., Eldridge, G., & Lee, C.-T.A. (2018). The redox “filter” beneath magmatic orogens and the formation of continental crust: Science Advances, 4(5), eaar4444, https://doi .org/10.1126/sciadv.aar4444.

Tang, M., Ji, W. Q., Chu, X., Wu, A., & Chen, C. (2021). Reconstructing crustal thickness evolution from europium anomalies in detrital zircons. Geology, 49(1), 76-80. https://doi.org/10.1130/G47745.1

Tang, M., Lee, C.-T. A., Chen, K., Erdman, M., Costin, G., & Jiang, H. (2019b). Nb/Ta systematics in arc magma differentiation and the role of arclogites in continent formation. Nature Communications, 10(1), 235. https://doi.org/10.1038/s41467-018-08198-3

Tang, M., Lee, C.-T.A., Costin, G., & Höfer, H.E. (2019a). Recycling reduced iron at the base of magmatic orogens: Earth and Planetary Science Letters, 528, 115827. https://doi.org/10.1016/ j.epsl.2019.115827

Thorkelson, D. J., Madsen, J. K., & Sluggett, C. L. (2011). Mantle flow through the Northern Cordilleran slab window revealed by volcanic geochemistry. Geology, 39(3), 267-270. https://doi.org/10.1130/g31522.1

Torres-Hernández, M. P. (2010). Petrografía, geocronología y geoquímica de las ignimbritas de la Formación Popayán, en el contexto del vulcanismo del Suroccidente de Colombia. MsC. Thesis. Universidad EAFIT. 1-132p.

Van Avendonk, H. J. A., Kuo-Chen, H., McIntosh, K. D., Lavier, L. L., Okaya, D. A., Wu, F. T., Wang, C. Y., Lee, C. S., & Liu, C. S. (2014). Deep crustal structure of an arc-continent collision: Constraints from seismic traveltimes in central Taiwan and the Philippine Sea: Central Taiwan crustal structure. Journal of Geophysical Research. Solid Earth, 119(11), 8397-8416. https://doi.org/10.1002/2014jb011327

van der Wiel, A.M. (1991). Uplift and Volcanism of the SE Colombian Andes in relation to Neogene sedimentation in the Upper Magdalena Valley. PhD. Thesis. University of Wageningen, 1-208 p.

Vermeesch, P. (2018). IsoplotR: A free and open toolbox for geochronology. Geoscience Frontiers, 9(5), 1479-1493. https://doi.org/10.1016/j.gsf.2018.04.001

Vermeesch, P. (2021). Maximum depositional age estimation revisited. Geoscience Frontiers, 12(2), 843-850. https://doi.org/10.1016/j.gsf.2020.08.008

Vervoort, J. D., & Blichert-Toft, J. (1999). Evolution of the depleted mantle: Hf isotope evidence from juvenile rocks through time. Geochimica et Cosmochimica Acta, 63(3-4), 533-556. doi.org/10.1016/S0016-7037(98)00274-9.

Vervoort, J. D., Patehett, P. J., Söderlund, U., & Baker, M. (2004). Isotopie composition of Yb and the determination of Lu concentrations and Lu/Hf ratios by isotope dilution using MC-ICPMS. Geochemistry, Geophysics, Geosystems: G(3), 5(11). https://doi.org/10.1029/2004GC000721

Vervoort, J. D., & Patchett, P. J., (1996). Behavior of hafnium and neodymium isotopes in the crust: Constraints from Precambrian crustally derived granites. Geochimica et Cosmochimica Acta 60, 3717-3733. https://doi.org/10.1016/0016-7037(96)00201-3

Villagómez, D., & Spikings, R. (2013). Thermochronology and tectonics of the Central and Western Cordilleras of Colombia: Early Cretaceous-Tertiary evolution of the Northern Andes. Lithos, 160-161, 228-249. https://doi.org/10.1016/j.lithos.2012.12.008

Villagómez, D., Spikings, R., Magna, T., Kammer, A., Winkler, W., & Beltrán, A. (2011). Geochronology, geochemistry and tectonic evolution of the Western and Central cordilleras of Colombia. Lithos, 125(3-4), 875-896. https://doi.org/10.1016/j.lithos.2011.05.003

Vinasco, C. J., Cordani, U. G., González, H., Weber, M., & Pelaez, C. (2006). Geochronological, isotopic, and geochemical data from Permo-Triassic granitic gneisses and granitoids of the Colombian Central Andes. Journal of South American Earth Sciences, 21(4), 355-371. https://doi.org/10.1016/j.jsames.2006.07.007

Wagner, L. S., Jaramillo, J. S., Ramírez-Hoyos, L. F., Monsalve, G., Cardona, A., & Becker, T. W. (2017). Transient slab flattening beneath Colombia. Geophysical Research Letters, 44(13), 6616-6623. https://doi.org/10.1002/2017gl073981

Waldbaum, D. R. (1971). Temperature changes associated with adiabatic decompression in geological processes. Nature, 232(5312), 545-547. https://doi.org/10.1038/232545a0

Wang, X., Griffin, W. L., & Chen, J. (2010). Hf contents and Zr/Hf ratios in granitic zircons. Geochemical Journal, 44(1), 65-72. https://doi.org/10.2343/geochemj.1.0043

Weber, M. B. I., 1998. The Mercaderes-Rio Mayo xenoliths, Colombia: their bearing on mantle and crustal processes in the Northern Andes. PhD. Thesis. University of Leicester (United Kingdom), 1-295 p.

Weber, M. B. I., Tarney, J., Kempton, P. D., & Kent, R. W. (2002). Crustal make-up of the northern Andes: evidence based on deep crustal xenolith suites, Mercaderes, SW Colombia. Tectonophysics, 345(1-4), 49-82. https://doi.org/10.1016/s0040-1951(01)00206-2

Weber, M., Cardona, A., Valencia, V., García-Casco, A., Tobón, M., & Zapata, S. (2010). U/Pb detrital zircon provenance from late cretaceous metamorphic units of the Guajira Peninsula, Colombia: Tectonic implications on the collision between the Caribbean arc and the South American margin. Journal of South American Earth Sciences, 29(4), 805-816. https://doi.org/10.1016/j.jsames.2009.10.004

White, W. M., Albarède, F., & Télouk, P. (2000). High-precision analysis of Pb isotope ratios by multi-collector ICP-MS. Chemical Geology, 167(3-4), 257-270. https://doi.org/10.1016/s0009-2541(99)00182-5

Wiedenbeck, M., Allé, P., Corfu, F., Griffin, W. L., Meier, M., Oberli, F., Quadt, A. V. O. N., Roddick, J. C., & Spiegel, W. (1995). Three natural zircon standards for u-Th-Pb, Lu-Hf, trace element and Ree analyses. Geostandards Newsletter, 19(1), 1-23. https://doi.org/10.1111/j.1751-908x.1995.tb00147.x

Williams, I.S. (1998). U-Th-Pb geochronology by ion microprobe: M.A. McKibben, W.C. Shanks III, W.I. Ridley (Eds.), Applications of Microanalytical Techniques to Understanding Mineralizing Processes: Reviews in Economic Geology, 7, 1-35. https://doi.org/10.5382/Rev.07.01

Woodhead, J. D., & Hergt, J. M. (2005). A preliminary appraisal of seven natural zircon reference materials for in situ Hf isotope determination. Geostandards and Geoanalytical Research, 29(2), 183-195. https://doi.org/10.1111/j.1751-908x.2005.tb00891.x

Yang, J., Cawood, P. A., Du, Y., Huang, H., Huang, H., & Tao, P. (2012). Large Igneous Province and magmatic arc sourced Permian-Triassic volcanogenic sediments in China. Sedimentary Geology, 261-262, 120-131. https://doi.org/10.1016/j.sedgeo.2012.03.018

Zapata, S., Calderon-Diaz, L., Jaramillo, C., Oboh-Ikuenobe, F., Piedrahita, J. C., Rodríguez-Cuevas, M., Cardona, A., Sobel, E. R., Parra, M., Valencia, V., Patiño, A., Jaramillo-Rios, J. S., Flores, M., & Glodny, J. (2023a). Drainage and sedimentary response of the Northern Andes and the Pebas system to Miocene strike-slip tectonics: A source to sink study of the Magdalena Basin. Basin Research, 35(5), 1674-1717. https://doi.org/10.1111/bre.12769

Zapata, S., Cardona, A., Jaramillo, J. S., Patiño, A., Valencia, V., León, S., Mejía, D., Pardo-Trujillo, A., & Castañeda, J. P. (2019). Cretaceous extensional and compressional tectonics in the Northwestern Andes, prior to the collision with the Caribbean oceanic plateau. Gondwana Research: International Geoscience Journal, 66, 207-226. https://doi.org/10.1016/j.gr.2018.10.008

Zapata, S., Jaramillo-Ríos, J. S., Botello, G.E., Siachoque, A., Calderon-Día, L. C., Cardona, A., Till, C., & Valencia, V. (2023b). Miocene Paleogeography of NW Colombia: A review of the sedimentary and magmatic evolution of the Amagá Basin a century after Grosse's

work. Revista de la Academia Colombiana de Ciencias Exactas, Fisicas y Naturales. https://doi.org/10.18257/raccefyn.1871

Zapata, S., Zapata-Henao, M., Cardona, A., Jaramillo, C., Silvestro, D., & Oboh-Ikuenobe, F. (2021). Long-term topographic growth and decay constrained by 3D thermo-kinematic modeling: Tectonic evolution of the Antioquia Altiplano, Northern Andes. Global and Planetary Change, 203. https://doi.org/10.1016/j.gloplacha.2021.103553

Zapata-García, G. & Rodríguez-García, G. (2020). New contributions to the knowledge about the Chocó-Panamá Arc in Colombia, including a new segment south of Colombia. In: Gómez, J. & Mateus-Zabala, D. (editors), The Geology of Colombia, Volume 3 Paleogene - Neogene. Servicio Geológico Colombiano, Publicaciones Geológicas Especiales 37, 417-450. Bogotá. https://doi.org/10.32685/pub.esp.37.2019.14

Zapata-Villada, J. P., Cardona, A., Serna, S., & Rodríguez, G. (2021). Late Cretaceous to Paleocene magmatic record of the transition between collision and subduction in the Western and Central Cordillera of northern Colombia. Journal of South American Earth Sciences, 112, 103557. https://doi.org/10.1016/j.jsames.2021.103557

Zhao, L., Guo, F., Fan, W., & Huang, M. (2019). Roles of Subducted Pelagic and Terrigenous Sediments in Early Jurassic Mafic Magmatism in NE China: Constraints on the Architecture of Paleo-Pacific Subduction Zone. Journal of Geophysical Research: Solid Earth 124, 2525-2550. https://doi.org/10.1029/2018JB016487

Zieman, L., Ibañez-Mejia, M., Rooney, A. D., Bloch, E., Pardo, N., Schoene, B., & Szymanowski, D. (2023). To sink, or not to sink: The thermal and density structure of the modern northern Andean arc constrained by xenolith petrology. Geology, 51(6), 586-590. https://doi.org/10.1130/g50973.1

Zimmerer, M. J., & McIntosh, W. C. (2012). The geochronology of volcanic and plutonic rocks at the Questa caldera: Constraints on the origin of caldera-related silicic magmas. Bulletin of the Geological Society of America, 124(7-8), 1394-1408. https://doi.org/10.1130/B30544.1.